The Astrophysical Journal Supplement Series, 257:66 (35pp), 2021 December https://doi.org/10.3847/1538-4365/ac2828

Point-spread Function Deconvolution of the IFU Data and Restoration of Galaxy Stellar Kinematics

Haeun Chung[1,2,3], Changbom Park[3], and Yong-Sun Park[2]
[1] University of Arizona, Steward Observatory, 933 N. Cherry Ave., Tucson, AZ 85721, USA
[2] Astronomy Program, Department of Physics and Astronomy, Seoul National University, 1 Gwanak-ro, Gwanak-gu, Seoul 08826, Republic of Korea
[3] School of Physics, Korea Institute for Advanced Study, 85 Hoegiro, Dongdaemun-gu, Seoul 02455, Republic of Korea; cbp@kias.re.kr
Received 2020 August 10; revised 2021 September 4; accepted 2021 September 17; published 2021 December 10

Abstract

We present a performance test of the point-spread function (PSF) deconvolution algorithm applied to astronomical integral field unit (IFU) spectroscopy data for restoration of galaxy kinematics. We deconvolve the IFU data by applying the Lucy–Richardson algorithm to the 2D image slice at each wavelength. We demonstrate that the algorithm can effectively recover the true stellar kinematics of the galaxy, by using mock IFU data with a diverse combination of surface brightness profile, signal-to-noise ratio, line-of-sight geometry, and line-of-sight velocity distribution (LOSVD). In addition, we show that the proxy of the spin parameter λ_{R_e} can be accurately measured from the deconvolved IFU data. We apply the deconvolution algorithm to the actual SDSS-IV MaNGA IFU survey data. The 2D LOSVD, geometry, and λ_{R_e} measured from the deconvolved MaNGA IFU data exhibit noticeable differences compared to the ones measured from the original IFU data. The method can be applied to any other regular-grid IFU data to extract the PSF-deconvolved spatial information.

Unified Astronomy Thesaurus concepts: Galaxy kinematics (602); Galaxy rotation (618); Deconvolution (1910); Astronomy data analysis (1858); Spectroscopy (1558)

1. Introduction

Integral field spectroscopy (IFS), or 3D spectroscopy, is an observational technique used to collect the 2D spatial information on the spectral properties of the target object. IFS observation can be performed by using a single or multiple integral field unit(s) (IFU(s)), a module that captures one contiguous region on the sky. Starting from SAURON IFU (Bacon et al. 2001), many IFS instruments (GMOS, Allington-Smith et al. 2002; VIMOS, Le Fèvre et al. 2005; IMACS, Dressler et al. 2011; PMAS/PPAK, Kelz et al. 2006; KMOS, Sharples et al. 2013; MUSE, Bacon et al. 2010) have been developed in the optical and near-infrared. Nowadays there are thousands of publicly available IFU data from a number of IFU surveys such as ATLAS^{3D} (Emsellem et al. 2011), DiskMass (Bershady et al. 2010), CALIFA (Sánchez et al. 2016), SAMI (Scott et al. 2018), and MaNGA (Bundy et al. 2015). However, all of the IFU data from the aforementioned ground-based surveys have a common limitation (unless corrected by adaptive optics): spatial information degradation corresponding to the point-spread function (PSF). The PSF is a combination of the atmospheric seeing, the aberration from the telescope and instrument optics, and the sampling size/scheme. Notably, the effect becomes more severe for the data obtained by a bare fiber-based IFU, because of the physical gap between sampling elements, which enlarges effective PSF size. Due to the effects of PSF, all derived, measured, or fitted quantities from the IFU data are smoothed and become spatially correlated. To extract the spatially resolved information as much as possible from the IFU data, one must minimize the effects of the PSF. A way to correct the PSF effects is forward modeling, such as a flux-weighted PSF convolution to the 2D model quantities (Cappellari 2008; Bouché et al. 2015). However, this is only an approximation that does not fully reflect the PSF effects.

Historically, there were numerous attempts that tried to mitigate the effects of the PSF on 2D images in the field of signal/image processing in particular (see the summaries by Bongard et al. 2011; Villeneuve & Carfantan 2014, and references therein). However, those techniques are not directly applicable to the astronomical data since they are optimized to three-channel color images or images with different characteristics compared to astronomical images. There were studies in the field of astronomy that adopted deconvolution, such as optimal spectrum extraction from the CCD image (Courbin et al. 2000; Lucy & Walsh 2003), or reduction of the Spitzer slit spectroscopy data (Rodet et al. 2008). More recently, several techniques (Bourguignon et al. 2011; Bongard et al. 2011; Soulez et al. 2011; Villeneuve & Carfantan 2014) were proposed to restore the 3D correlated IFU data in both spatial and spectral direction in the context of MUSE (Henault et al. 2003). Bongard et al. (2011) utilized prior knowledge on the correlation between spatial and spectral direction to deconvolve the IFU data by using a regularized χ^2 method. This technique requires two hyperparameters for the deconvolution; however, the parameters are determined not by quantitative criteria but by visual inspection of the results from various sets of parameters through trial and error. Villeneuve & Carfantan (2014) proposed to use the nonlinear deconvolution technique on the IFU data with Markov Chain Monte Carlo in a Bayesian framework, to recover the flux, the relative velocity, and the velocity dispersion distribution of the target. The technique was demonstrated on simulated IFU data from mock observation of objects with two separated emission lines.

In this work, we explore a general method to mitigate the effects of the PSF that can be applied to any kind of IFU data. In particular, we study the performance of the PSF deconvolution method applied to extended sources (galaxies) to restore their true kinematics. This work was motivated by the study of stellar kinematics of SDSS-IV MaNGA survey galaxies. We use the Lucy–Richardson (LR) algorithm (Richardson 1972; Lucy 1974), which is one of the simplest deconvolution techniques and requires a minimum number of parameters. We

validate the algorithm using mock IFU data and show that the kinematics of galaxies can be well restored through our deconvolution procedure. In addition, we apply the deconvolution method to measure the spin parameter λ_{R_e} (Emsellem et al. 2007), which is a widely used proxy of the galaxy angular momentum.

The structure of this paper is as follows. In Section 2, we introduce the LR deconvolution algorithm and its implementation to the IFU data. We demonstrate the validity of the deconvolution technique using the mock IFU data in Section 3. In Section 4 we illustrate the example of deconvolution to the MaNGA IFU data. Finally, we show how the deconvolution can be used to improve the measurement of spin parameter λ_{R_e} in Section 5, and we present a summary in Section 6.

2. PSF Deconvolution of IFS Data

2.1. Lucy–Richardson Deconvolution Algorithm

The LR deconvolution algorithm is an iterative procedure to recover an image that is blurred (convolved) by a PSF. The algorithm is introduced here in a simple form,

$$u^{n+1} = u^n \cdot \left(\frac{d}{u^n \otimes p} \otimes p \right), \quad (1)$$

where u^n is the nth estimate of the 2D maximum likelihood solution ($u^0 = d$), d is the original PSF-convolved image, p is the 2D PSF, and $\otimes$ denotes 2D convolution. If d follows the Poisson statistics and u^n converges as iteration proceeds, u^n becomes the maximum likelihood solution (Shepp & Vardi 1982). The LR deconvolution method has several advantages: (1) it is straightforward to implement, (2) it requires only a few parameters to perform, and (3) it can perform fast on an average computing machine (takes less than 4 minutes on a 2.67 GHz single-core CPU when applied to a $72 \times 72 \times 4563$ cube ($x \times y \times$ wavelength)). If the shape of the PSF is known as Gaussian, then only two parameters are required for the procedure: (1) FWHM of Gaussian and (2) a number of iterations. The algorithm produces a nonnegative solution since it assumes Poisson statistics. However, there are well-known drawbacks of the algorithm, which are (1) the noise amplification and (2) the ringing artifact structure around the sharp feature, which both happen as the number of iteration ($N_{\rm iter}$) increases (Magain et al. 1998). Therefore, the relation between the number of iteration and the quality of the deconvolved data should be investigated before using the deconvolved data for further scientific analysis.

2.2. Implementation to the IFU Data

We develop a `Python3` code to apply the LR deconvolution algorithm to optical IFU data. We consider IFU data as a combination of 2D images at multiple wavelength bins, and we perform the deconvolution method on the 2D image slice at each wavelength bin independently. In other words, we apply the deconvolution method only in the spatial directions, not in the spectral direction. The core part of the procedure is written to follow Equation (1). We implement fast Fourier transform (FFT; Cooley & Tukey 1965; Press et al. 2007) to increase the speed of the procedure. The algorithm requires a 2D image of the PSF that has identical size to the input 2D image slice. Here we use a 2D Gaussian function image as a PSF, but it can be any other shape in practice.

To cope with the wavelength dependency of the $\mathrm{FWHM_{PSF}}$ size, we assume the size of $\mathrm{FWHM_{PSF}}$ as a linear function of wavelength and deconvolve a 2D image slice at each wavelength bin with corresponding $\mathrm{FWHM_{PSF}}$ size. We apply a zero padding on the 2D slice image to increase its size to $2^N \times 2^N$ before deconvolution to maximize the execution speed of FFT. After the zero padding, the zero-padded pixels, bad pixels, and all nonpositive pixels are marked. The marked pixels are replaced by proper nonzero values to avoid having an oscillation feature around the masked pixels or having invalid pixel values after the deconvolution. These marked pixels are substituted by an iterative value-correction process, which alters the marked pixels to the average of the nearest positive pixel values. The value-correction process is applied multiple times until the boundary of the data is extended by three times the $\mathrm{FWHM_{PSF}}$. This process significantly reduces the artificial effect owing to the sharp edge in the result of the deconvolution. Finally, the LR deconvolution algorithm is performed on the value-corrected $2^N \times 2^N$ size image. The values that were replaced by the value-correction process are masked to zero after the deconvolution, and the padded region is cut out. We present the deconvolution code in `Python3` for public use available on `GitHub`[4] under an MIT License, and version 1.0 is archived in Zenodo (Chung 2021).

3. Deconvolution Method Parameter Determination and Performance Test

In this section, we verify the reliability of the deconvolution method and also determine the proper value of the deconvolution parameter, which is the number of iteration. We also check the acceptable range of the other deconvolution parameter, $\mathrm{FWHM_{PSF}}$, when the value is different from the correct $\mathrm{FWHM_{PSF}}$ value that is originally imprinted to the PSF-convolved IFU data. We use three sets of mock IFU data: the first one where no PSF is convolved, the second one where a PSF is convolved to the first one, and the third one where the PSF is deconvolved from the second one by our deconvolution method. The first set of mock IFU data is generated by using a model galaxy with various photometric and kinematic parameters. We use differences between the true galaxy model parameter values and the corresponding parameter values that are extracted from the PSF-deconvolved mock IFU data as metrics of the deconvolution performance. Using those metrics, we quantify the effect of the deconvolution and determine the proper deconvolution procedure parameter values ($N_{\rm iter}$ and $\mathrm{FWHM_{PSF}}$).

3.1. Mock Galaxy Model

We define a mock galaxy model that resembles an actual rotating galaxy. Our mock galaxy is composed of simple photometric and kinematic models, which are flux distribution with the Sérsic profile and kinematic distribution with the thin-disk approximated galaxy rotation curve (RC) function and a simple radial velocity dispersion function.

We use a model of a galaxy with infinitely thin disk shape and ordered rotation. There are several functional forms to

[4] http://github.com/astrohchung/deconv. An example code to deconvolve MaNGA IFU data and compare the 2D kinematics measured from the original and the deconvolved MaNGA data is provided (partially reconstruct Figure 9).

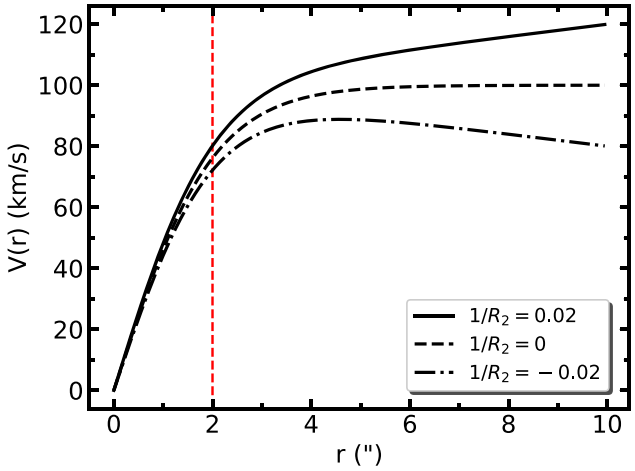

Figure 1. Example of an RC model. Each line shows a different shape at the outskirts described by the $1/R_2$ value (when $V_{\rm ROT} = 100$ km s^{-1} and $R_1 = 2''$). The vertical dotted line indicates R_1.

describe the typical shape of the disk galaxies: an arctangent (Puech et al. 2008), a hyperbolic tangent (Andersen & Bershady 2013), and an inverted exponential (Feng & Gallo 2011). All these models have an RC converging to a constant velocity at their outer radii, namely, the well-known *flat* RC. Although it is nontrivial to describe the complex shape of the real RC in a simple form, we try to improve the current model while maintaining its simple form. We propose the following RC model, which is a combination of the hyperbolic tangent function and a linear term:

$$V(r) = V_{\rm ROT}\left[\tanh\left(\frac{r}{R_1}\right) + \frac{r}{R_2}\right], \quad (2)$$

where $V_{\rm ROT}$ is a maximum circular velocity if $1/R_2 = 0$, R_1 is a characteristic radius where the curve slope changes, and $1/R_2$ is the slope of the curve at its outer radii. Figure 1 shows a few examples of this model with different signs of $1/R_2$. The advantage of this model is that it can describe the inclined/flat RC at the outer radii, as well as the rigid-body rotation motion at near the center of galaxy, which are typically observed in the RC of real galaxies. We would like to point out that there is a degeneracy between R_1 and $1/R_2$ in terms of the shape of the curve. For example, the shape of the RC model with certain $R_1 = a$ and $1/R_2 = b$ is identical to the other RC model with $R_1 = ca$ and $1/R_2 = b/c$. Therefore, to compare the shape of different sets of our RC model parameters, a normalized RC outer radius, R_1/R_2, should be used.

We use a line-of-sight (LOS) velocity dispersion function as follows:

$$\sigma_r = \frac{\sigma_0}{\sigma' r/R_1 + 1}, \quad (3)$$

where σ_0 is a velocity dispersion at the center, r is a circular radial distance from the center of a galaxy, and R_1 is a characteristic scale that is set to be identical to the one in the RC model. The slope of σ_r is mainly described by the R_1, but σ' is introduced to provide an additional freedom to the slope (Section 5.1). The σ_r form is taken from Graham et al. (2018) with slight modification, and it also well describes the actual velocity dispersion distribution of galaxies (see Section 4.3).

Table 1
Mock IFU Data Parameters (Group 1 and 2)

Parameter	Value
IFU FOV (arcsec)	32
IFU radial coverage in R_e	2.5
S/N at 1 R_e	10, 20, 30
Sérsic index	1, 4
Inclination (deg)	40, 55, 70
Position angle (deg)	15
$V_{\rm ROT}$ (km s^{-1})	200
R_1 (arcsec), $1/R_2$ (1/arcsec)	3, −0.05 3, 0.00 3, 0.05 2, 0.05 4, 0.05
σ_0 (km s^{-1})	150
σ'	1
FWHM coefficient c_0 (arcsec)	2.6 (Group 1) 2.3, 2.6, 2.9 (Group 2)
FWHM coefficient c_1 ($\times 10^{-5}$ arcsec Å^{-1})	−1.2
Redshift	0.02

Note. S/N at 1 R_e is defined as the median S/N of a spaxel around 1 R_e per spectral element.

3.2. Mock IFU Data

We generate three *groups* of mock IFS data using the aforementioned photometric and kinematic galaxy model. Each group of mock IFU data is determined by multiple *sets* of model parameters, and each mock IFU datum is generated to follow the 2D velocity, velocity dispersion, and flux distribution determined by a set of model parameters. The details of the mock IFU generation process are described in Appendix A. Here, we only describe the composition of each mock IFU data group.

The purpose of Group 1 is to investigate the performance of the deconvolution with respect to the number of deconvolution iterations. We determine sets of model parameters as in Table 1 to elaborate the diverse properties of galaxies. We use the realistic model parameters that could represent the photometric and kinematic distributions of actual galaxies such as the target galaxies of the SDSS-IV MaNGA IFU survey. The S/N at one half-light radius (1 R_e) is defined similarly to the MaNGA data, where S/N = 14–35 per spatial element per spectral resolution element in r band at 1 R_e (Bundy et al. 2015). We also choose the shape and size of the mock IFU field of view (FOV) to be the same as the MaNGA IFU data, which have a hexagonal shape with the FOV size of 12″ to 32″ in vertex to vertex, with the size of the spatial element as $0\farcs5 \times 0\farcs5$. The combination of each parameter, S/N at 1 R_e, Sérsic index ($n_{\rm Sérsic}$), inclination angle, R_1, and $1/R_2$, yields 90 sets of mock galaxies ($3 \times 2 \times 3 \times 5 = 90$; see Section 3.1 for the definition). For each set of galaxy parameters we construct three types of mock IFU data. Type 1 (Free) are ideal IFU data without any PSF convolution or noise (i.e., free from atmospheric seeing effects and optical aberrations). Type 2 (Conv) are realistic IFU data where Gaussian PSF is convolved and the Gaussian noise is added. Type 3 (Deconv) are PSF-deconvolved IFU data that are obtained by performing the deconvolution method to the Type 2 IFU data. We generate 25 Conv IFU data from each Free mock IFU datum by adding Gaussian random noise with 25 different random seeds. By using the distribution of the

parameters measured from mock IFU data with different random noise, we obtain the statistical distribution of each extracted galaxy model parameter. Also, we assume the wavelength-dependent $\mathrm{FWHM_{PSF}}$, which corresponds to the $\mathrm{FWHM_{PSF,\lambda}} = c_0 + c_1 \times \lambda$, where c_0 and c_1 are as in Table 1. This wavelength-dependent PSF represents the wavelength dependency of the PSF in the real data (Section 4.1). Lastly, 50 Deconv IFU data are produced per each Conv IFU datum with $N_{\mathrm{iter}} = 1$ to 50. In total, 90 Free, 2250 Conv, and 112,500 Deconv mock IFU data are produced as Group 1.

Group 2 is designed to investigate the impact of the two types of $\mathrm{FWHM_{PSF}}$ value on the performance of the deconvolution method: (1) the $\mathrm{FWHM_{Conv}}$ value, which was convolved to the PSF-Free IFU mock data, and (2) the $\mathrm{FWHM_{Deconv}}$ value, which is used for the deconvolution procedure. This is to verify the effect of deconvolution in practical situations where (1) each IFU datum is observed with various atmospheric seeing sizes and (2) the $\mathrm{FWHM_{Deconv}}$ is different from the actual effective $\mathrm{FWHM_{Conv}}$. These effects are identified to ensure that the deconvolution provides more accurate kinematics compared to the one from the nondeconvolved data even with a little inaccurate $\mathrm{FWHM_{Deconv}}$. We again construct three types of mock IFU data using the parameters given in Table 1. Group 2—Type 1 data are identical to the Group 1—Type 1 data. For each of the Group 2—Type 1 Free IFU data, we produce 75 Conv IFU data by using three different c_0 values and the 25 different random noise seeds per each c_0 value. Thirteen Deconv IFU data are produced per each Conv IFU datum with 13 different $\mathrm{FWHM_{Deconv}}$ values, which ranges within $\pm 0\farcs3$ from the c_0 value with a $0\farcs05$ interval. We have chosen the $\pm 0\farcs3$ range considering the $\mathrm{FWHM_{PSF}}$ distribution of actual IFU survey data ($2\farcs2$–$2\farcs7$ in g band; Section 4.1). It is known that such $\mathrm{FWHM_{PSF}}$ could vary up to 10% over the FOV of a single IFU (Law et al. 2016). This means that an average $\mathrm{FWHM_{PSF}}$ difference over a single IFU FOV will be less than $0\farcs3$. Thus, the $\pm 0\farcs3$ range is an extreme case where the entire $\mathrm{FWHM_{PSF}}$ used for the deconvolution is ~10% larger or smaller compared to the actual $\mathrm{FWHM_{PSF}}$. N_{iter} is fixed as 20 times. In total, 90 Free, 6750 Conv, and 87,750 Deconv mock IFU data are produced as Group 2.

Lastly, we produce Group 3 data using a range of mock galaxy model parameters as in Table 2. This is to verify the performance of deconvolution in a more diverse combination of galaxy photometric and kinematic distributions. A total of 40,000 sets of galaxy model parameters are determined randomly in the Monte Carlo way, and 1 Free, 1 Conv, and 1 Deconv mock IFU data are generated for each set. In total, 40,000 Free, 40,000 Conv, and 40,000 Deconv IFU data are produced as Group 3.

Table 2
Mock IFU Data Parameters (Group 3)

Parameter	Value
IFU FOV (arcsec)	12, 17, 22, 27, 32
IFU radial coverage in R_e	1.5, 2.5
S/N at 1 R_e	10–30
Sérsic index	1, 4
Inclination (deg)	10–80
Position angle (deg)	15
V_{ROT} (km s^{-1})	50–300
R_1 (arcsec)	1–4
$1/R_2$ (1/arcsec)	−0.1–0.1
σ_0 (km s^{-1})	50–300
σ'	1
FWHM coefficient c_0 (arcsec)	2.3–2.9
FWHM coefficient c_1 ($\times 10^{-5}$ arcsec Å^{-1})	−3.6–1.2
Redshift	0.02

Note. S/N at 1 R_e is defined as the median S/N of a spaxel around 1 R_e per spectral element. When values of a parameter are listed with commas, one of the values is randomly selected. When values of a parameter are given in a range, the value is selected randomly within the range.

3.3. Kinematics Measurement and Rotation Curve Model Fitting

We measure the LOS kinematics from the mock IFU data produced in Section 3.2 and fit the RC model on the measured 2D kinematic distribution to extract the RC model parameter values. We use an `IDL` version of the penalized-pixel fitting (pPXF; Cappellari & Emsellem 2004; Cappellari 2017) procedure to extract the LOS velocity distribution (LOSVD) from the mock IFU data. To minimize the pPXF computation time, we use model spectral energy distributions (SEDs) identical to the ones that we used for the mock generation (see Appendix A) and fit only the velocity and the velocity dispersion without any additive or multiplicative Legendre polynomials or high-order kinematic moments. Following the recipe from Cappellari (2017), (1) we match the spectral resolution of the model SED to that of the mock IFU data, and (2) we de-redshift the mock IFU spectra to the rest frame before extracting the LOSVD. We also masked the wavelength around the known emission lines, although there is no emission line in the mock IFU spectra. Considering the wavelength coverage of the mock IFU data (3540 to 7410 Å; see Appendix A), we limit the fitting wavelength range as from 3700 to 7400 Å for the LOSVD measurement.

We fit our RC model (Equation (2)) to the extracted 2D velocity map of mock galaxies to quantify the shape of the RC. From the fitting, we obtain the RC model parameters (V_{ROT}, R_1, $1/R_2$) and the kinematic geometrical parameters (center x, center y, position angle, and inclination angle). The fitting procedure uses the minimum χ^2 method that finds a set of parameters that is minimizing the χ^2 between the true 2D velocity map and the measured 2D velocity map. The following equation describes the 2D model velocity map,

$$V_{\mathrm{obs}}(r', \phi') = V_{\mathrm{SYS}} + V(r)\sin i \cos(\phi - \phi_0), \quad (4)$$

where r' is the distance from the kinematic center of the galaxy to each pixel on the sky, r is galaxy-centric radius in the deprojected plane, V_{SYS} is a systematic LOS velocity of the kinematic center, and i and ϕ_0 are kinematic inclination angle and the position angle in the observed (projected) plane, respectively. Including the delta Δx and Δy from the kinematic center position in the observed plane, eight parameters are fitted simultaneously (V_{SYS}, V_{ROT}, R_1, $1/R_2$, i, ϕ_0, Δx_{cent}, and Δy_{cent}).

The minimum χ^2 method is sensitive to the initial values when there are multiple fitting parameters, in particular for the geometrical parameters (i, ϕ_0, Δx_{cent}, and Δy_{cent}). To fit the 2D RC model with suitable initial parameter values, we first fit the 2D Sérsic model to the reconstructed g-band image of the mock IFUs before fitting the RC model. The geometrical parameters

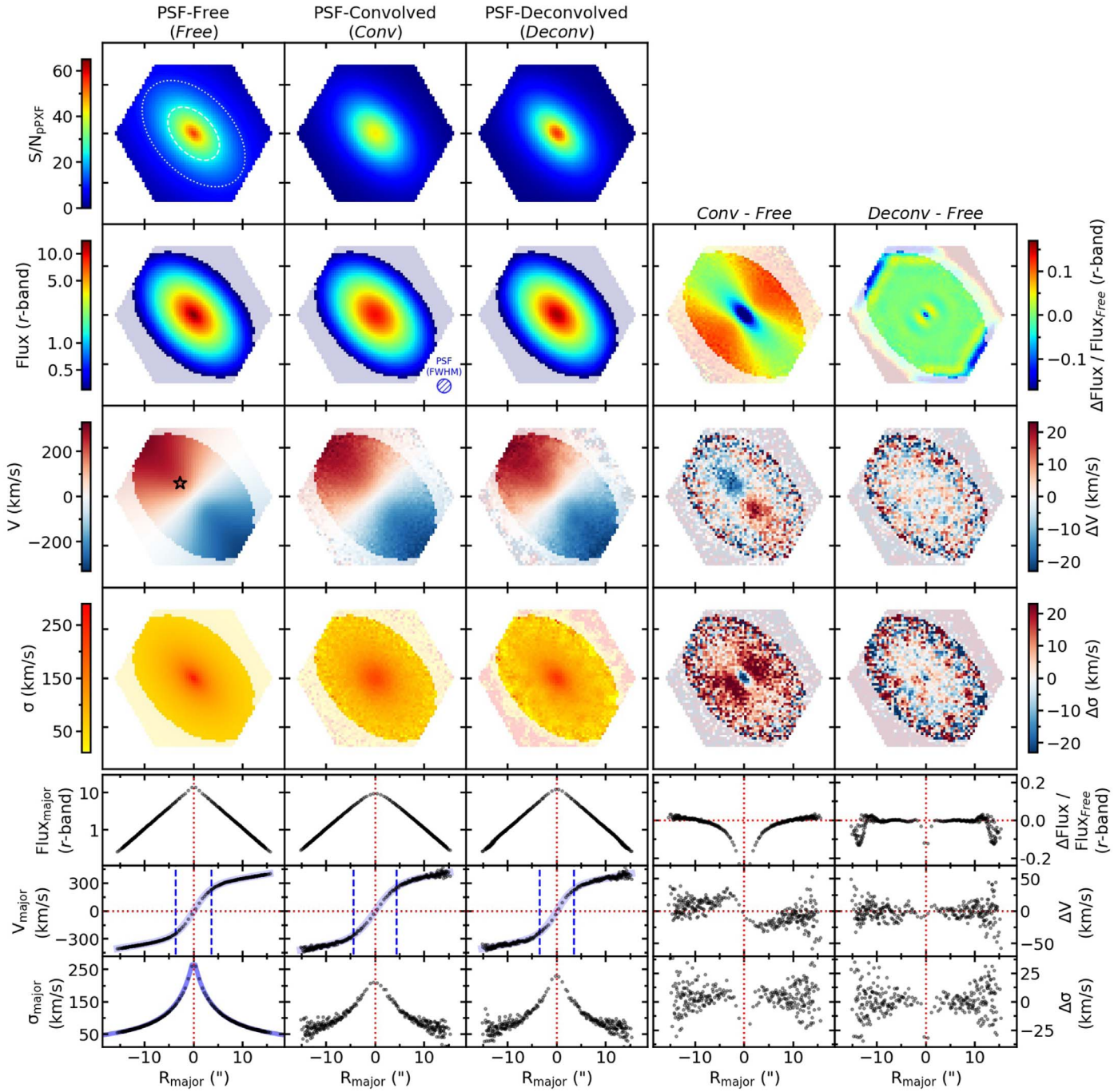

Figure 2. Plots demonstrating the effects of the PSF convolution and deconvolution on the 2D maps of S/N, *r*-band flux, LOS velocity (V), and velocity dispersion (σ). 1D radial profiles of the *r*-band flux, LOS velocity, and velocity dispersion along the major axis are also shown. The first, second, and third columns represent the 2D or 1D distribution of the measured quantities from PSF-Free (Free), PSF-Convolved (Conv), and PSF-Deconvolved (Deconv) mock IFU data, respectively. The mock IFU data are selected from Group 3 Monte Carlo mock IFU samples (see text). The fourth (fifth) column shows the difference between the quantities from the Conv (Deconv) and the Free mock IFU data. The size of the major tick in the 2D maps is $10''$. A dashed (dotted) ellipse is overplotted in the top left panel to represent the size of $1R_e$ ($2R_e$). FWHM of the convolved PSF is shown as a blue hatched circle in the Flux–Conv panel. The black open star on the V–Free panel is the location of the example spectrum in Figure 3. Spaxels with S/N < 3 are paled out in the 2D maps except for the S/N map. Only data points within $\pm 5^\circ$ of major axis are shown in the radial profiles for clarity. Blue paled-out lines are underplotted on the $V_{\rm major}$ profiles (Free, Conv, Deconv) and the $\sigma_{\rm major}$ profile (Free only) to represent the fitted RC (and σ) model functions. Blue vertical dashed lines in the $V_{\rm major}$ profiles denote R_1 of the corresponding fitted RC model function.

obtained from the 2D Sérsic model are used as the initial value of the 2D RC model fitting.

There are two caveats in fitting our RC model:

1. The velocity map should cover sufficiently large radial range along the major axis compared to the R_1; otherwise, the $1/R_2$ parameter cannot be accurately determined. In particular, it is important to have sufficient radial coverage along the major axis. The radial coverage along the minor axis contributes significantly less than the coverage along the major axis to the RC model fitting, because of the $\cos(\phi - \phi_0)$ term in Equation (4).

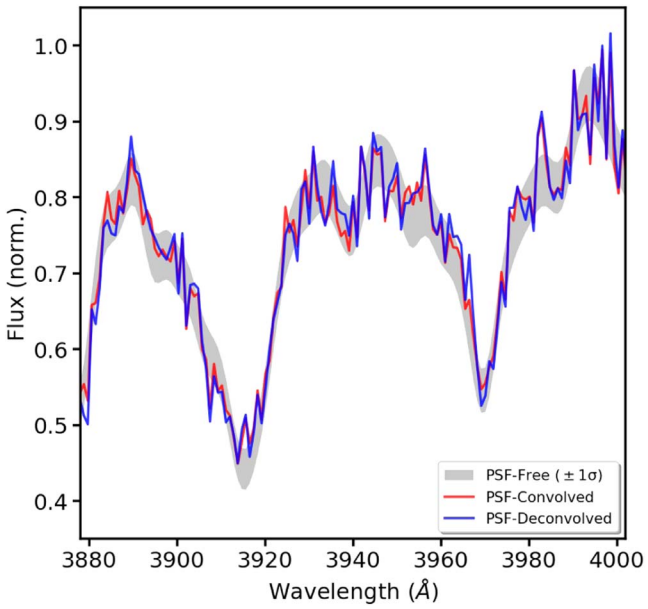

Figure 3. Spectrum of a spaxel whose ΔV between the Conv and the Free is $-20\,\mathrm{km\,s^{-1}}$. Only the spectra around the Ca H and K lines are shown. The location of this spaxel is marked as a black open star in Figure 2. The median S/N of this spaxel is 36. Each spectrum is normalized by the median of each to show only the difference between spectra in their shape. The thickness of the spectrum from Free (gray) represents $\pm 1\sigma$ error at each wavelength bin.

2. The 2D RC model is less sensitive to the galaxies with too low or too high inclination angle. Due to the $\sin i$ term in the Equation (4), the V_{ROT} term is often inaccurately measured at low inclination angle (close to face-on). At high inclination angle, the fitting result is not reliable because of the relatively small number of data points along the major axis and the significant PSF convolution effects that scramble the information between the measured quantities on and out of the major axis, even in the PSF-deconvolved mock IFU data.

In Appendix B, we analyze the RC model fitting result of the Group 3 mock IFU data and derive analytic criteria to ensure the accuracy of the RC model fitting result. We find that when the result satisfies $R_{\mathrm{max,\,S/N>3,major}}/R_{\mathrm{l}} > 2.5$ and the fitted inclination angle falls on $75^\circ > i > 25^\circ$, the fitting results are considered reliable. In addition, we find that the model parameter values measured from the mock IFU data with FOV equal to $12''$ are not well recovered because of an insufficient number of valid data points (S/N > 3) in such a narrow FOV with a given spatial element size ($0\farcs5$ by $0\farcs5$). In further analysis, we only consider the fitting results to be those that are satisfying the above criteria ($R^{\mathrm{major}}_{\mathrm{max,\,S/N>3}}/R_{\mathrm{l}} > 2.5$ and $75^\circ > i > 25^\circ$).

3.4. Results and Discussion

In this subsection, we present the performance of our deconvolution method by using the mock IFU data. We show the relation between the restored kinematics and the deconvolution parameters (N_{iter}, $\mathrm{FWHM_{Deconv}}$) and discuss the adequate choice of the deconvolution parameters. Lastly, we demonstrate the feasibility of applying our deconvolution method to more generalized cases, by showing the test result of the deconvolution method for mock IFU data with various combinations of the galaxy surface brightness distribution, galaxy inner and outer kinematics, its geometry, radial coverage and S/N of data, geometry, and size of the convolved PSF.

3.4.1. Effects of PSF Convolution and Deconvolution

Figure 2 shows the effects of PSF convolution and deconvolution by using test results from one of the Group 3 (Monte Carlo) mock IFU data ($n_{\mathrm{Sérsic}} = 1$, $\mathrm{S/N_{1}}_{R_e} = 25$, $i = 48^\circ$, $V_{\mathrm{ROT}} = 212\,\mathrm{km\,s^{-1}}$, $R_1 = 3\farcs7$, $1/R_2 = 0.02$ (1/arcsec), $\sigma = 74\,\mathrm{km\,s^{-1}}$, $\mathrm{FWHM_{PSF}} = 2\farcs88$, FOV $= 32''$). Panels on the leftmost column show the 2D or 1D quantities measured or extracted from the Free IFU data. The quantities match very well with the model 2D photometric and kinematic distributions that we put in, meaning that the mock IFU data are constructed accurately in accordance with the model parameters. The second-to-left column presents distributions from Conv IFU data, and the second-to-right column displays the difference between the leftmost and the second-to-left column.

As expected, the panels clearly exhibit noticeable changes in all three quantities (flux, velocity, and the velocity dispersion) caused by the PSF convolution. The differences in $\mathrm{Flux_{major}}$ and V_{major} 1D profiles (the second-to-right column) also show evident deviation between the Conv and the Free. In particular, the characteristic radius of the RC (R_1 represents the size of the inner linear part) is increased by the PSF convolution. The overall velocity dispersion around the center is also increased, but at the very center the dispersion is decreased. This is caused by the combination of the PSF convolution effects on the LOS velocity and the velocity dispersion distribution. The convolved PSF *increases* the velocity dispersion, in particular along the minor axis because of the the opposite direction of LOS velocity around the minor axis. On the other hand, the convolved PSF smooths the velocity dispersion distribution so that it *decreases* the velocity dispersion at the center but *increases* the dispersion around the center because the center has both the brightest point and the highest velocity dispersion.

The central column presents the distributions from Deconv IFU data, and the rightmost column shows the difference between the Deconv and the Free. It is clear that the difference between the Deconv and the Free is significantly less than the same between the Conv and the Free. Compared to the Conv column, the apparent b/a ratio is decreased, the flux at the center is increased, and the R_1 of the RC is now much closer to the one from the Free column. The difference in both velocity and velocity dispersion distribution is also much diminished. This result clearly exhibits that the flux, the velocity, and the velocity dispersion distribution from the PSF-deconvolved IFU data are indeed well recovered toward the true distributions. However, the distribution near the edge of the galaxy becomes fuzzier and shows some systematic feature, in particular in the flux distribution. This is partially due to the low S/N near the edge of mock IFU data, and partially due to the edge effect of the deconvolution. We would like to point out that the edge effect in this example is already significantly reduced by the iterative value-correction process (see Section 2.2). Without the iterative value-correction process, the edge effect makes a distinctive artificial hexagonal shape oscillating pattern on the entire image. We put additional examples of Group 1 mock IFU data in Appendix C to show the result with different input distributions. The examples in Appendix C demonstrate that the deconvolution method on IFU data is working effectively

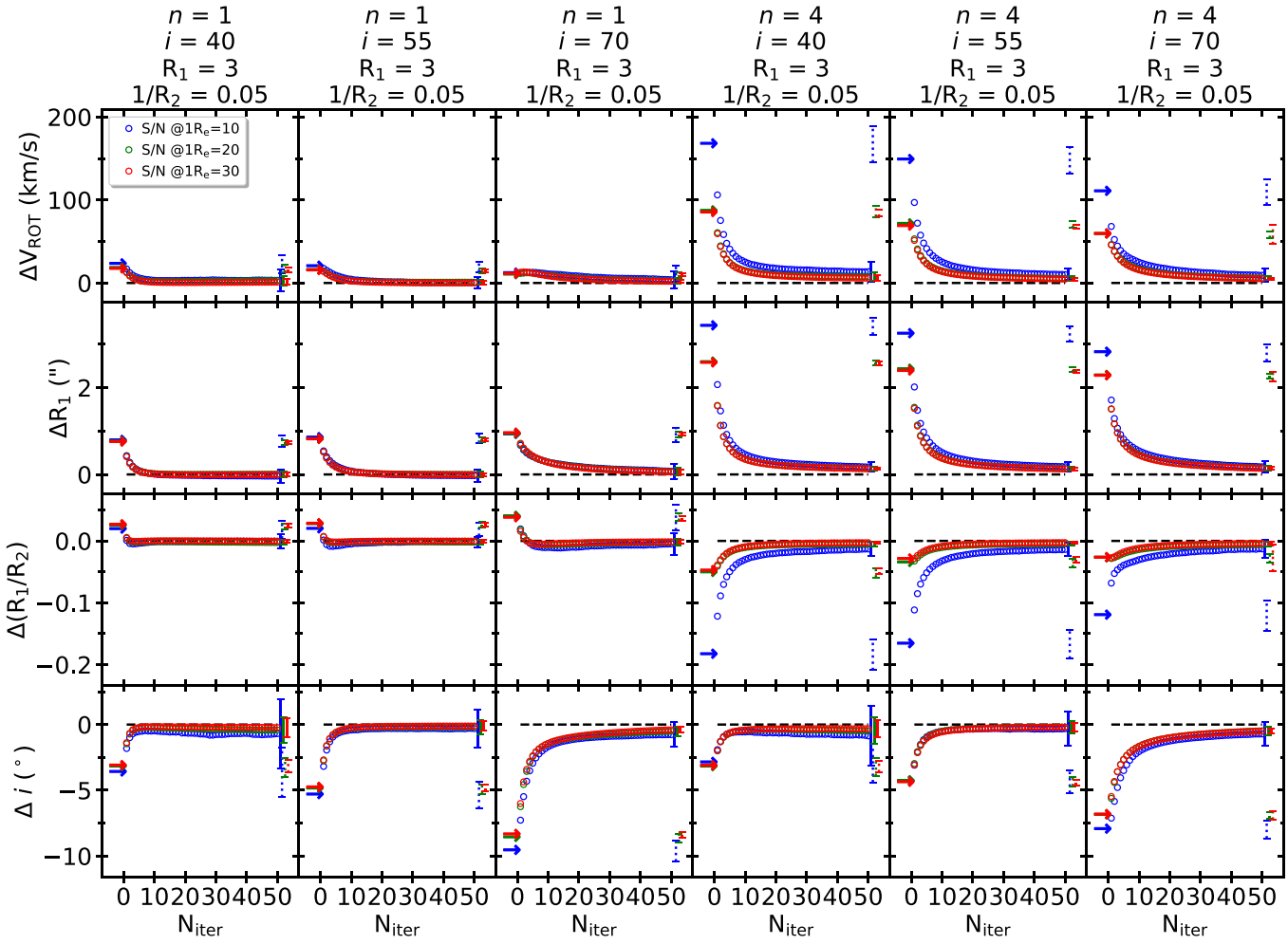

Figure 4. Difference between the true RC model parameters and the fitted model RC parameters from the PSF-deconvolved mock data (Deconv) with respect to the number of LR deconvolution iterations ($N_{\rm iter}$ = 1–50). Each column shows the results from the mock IFU data with different Sérsic index ($n_{\rm Sérsic}$) and kinematic inclination angle (i). In each panel, Δ of one of the four RC model parameters ($\Delta V_{\rm ROT}$, ΔR_1, $\Delta(R_1/R_2)$, and Δi) with a different number of deconvolution iterations ($N_{\rm iter}$) are plotted as open circles. Color represents the S/N at 1 $R_{\rm e}$ value that is used to generate the corresponding PSF-free mock IFU data (Free) of each open circle. Black dashed lines are plotted at the difference of 0 as a guidance. The arrow points out the value of the fitted parameters from the PSF-convolved mock IFU data (Conv). For clarification, we put only one solid error bar per S/N at 1 $R_{\rm e}$ value in each panel instead of putting error bars on every open circle. The error bar represents the standard deviation of each Δ parameter value from 25 different random seeds (there is almost no dependency of the standard deviation of the Δ parameters with respect to $N_{\rm iter}$). The dotted error bar is the corresponding standard deviation from the difference between the true RC model parameter value and the fitted model RC parameter value of the PSF-convolved (Conv) mock IFU data.

well and the method restores the distributions of photometric and kinematic quantities close to the true distributions.

We visualize the effect of the deconvolution method in the wavelength dimension in Figure 3. Figure 3 shows an example of spectra at the spaxel where ΔV between the Conv and the Free is about $-20\,{\rm km\,s^{-1}}$. Because the size of one wavelength bin of the spectrum corresponds to $69\,{\rm km\,s^{-1}}$, ΔV of $-20\,{\rm km\,s^{-1}}$ (∼0.29 pixel) is hardly recognized between the spectra by eyes, even around the strong absorption lines. It is also noticed that the Deconv spectrum is slightly noisier than the Conv spectrum. The mean difference between the Conv and the Free spectrum at this spaxel is 4.0%, but the corresponding difference between the Deconv and the Free spectrum is 4.6%. In fact, the noisier Deconv spectrum is expected by the effect of the LR deconvolution algorithm (noise amplification). Although the Deconv spectrum is noisier than the Conv spectrum, the overall shape of the Conv spectrum has changed and shifted through the deconvolution process, and the LOS velocity and the velocity dispersion of the Deconv spectrum are better recovered to the true value.

3.4.2. Deconvolution Parameters

Figure 4 represents the difference between the fitted and the true RC model parameter value as $N_{\rm iter}$ increases from 1 to 50. The error bar is calculated from the 25 mock IFU data with different random seeds that we implemented for the noise realization. Since the deviation from the true value depends on the galaxy model parameters, we show the result from multiple model galaxies at each column from the Group 1 mock IFU data. The figure shows the case of the mock data with $n_{\rm Sérsic}$ = 1, 4 and $i = 40°$, 55°, 70°. Here we present the difference in R_1/R_2 rather than $1/R_2$, because the R_1/R_2 value better describes the overall shape of the RC without degeneracy (see Section 3.1).

It is evident that the difference between fitted RC model parameter values measured from the Deconv and the true RC

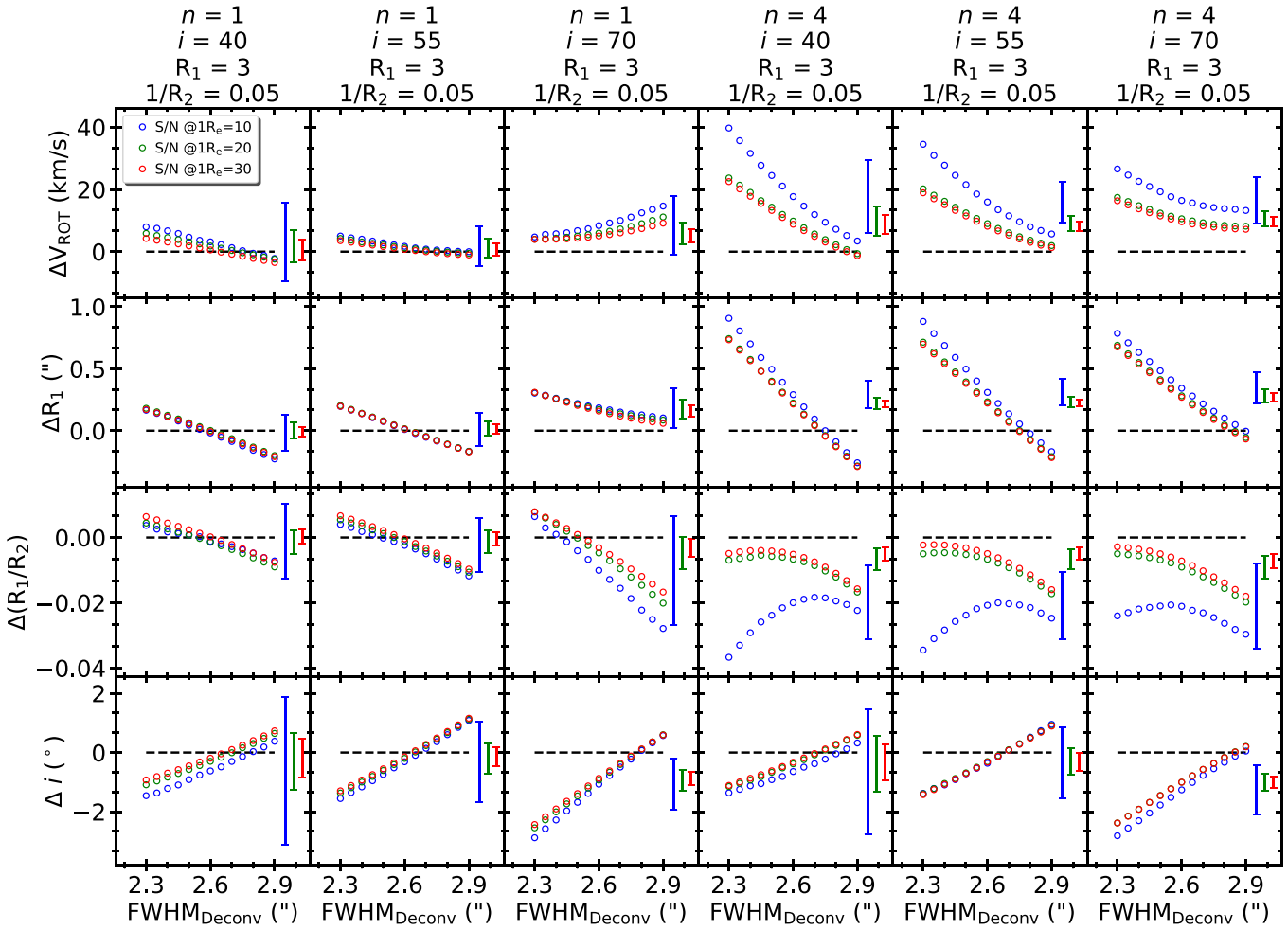

Figure 5. Difference between the true RC model parameters and the fitted model RC parameters from the PSF-deconvolved mock data (Deconv) with respect to the FWHM of the PSF used for the deconvolution (with fixed $N_{\rm iter} = 20$). Each column shows the results from the mock IFU data with different Sérsic index ($n_{\rm Sérsic}$) and kinematic inclination angle (i). In each panel, Δ of one of the four RC model parameters ($\Delta V_{\rm ROT}$, ΔR_1, $\Delta(R_1/R_2)$, and Δi) with different PSF FWHM size used for the deconvolution ($\rm FWHM_{Deconv}$) are plotted as open circles. Color represents the S/N at 1 $R_{\rm e}$ value that is used to generate the corresponding PSF-free mock IFU data (Free) of each open circle. Again, black dashed lines are plotted at the difference of 0 as a guidance. For clarification, we put only one solid error bar per S/N at the 1 $R_{\rm e}$ value in each panel instead of putting error bars on every open circle. The solid error bar represents the standard deviation of each Δ parameter value from 25 different random seeds, as in Figure 4 (there is almost no dependency of the standard deviation of the Δ parameters with respect to $\rm FWHM_{Deconv}$). Note that the y-axis scale of in this figure is smaller than that of Figure 4.

model parameter decreases as $N_{\rm iter}$ increases. Although the difference does not always converge to zero as $N_{\rm iter}$ increases, it is clear that the difference is significantly reduced by the deconvolution method. Note that the size of the 1σ error of the fitted RC model parameter values from Deconv is smaller than the Δ between the parameter values measured from Conv and the true values. This result clearly exhibits that the kinematic parameters are reasonably well restored closely to the true values, even considering the measurement error.

To visualize the effect of $N_{\rm iter}$, we show varying 2D r-band flux, LOS velocity, and velocity dispersion map as $N_{\rm iter}$ changes in Figure D1, using the same mock IFU data as in Figure 2. Note that the variation is shown for selected $N_{\rm iter} = 0$ (Conv; No deconvolution), 1, 2, 3, 10, 20, and 30. Similar to the trend of difference between the true RC model parameters and the fitted model RC parameters to $N_{\rm iter}$ (Figure 4), the amount of difference between 2D maps from true and deconvolved IFU data is larger for the small $N_{\rm iter}$.

Considering the overall trend of the Δ parameter values with respect to $N_{\rm iter}$, it is not obvious to determine the optimal $N_{\rm iter}$ value. Most of the parameters are rapidly converged to the true values during the first $N_{\rm iter} \sim 5$. At $N_{\rm iter} > 5$, the slope of the Δ parameter is reduced, although the slope is generally stiffer when $n_{\rm Sérsic} = 4$ compared to the $n_{\rm Sérsic} = 1$ case. In general, the change of the parameter value depending on $N_{\rm iter}$ is smaller than the error bar when $N_{\rm iter} > 10$ (see also the figures in Appendix D.1). For example, when S/N of data is low (S/N at 1 $R_e \lesssim 10$), in practice, $N_{\rm iter} > 10$ does not improve the Δ parameter for the cases in Figure 4. Moreover, in some cases the Δ parameter is even increased as $N_{\rm iter}$ increases (e.g., the first column of the fourth row and the fourth column of the fourth row in Figure 4 when S/N at 1 $R_e = 10$). This is because the measured parameter values are dominated by the intrinsic error (low S/N) in the data, not by $N_{\rm iter}$. On the other hand, since the error bar is decreasing when the data have high S/N, higher $N_{\rm iter}$ may provide more accurate results if S/N is high. However, as can be seen in Figure 4, the difference between the parameters measured by $N_{\rm iter} = 20$ and $N_{\rm iter} > 20$ is considerably smaller than the difference between the parameters measured by $N_{\rm iter} = 0$ and $N_{\rm iter} = 20$. In addition, the trends of the Δ parameter with medium S/N (S/N at 1 $R_e = 20$) and high S/N (S/N at 1 $R_e = 30$) are nearly overlapped in all $N_{\rm iter}$

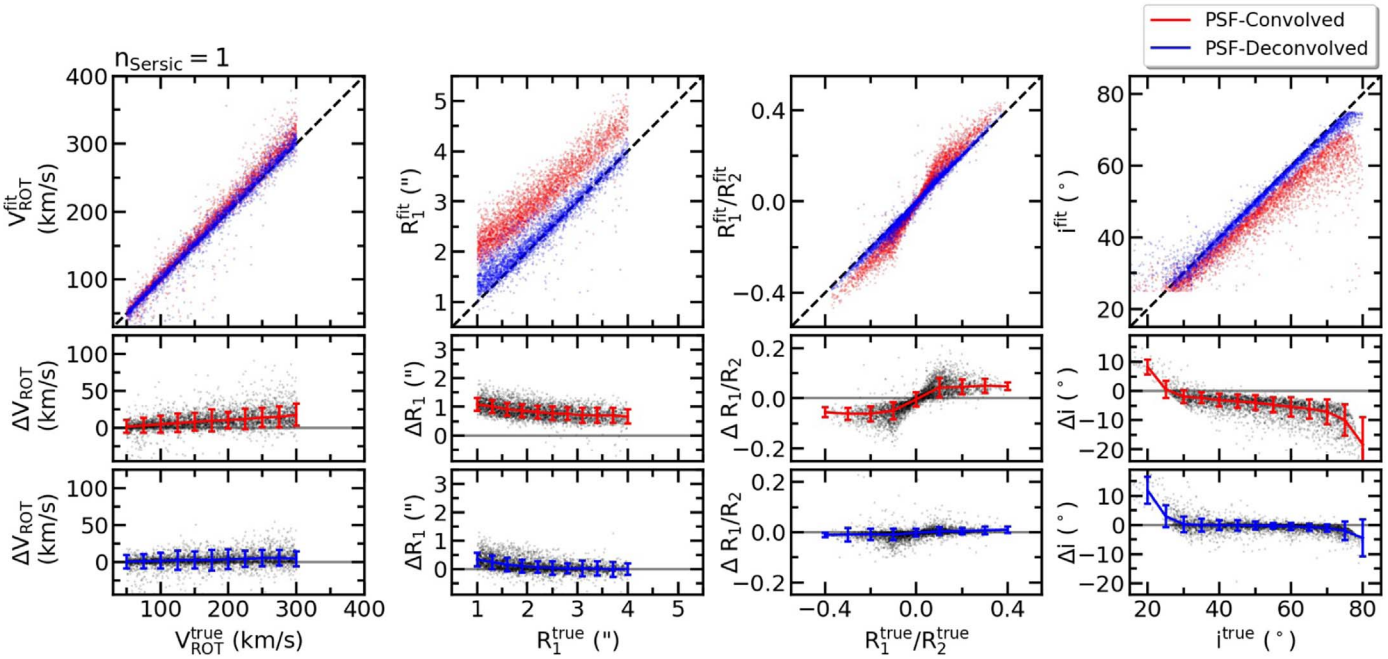

Figure 6. The top panel of each column shows a 1:1 relation between the fitted RC model parameter values from Conv IFU data and the true parameter value (red), and the relation between the fitted RC model parameter values from Deconv IFU data and the true value (blue), when $n_{\rm Sérsic} = 1$. The middle (bottom) panel of each column presents the difference between the fitted RC model parameter values from Conv (Deconv) IFU data and the true value with respect to the true parameter values. The error bar in the middle and the bottom panel shows the 1σ range of the data points within each arbitrary bin size.

versus Δ parameters, compared to the difference between trends of the low-S/N (S/N at 1 $R_e = 10$) and medium-S/N cases (see also Figures D2–D5). This implies that the trend with even higher S/N (S/N at 1 $R_e > 30$) will also follow a similar trend to that for the medium-S/N and high-S/N cases. In this work, considering the S/N at 1 R_e of MaNGA data (14–35; Bundy et al. 2015), we use $N_{\rm iter} = 20$ as the number of deconvolution iterations. In Appendix D.1, we present additional similar figures with various mock galaxy model parameters to support the validity of our deconvolution method.

Figure 5 presents the difference between the fitted RC model parameter and the respective true value as a function of the Gaussian PSF FWHM used for the deconvolution ($\rm FWHM_{Deconv}$). $\rm FWHM_{Deconv}$ is varied from 2.″3 to 2.″9 with 0.″05 increments when the FWHM of the convolved Gaussian PSF ($\rm FWHM_{Conv}$) is 2.″6. $N_{\rm iter}$ is fixed as 20. Again the error is calculated from the result with 25 mock IFU data generated with different random seeds. The figure shows the case of the mock IFU data with the combination of $n_{\rm Sérsic} = 1$, 4 and $i = 40$, 55, 70° with R_1 and $1/R_2$ fixed as 3 and 0.05, respectively. Indeed, there is a dependency of the fitted parameters on the $\rm FWHM_{Deconv}$ value, but variation of the value is not significant when $|\rm FWHM_{Deconv} - FWHM_{Conv}| < 0.''3$, considering the error bar. As the $\rm FWHM_{Deconv}$ is varied, the difference between the parameters from the Deconv (open circles) and the true value changes, but not always linearly. In all cases, the measured parameter values from the deconvolved IFU data are clearly getting closer to the true value, compared to the values without deconvolution (values measured from Conv mock IFU data). Considering all four kinds of fitted parameters, the best result is obtained when $\rm FWHM_{Deconv} = FWHM_{Conv}$, although the difference between the fitted and the true model parameters from the Deconv and the Free are not always minimum at $\rm FWHM_{Deconv} = FWHM_{Conv}$. From this test result, we conclude that in most cases the deconvolved IFU data produce fairly consistent results when $\rm FWHM_{Deconv} - FWHM_{Conv}$ is less than 0.″3 (i.e., when the measurement error of the size of $\rm FWHM_{Conv}$ is less than 0.″3). In Appendix D.2, we present supplementary figures with different $\rm FWHM_{Conv}$ values (2.″3 and 2.″9) and different mock galaxy model parameters.

3.4.3. Results from the Monte Carlo Mock IFU Data

Here we present the result of the deconvolution method performance verification test with Group 3 Monte Carlo mock IFU data. This is to validate that the deconvolution method works well not only with the mock galaxy model with a certain combination of model parameter values but also with a diverse combination of the galaxy model parameters. We divide the results according to $n_{\rm Sérsic}$ value because the results are highly correlated with $n_{\rm Sérsic}$. Figures 6 and 7 show the results with $n_{\rm Sérsic} = 1$ and $n_{\rm Sérsic} = 4$, respectively. Note that we only include the results when the Deconv mock IFU data satisfy the fitting qualification criteria, which are IFU FOV equal to or wider than 17″, $R_{\rm major,\ S/N>3}/R_1 > 2.5$, and $75° > i > 25°$. The number of mock IFU data used for Figure 6 is 2354, and for Figure 7 it is 3820. In Figure 6, all $V_{\rm ROT}$, R_1, R_1/R_2, and i model parameters measured from the Deconv mock IFU data show good agreement with the true value. On the contrary, the model parameter values measured from Conv mock IFU data show considerable deviations from the true value. In Figure 7, again all parameters measured from the Deconv mock IFU data show good agreement with the true value. The model parameter values measured from Conv mock IFU data show larger discrepancy in the case of $n_{\rm Sérsic} = 4$.

Results from the figures show that our deconvolution method successfully restores the kinematic properties of galaxies. It also shows that the measured parameter values from the Conv mock IFU data have a noticeable deviation from the true value,

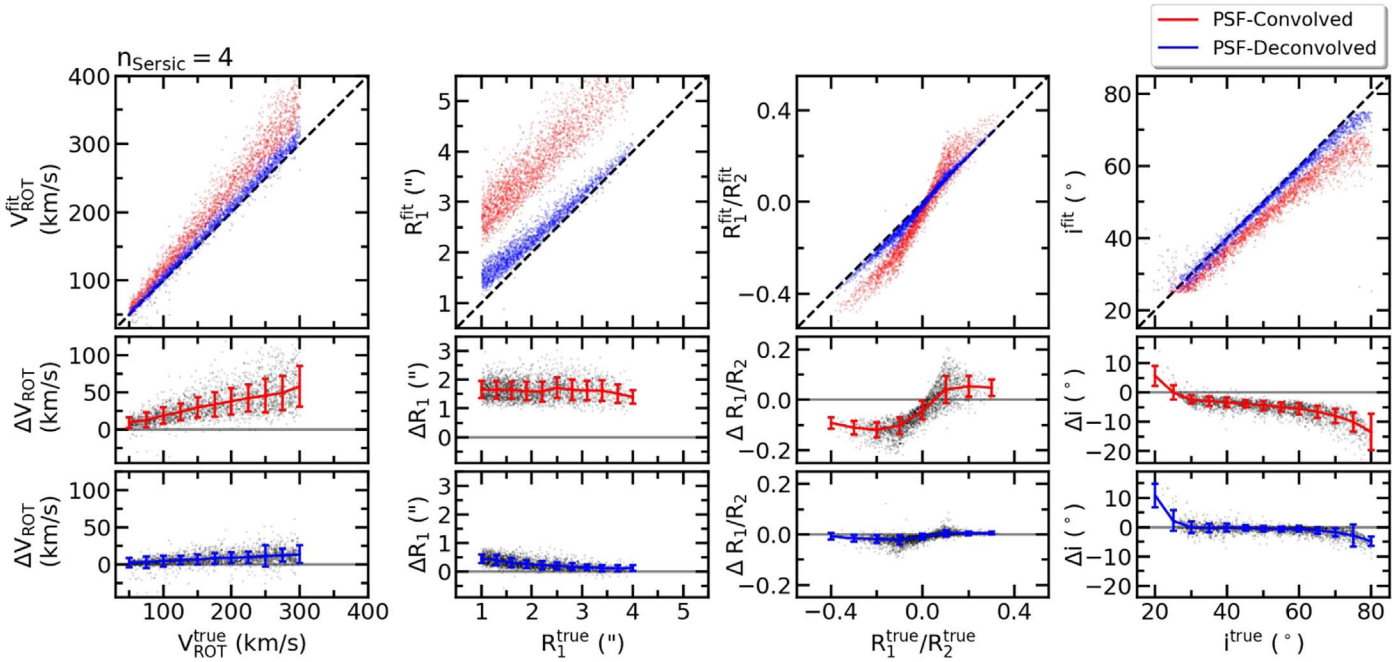

Figure 7. Same as Figure 6, but with mock IFU data of $n_{\text{Sérsic}} = 4$.

especially when $n_{\text{Sérsic}} = 4$. It can be interpreted as the PSF convolution effect becoming more significant when there is a steeper relative flux slope between the adjacent spaxels. This effect is most evident for the R_1 parameter. $R_1^{\text{fit}} - R_1^{\text{true}}$ of the Conv mock IFU data show a median offset of 1.″8 in Figure 7. This large offset also affects $1/R_2$, where many $1/R_2$ values from Conv are measured in the condition where they did not meet the fitting qualification criteria.

4. Application to SDSS-IV MaNGA IFU Data

4.1. MaNGA Point-spread Function

We use IFU data from the third public release of MaNGA (Bundy et al. 2015), which is a part of Sloan Digital Sky Survey (SDSS) Data Release (DR) 15 (Aguado et al. 2019). Among the 4824 DR15 MaNGA cube data, we select 4,426 unique galaxies from the MaNGA main galaxy sample (primary, color-enhanced primary, and secondary; Wake et al. 2017) by removing repeated observations, duplicated galaxies with different MaNGA-ID,[5] and special targets (IC 342, Coma, and M31). For the repeated observations and duplicated galaxies, we choose data observed by a bigger IFU. If both are observed by IFU with the same size, then we use the data with higher blue channel S/N as recorded in the FITS header of the data. In the context of deconvolution, it is important to know the accurate information about the shape and size of PSF that is convolved to each MaNGA IFU datum. According to Law et al. (2015, 2016) and Yan et al. (2016), it is known that (1) the size of the PSF FWHM ranges between 2.″2 and 2.″7 in g band, (2) the shape of the PSF is well described by a single 2D circular Gaussian function, (3) the FWHM of the fitted model Gaussian function agrees with the measured FWHM within 1%–2%, and (4) the PSF FWHM varies less than 10% across the FOV within a single MaNGA IFU. MaNGA IFU data provide the reconstructed MaNGA PSF image in *griz* band, as well as *griz* PSF FWHM values in its header. The g-band PSF FWHM distribution of all the SDSS DR15 MaNGA data is shown in the left panel of Figure 8. To account for the wavelength dependency of the MaNGA PSF FWHM (Figure 8, middle panel), we fit a simple linear function (first-order polynomial) to the PSF FWHM of *griz* bands to interpolate/extrapolate the PSF FWHM value at other wavelengths. The average absolute difference between the reconstructed PSF FWHM values recorded in the IFU data header and the PSF FWHM values from the fitted linear function is 0.″007 with a standard deviation of 0.″006, calculated from all the MaNGA IFU data.

Considering the error of the reconstructed PSF FWHM of MaNGA IFU data (1%–2% or 0.025–0.05 in arcsec; Law et al. 2016), we conclude that the PSF FWHM from the fitted linear function gives a reasonable PSF FWHM at each wavelength bin. The distribution of the slope of the fitted linear functions is shown in the right panel of Figure 8.

4.2. Measurements of Kinematic Parameters

We measure the LOS velocity and the velocity dispersion from 4425 unique MaNGA galaxies. The measurement procedure is similar to the procedure that is described in Section 3.3, but with several differences. Instead of using one single stellar population model template, we use 156 single stellar population model SED templates from the MILES stellar library (Sánchez-Blázquez et al. 2006; Vazdekis et al. 2010; Falcón-Barroso et al. 2011) generated by using a unimodal initial mass function (Vazdekis et al. 1996) and Padova+00 isochrones (Girardi et al. 2000), age from 1 to 17.78 Gyr, and metallicity (Z) from −2.32 to 0.22 (26 ages × 6 metallicities = 156). We use an option to use sixth-order additive and multiplicative Legendre polynomials during the fitting to account for the low-order difference and offset between the MILES model and data. We mask the spectrum

[5] https://www.sdss.org/dr15/manga/manga-caveats/

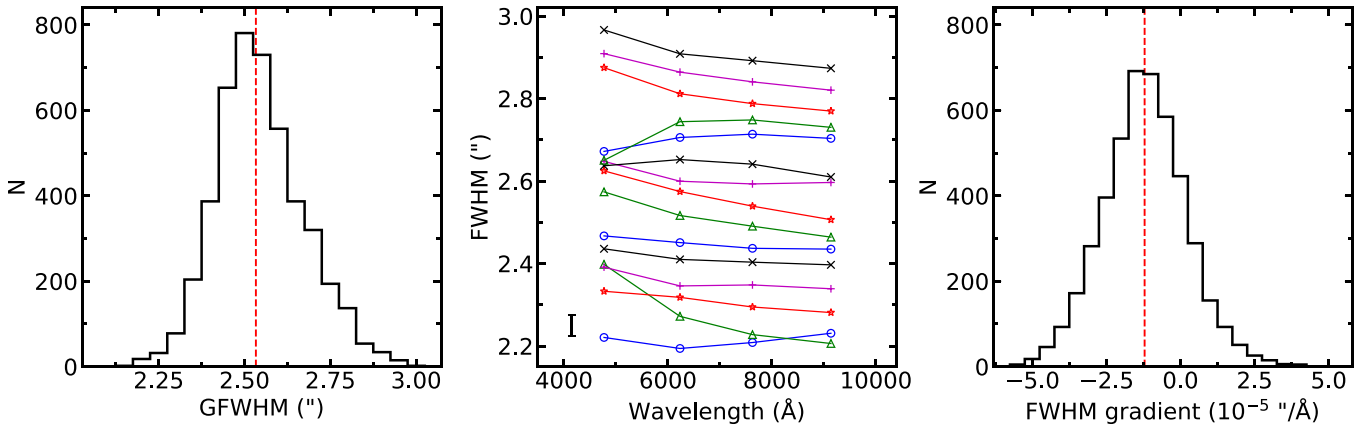

Figure 8. Left: distribution of the reconstructed FWHM in *g* band. The median value is 2.″53. Middle: wavelength-dependent $\mathrm{FWHM_{PSF}}$ of the selected MaNGA galaxies. Each connected line represents the *griz* FWHM of the PSF from a particular sample. Samples are randomly selected for illustrative purposes. The error bar shows a ±0.″025 range (1% of 2.″5). Right: distribution of wavelength-dependent FWHM gradient. The gradient is obtained by fitting a linear function to the reconstructed FWHM at *griz* bands. The median value is -1.21×10^{-5} arcsec Å^{-1}.

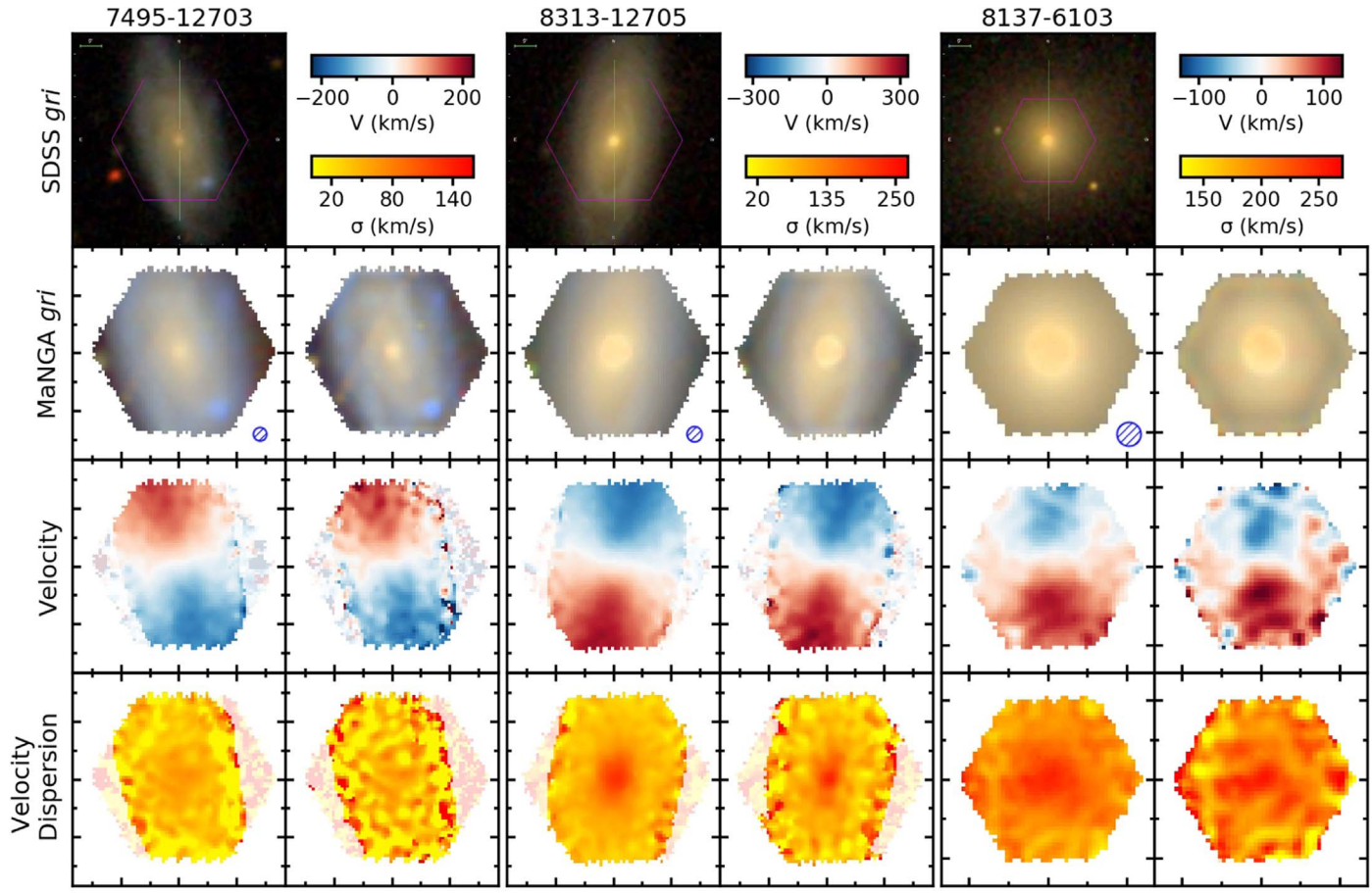

Figure 9. The results of the PSF deconvolution on three MaNGA galaxies. The number at the top of each SDSS *gri* image is the PLATE-IFU designation of a given galaxy. For each galaxy, images in the left column show reconstructed MaNGA *gri* image, velocity, and velocity dispersion distribution obtained from the *original* MaNGA data. Images in the right column are those from the PSF-*deconvolved* MaNGA data. The hatched blue circle represents the PSF FWHM size of each galaxy. Spaxels with median $\mathrm{S/N_{pPXF}} < 3$ are paled out in the velocity and velocity dispersion distributions. Each major tick interval corresponds to 10″.

pixels around the known emission lines. Model SED templates are convolved with a Gaussian function to match the spectrum resolution of MaNGA data as provided in the SPECRES HDU.

4.3. Results

Figure 9 shows the result of deconvolution applied to three of the MaNGA galaxies as an example (PLATE-IFU: 7495–12703, 8313–12705, 8137–6103). These galaxies are chosen based on their shape of the RC and the velocity dispersion profile. Each reconstructed *gri* image obtained from the deconvolved MaNGA (Deconv) data shows a noticeable difference compared to the reconstructed *gri* image from the original MaNGA (*Ori*) data. The MaNGA-Deconv data show more sharpened substructures. The restored substructures are

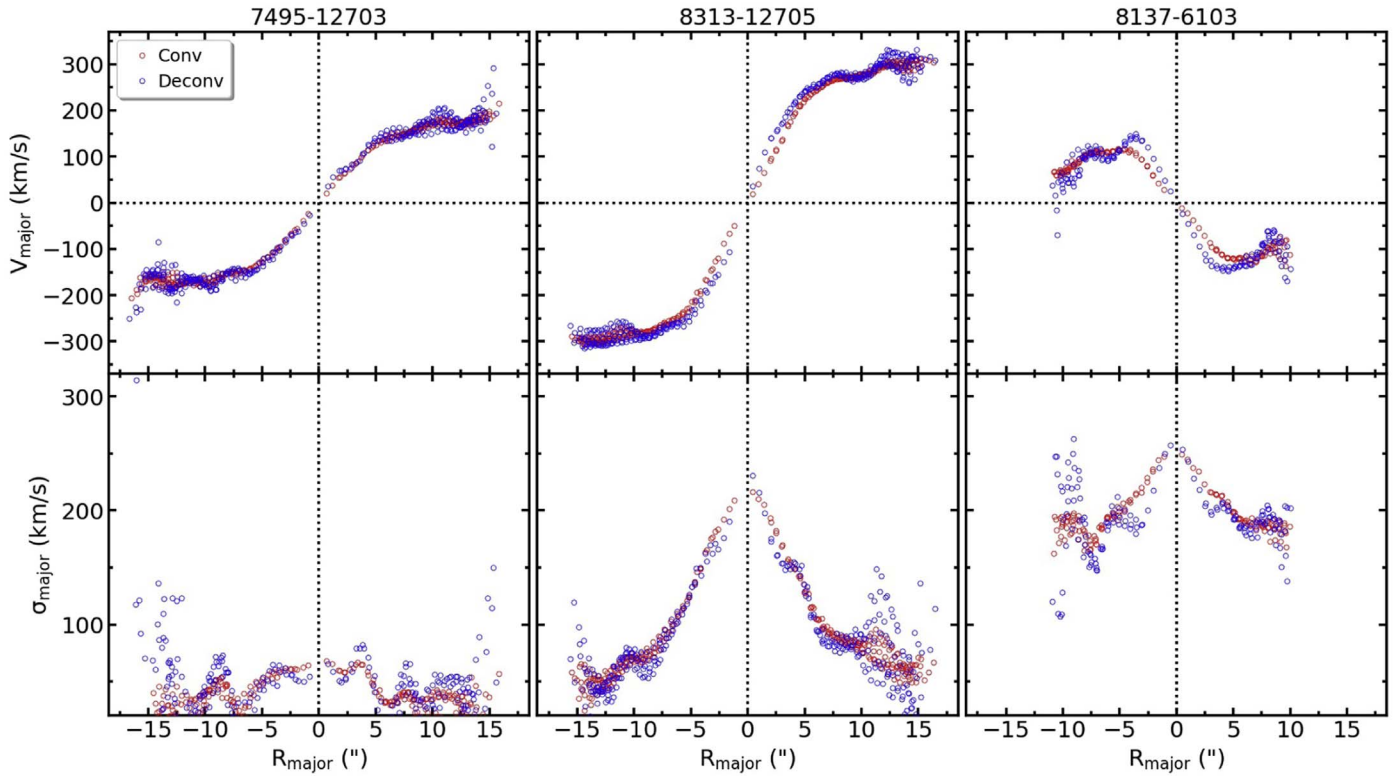

Figure 10. The velocity and velocity dispersion profiles from the original and deconvolved MaNGA data. Only the data points from $\pm 10°$ of the major axis with median $S/N_{pPXF} > 3$ are shown for clarity.

not artifacts created by the deconvolution method but are actual substructures that can be seen in the SDSS *gri* image that has higher spatial resolution. The velocity distribution also shows the apparent change, especially around the center of galaxies (i.e., the velocity gradient becomes steeper). The velocity dispersion exhibits some changes as well and shows narrower dispersion distribution near the center and sharper substructures. The restored substructures can be understood intuitively as a result of deconvolution. The difference between MaNGA-*Ori* and MaNGA-Deconv data can be seen more prominently in Figure 10. The figure clearly exhibits the changes in the velocity and the velocity dispersion distribution along the galaxy major axis.

5. Measurement of the Spin Parameter

In this section, we investigate the reliability of the λ_R parameter measured from the deconvolved IFU data. λ_R is a proxy of the spin parameter λ. It is calculated from the luminosity-weighted first and second velocity moments as in Emsellem et al. (2007),

$$\lambda_R \equiv \frac{\langle R|V|\rangle}{\langle R\sqrt{V^2+\sigma^2}\rangle} = \frac{\Sigma_{i=1}^{N} F_i R_i |V_i|}{\Sigma_{i=1}^{N} F_i R_i \sqrt{V_i^2+\sigma_i^2}}, \quad (5)$$

where F_i, R_i, V_i, and σ_i are flux, radius of the concentric ellipse, LOS velocity, and LOS velocity dispersion at the ith spatial bin, respectively. λ_R is widely used in various applications, such as kinematic classification of galaxies (Emsellem et al. 2011; Cortese et al. 2016; van de Sande et al. 2017; Graham et al. 2018), measurement of the angular momentum of merger remnants (Jesseit et al. 2009), and the studies of the environmental dependence of galaxy spin (Greene et al. 2018; Lee et al. 2018). There are also studies investigating the origin of fast and slow rotators (Naab et al. 2014; Penoyre et al. 2017), and the evolution of galaxy kinematics by using spin parameter (λ_R or V/σ) and simulation data (Choi & Yi 2017; Lagos et al. 2017; Choi et al. 2018; Martin et al. 2018). In particular, van de Sande et al. (2019) provide comprehensive analysis on the dynamical parameter measured from both observation and simulation though using V/σ instead of λ_R.

Typically λ_R is calculated by using the information within galaxy half-light radius (equivalent to the $R_e^{\rm major}$; Hopkins et al. 2010; Cappellari et al. 2013) and denoted as λ_{R_e}. It is known that λ_{R_e} is mainly correlated with two parameters: inclination angle (ϵ, as axis ratio) and FWHM of PSF that is convolved in data, because distributions of F_i, R_i, V_i, and σ_i are much affected by those parameters (Cappellari 2016; Graham et al. 2018).

There were several attempts to mitigate the effect of the PSF on λ_{R_e} measurement: (1) by correcting λ_{R_e} by $1/\sqrt{\epsilon}$ (Emsellem et al. 2011; D'Eugenio et al. 2013; Cortese et al. 2016; Greene et al. 2018) or (2) by applying an empirical correction function such as Graham et al. (2018, hereafter G18) and Harborne et al. (2020, hereafter H20). The empirical correction function provides a convenient way to correct the PSF effect to a certain parameter. Generally these functions are derived based on galaxies from a model or simulation. Therefore, those functions have nonnegligible dependence on the galaxy model or simulation used. In other words, the form or coefficient of those functions will be different if such a function is generated using other model/simulated galaxies. Those correction functions should be used with caution because they can often undercorrect or overcorrect such a parameter when they are

applied to the real galaxies. In addition, the equation should be used within a certain boundary condition such as a range of Sérsic index.

Here we show that our deconvolution method can also be used to accurately measure λ_{R_e}. In Section 5.1, we measure λ_{R_e} from the Group 3 Monte Carlo mock IFU data (Free, Conv, Deconv) and compare the λ_{R_e} measured from each type of the mock IFU data. From the result, we find that the λ_{R_e} value measured from the deconvolved IFU data is close to the true λ_{R_e}. We also check the amount of change induced by G18 and H20 correction functions using our mock data. Note that we use a different definition of R_i in Equation (1) compared to G18. In G18, R_i is defined as the circularized radius, but in our work we define R_i as the semimajor axis radius of an ellipse that passes through each spaxel (elliptical radii). The definition in G18 is the same as the original definition of λ_{R_e} in Emsellem et al. (2007), as well as in Greene et al. (2018). The other definition (semimajor axis) was used in some other studies (Cortese et al. 2016; van de Sande et al. 2017; Lee et al. 2018). The difference between the two definitions is the different weighting of the kinematics around the minor axis. Generally, for regular rotators, this weighting is not a major contributor to the λ_{R_e} calculation because the LOS velocity around the minor axis is small owing to the projection effect. H20 provides two forms of correction function for both definitions of R_i. In this study, we use the H20 correction function with the R_i defined as the semimajor axis radius. H20 also showed that the corrected λ_{R_e} value by both forms of correction function are similar to the true value when applied to λ_{R_e} measured with elliptical radii. Contrary to the seeing correction of λ_{R_e} using the empirical function, measurement of λ_{R_e} using the deconvolved IFU data is completely independent from any galaxy model. In Section 5.2, we measure λ_{R_e} from both MaNGA-*Ori* and MaNGA-Deconv and examine the differences. Finally, in Section 5.3, we test the validity of the λ_{R_e} value measured from the deconvolved IFU data by using the actual MaNGA data as a proxy of PSF-Free data. We consider MaNGA DR15 data as a seeing-free ground truth and generate PSF-convolved and PSF-deconvolved IFU data from the original MaNGA data. We present the difference between λ_{R_e} values measured from the original MaNGA IFU data and PSF-convolved/deconvolved data.

5.1. Verification Using Mock Data

We calculate λ_{R_e} following Equation (5), by using the reconstructed *r*-band flux, the velocity, and the velocity dispersion distribution measured from the Free, Conv, and Deconv Monte Carlo mock IFU data (Group 3, 40,000 IFU data each; see Section 3.2 and Table 2). The area for the λ_{R_e} calculation is defined as the spaxels within an ellipse where the semimajor axis radius is R_e. We also calculate the corrected λ_{R_e} value by applying the correction function in G18 to the $\lambda_{R_e}^{\rm Conv}$ value to compare the result between the corrected value and the value measured from the deconvolved IFU data. To apply correction functions of G18 and H20, we use $n_{\rm Sérsic}^{\rm Free}$, $R_e^{\rm Free}$, and $\rm FWHM_{PSF}$ at the *r*-band pivot wavelength (6231 Å). $R_e^{\rm Free}$ should be used instead of $R_e^{\rm Conv}$. This is because both correction functions assume that such a seeing-corrected R_e value is available from a high-resolution seeing-free image or obtained by a fitting method that calculates seeing-corrected R_e (e.g., multi-Gaussian expansion fitting; Emsellem et al. 1994; Cappellari 2002).

First, we check the ratio between the calculated λ_{R_e} values ($\lambda_{R_e}^{\rm Conv}$, $\lambda_{R_e}^{\rm Deconv}$, $\lambda_{R_e}^{\rm G18\ Corr.}$, and $\lambda_{R_e}^{\rm H20\ Corr.}$) and the true λ_{R_e} value ($\lambda_{R_e}^{\rm Free}$), as a function of true $\lambda_{R_e}^{\rm Free}$ value. In our mock IFU data, the angular size of R_e is determined by the combination of IFU FOV and radial coverage in R_e (Table 2, Appendix A). Thus, we divide the result depending on three parameters of mock IFU data, (1) $n_{\rm Sérsic}$ (1, 2, 3, 4), (2) IFU FOV (12″–32″), and (3) radial coverage in R_e (1.5 R_e and 2.5 R_e). We plot the relation between the calculated ratios to the $\lambda_{R_e}^{\rm Free}$ of each divided result. Figure E1 is shown as an example of the result for the mock IFU data with $n_{\rm Sérsic} = 1$ and 4 and IFU FOV = 1.5 R_e and 2.5 R_e. To illustrate the overall dependence of the ratio on the $n_{\rm Sérsic}$ and the size of R_e, we take the median of the ratios and the median of the standard deviation of the ratios at each bin (per $\Delta\lambda_{R_e}^{\rm Free} = 0.1$) in each panel of Figure E1. We plot the median of the ratios and the median of the standard deviation of the ratios as a function of $\sigma_{\rm PSF}/R_e^{\rm maj}$, where $\sigma_{\rm PSF} = \rm FWHM_{PSF}/2.355$. $\sigma_{\rm PSF}/R_e^{\rm maj}$ is calculated from each combination of IFU FOV and the radial coverage. For example, the rightmost filled circle red data point in the leftmost panel in Figure 11 ($\sigma_{\rm PSF}/R_e^{\rm maj} = 0.276$, $\lambda_{R_e}^{\rm Conv}/\lambda_{R_e}^{\rm Free} = 0.82 \pm 0.03$) is derived from the top left panel of Figure E1 ($n_{\rm Sérsic} = 1$, IFU FOV = 12″ (=1.5 R_e)) by taking the median and the median of 1σ of the binned relation. Note that the actual $\sigma_{\rm PSF}/R_e^{\rm maj}$ of each combination of IFU FOV and the radial coverage is not a constant. This is because $\rm FWHM_{PSF}$ of the Group 3 IFU data is slightly different for each mock IFU datum as $2\farcs6 \pm 0\farcs3$. Since R_e is different for each combination of IFU FOV and the radial coverage, the difference caused by $\rm FWHM_{PSF}$ is also different for each combination of IFU FOV and the radial coverage (e.g., $\Delta(\sigma_{\rm PSF}/R_e^{\rm maj}) = \pm 0.04$ for IFU FOV = 12″ and radial coverage = 2.5 R_e). Nevertheless, Figure 11 could still be used to show the dependence of $\lambda_{R_e}^{\rm Conv}/\lambda_{R_e}^{\rm Free}$ with respect to $\sigma_{\rm PSF}/R_e^{\rm maj}$.

Figure 11 shows that $\lambda_{R_e}^{\rm Conv}$ deviates significantly from $\lambda_{R_e}^{\rm Free}$, and the amount of the deviation becomes larger as $n_{\rm Sérsic}$ increases and as $\sigma_{\rm PSF}/R_e^{\rm maj}$ increases. On the other hand, $\lambda_{R_e}^{\rm Deconv}$ is strikingly well restored to the correct value ($\lambda_{R_e}^{\rm Free}$), although there is some deviation when $\sigma_{\rm PSF}/R_e^{\rm maj}$ is greater than 0.2. When $\sigma_{\rm PSF}/R_e^{\rm maj}$ is less than 0.2, the fractional difference between $\lambda_{R_e}^{\rm Deconv}$ and $\lambda_{R_e}^{\rm Free}$ is less than 3%, with less than 4.6% point standard deviation. We find that the corrected λ_{R_e} by the G18 or H20 correction function is also close to the correct value compared to the uncorrected λ_{R_e}. However, the fractional difference versus $\sigma_{\rm PSF}/R_e^{\rm maj}$ shows that different trends depend on $n_{\rm Sérsic}$. G18 correction works best when galaxy $n_{\rm Sérsic} = 1$. On the contrary, H20 correction works best when galaxy $n_{\rm Sérsic} = 4$. This discrepancy is most likely due to the difference of the galaxy model used between this study, G18, and H20.

We would like to note that the fractional difference ($\lambda_{R_e}^{\rm Deconv}/\lambda_{R_e}^{\rm Free}$) also shows some dependence on $n_{\rm Sérsic}$. The fractional difference is decreased (i.e., $\lambda_{R_e}^{\rm Deconv}$ is under-corrected) when $n_{\rm Sérsic}$ value increases. This could be due to the fact that the deconvolution method is working less effectively when the original flux distribution has a steeper gradient (see figures in Appendix C). On the contrary, the result in Figure 15 shows the opposite trend where the $\lambda_{R_e}^{\rm Deconv}$ values measured from high $n_{\rm Sérsic}$ values are closer to the true λ_{R_e} value. We discuss this discrepancy in Section 5.3.

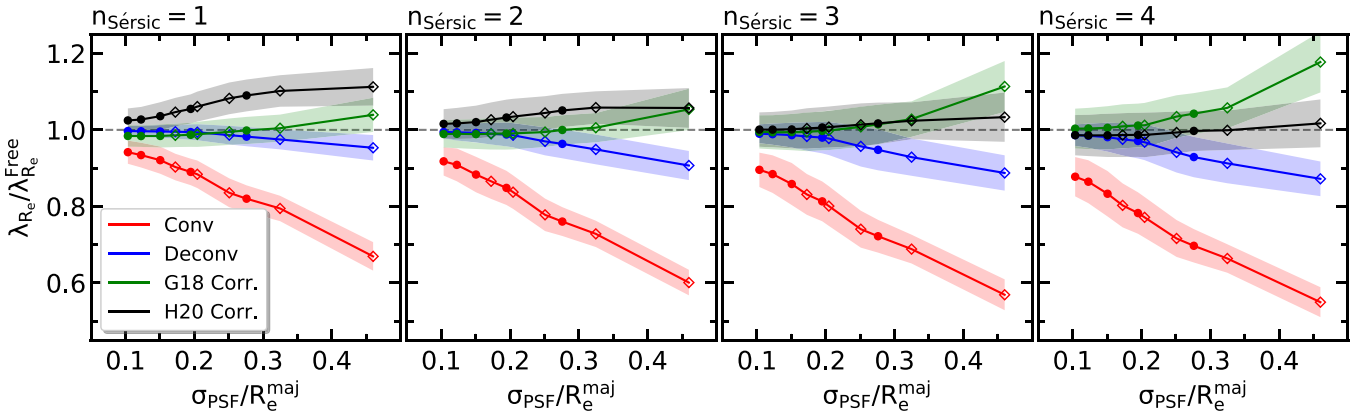

Figure 11. Ratio between the true and the measured/corrected spin parameter λ_{R_e} depending on $n_{\rm Sérsic}$ and $\sigma_{\rm PSF}/R_e^{\rm maj.}$. The leftmost panel shows the ratio measured from the Group 3 mock IFU data (Table 2) with $n_{\rm Sérsic} = 1$. Other panels show the result from mock IFU data with $n_{\rm Sérsic} = 2$, 3, 4. Filled circles are estimated from mock IFU data with radial coverage = 1.5 R_e, and the open diamonds are estimated from mock IFU data with IFU radial coverage = 2.5 R_e.

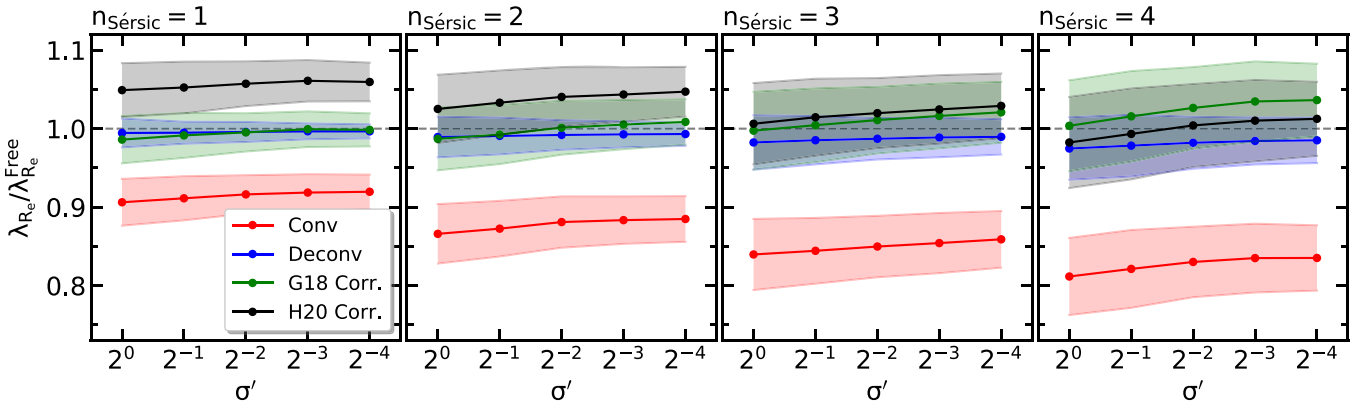

Figure 12. Ratio between the true and the measured/corrected spin parameter λ_{R_e} depending on $n_{\rm Sérsic}$ and velocity dispersion profile coefficient σ_1. The leftmost panel shows the ratios measured from the Group 3–like mock IFU data set (Table 2, all with 32″ FOV and radial coverage of 2.5 $R_{\rm e}$ with $n_{\rm Sérsic} = 1$), depending on velocity dispersion profile coefficient $\sigma_1 = 1$, 0.5, 0.25, 0.125, 0.0625. Other panels show the results from mock IFU data with $n_{\rm Sérsic} = 2$, 3, 4.

In addition, we have checked whether there is an unexpected dependency of the result due to the realism of the equal variety of kinematics used for the mock IFU data. Since the deconvolution method itself is a data processing procedure that is independent of the realism of the model used for the verification, the flux or kinematic distribution should be recovered close to the true distribution regardless of the realism of the original flux or kinematic distribution. As expected, there are no noticeable differences between the blue curve in Figure 11 depending on $V_{\rm ROT}$ or σ_0 values of the mock galaxy.

We conducted an additional test with a different set of mock data that have a slightly modified 2D velocity dispersion distribution profile. The Group 3 mock data set is constructed with the velocity dispersion profile of only $\sigma' = 1$, where the velocity dispersion drops sharply between the center and $r = R_1$ (Equation (3), Table 2). However, the velocity dispersion profile of the actual galaxy does not always follow the same shape. For example, in Figure 10, when we fit Equation (3) to the velocity dispersion profile, MaNGA data 8313–12705 (PLATE-IFU) are well described by $\sigma' = 1$. On the other hand, the velocity dispersion profile of MaNGA data 7495–12703 is not well fitted by Equation (3), and for MaNGA data 8137–6103, the best-fit σ' value is around 0.44, which is fairly different compared to the MaNGA data 8313–12705 case.

To further explore the performance of deconvolution to the λ_{R_e} calculation on a different velocity dispersion profile, we construct an additional mock IFU data set similar to Group 3 mock IFU data but with different σ' values and additional $n_{\rm Sérsic}$ values. The additional data set is composed of $\sigma' = 1$, 0.5, 0.25, 0.125, 0.0625 (2^0, 2^{-1}, 2^{-2}, 2^{-3}, 2^{-4}) and $n_{\rm Sérsic} = 1$, 2, 3, 4. A smaller σ' value means a less steep velocity dispersion profile. For example, if $\sigma' = 0.1$, then $\sigma_{r=R_1}/\sigma_{r=0} = 0.91$, but if $\sigma' = 1$, then $\sigma_{r=R_1}/\sigma_{r=0} = 0.5$. For each combination of σ' and $n_{\rm Sérsic}$ ($5 \times 4 = 20$), 4000 mock IFU data are generated randomly in the Monte Carlo way just like Group 3 mock IFU data but with a fixed IFU FOV as 32″ and IFU radial coverage as 2.5 $R_{\rm e}$, meaning that the ratio between $\rm FWHM_{PSF}$ and $R_{\rm e}$ is relatively fixed for this data set ($\sigma_{\rm PSF}/R_{\rm e}^{\rm maj} \sim 0.17$), compared to the overall Group 3 mock IFU data. In total, 80,000 Free, 80,000 Conv, and 80,000 Deconv IFU data are produced as this additional test. This data set is analyzed in the same way as Group 3 mock IFU data, and λ_{R_e} values ($\lambda_{R_e}^{\rm Free}$, $\lambda_{R_e}^{\rm Conv}$, $\lambda_{R_e}^{\rm Deconv}$, $\lambda_{R_e}^{\rm G18Corr.}$, $\lambda_{R_e}^{\rm H20Corr.}$) from this data set are calculated.

First, we check the relation between the ratios ($\lambda_{R_e}^{\rm Conv}/\lambda_{R_e}^{\rm Free}$, $\lambda_{R_e}^{\rm Deconv}/\lambda_{R_e}^{\rm Free}$, $\lambda_{R_e}^{\rm G18Corr.}/\lambda_{R_e}^{\rm Free}$, $\lambda_{R_e}^{\rm H20Corr.}/\lambda_{R_e}^{\rm Free}$) and the true λ_{R_e} value ($\lambda_{R_e}^{\rm Free}$) as in Figure E2. Then, we plot Figure 12 in the same way as we did for Figure 11. Again, the result shows that $\lambda_{R_e}^{\rm Conv}$ deviates considerably from $\lambda_{R_e}^{\rm Free}$, and the amount of the

deviation becomes larger as $n_{\rm Sérsic}$ increases, with a mild dependence on the σ' value. Moreover, $\lambda_{R_e}^{\rm Deconv}$ is still well restored to the correct value ($\lambda_{R_e}^{\rm Free}$) for all combinations of σ' and $n_{\rm Sérsic}$, with the fractional difference between $\lambda_{R_e}^{\rm Deconv}$ and the correct value less than 1% and less than 1.9% point standard deviation.

On the other hand, $\lambda_{R_e}^{\rm G18Corr.}$ and $\lambda_{R_e}^{\rm H20Corr.}$ show noticeable dependence on the σ' value for all four $n_{\rm Sérsic}$ cases, where the deviation increases as the σ' decreases. The reason for the deviation of $\lambda_{R_e}^{\rm G18Corr.}$ or $\lambda_{R_e}^{\rm H20Corr.}$ could be because of the shape of the velocity dispersion profile covered by the model galaxy used by G18 or H20, if the model galaxies did not include velocity dispersion distribution close to flat. In Section 3.4.1, we discuss the effect of PSF convolution on the velocity dispersion distribution. When there is a small gradient of the velocity dispersion profile (i.e., smaller σ'), the amount of smoothing effect on the velocity dispersion around the center will also be smaller, so the velocity dispersion around the center will be increased relatively less than the case of a steep velocity dispersion gradient profile. Thus, the amount of change in the λ_{R_e} value caused by PSF convolution will be smaller if the velocity dispersion profile has a lower gradient. The dependence of $\lambda_{R_e}^{\rm Conv}$ on σ' shows the expected trend in Figure 12, which implies that the G18 correction function overcorrects the $\lambda_{R_e}^{\rm Conv}$ value.

5.2. Application to MaNGA Data

We measure λ_{R_e} by using both the original and the PSF-deconvolved MaNGA data, and we investigate the difference in the measured λ_{R_e} values that is induced by the deconvolution. We use 2D velocity and the velocity dispersion distribution (Section 4.2), along with the reconstructed MaNGA r-band flux data of 4426 MaNGA galaxies that we measured in Section 4. We use "NSA_ELPETRO_TH50_R," "NSA_ELPETRO_BA," "NSA_ELPETRO_PHI," "IFURA/IFUDEC," and "OBJRA/OBJDEC" in the FITS header of each galaxy IFU datum to evaluate the concentric ellipse of each. To ensure the quality of measured λ_{R_e}, we did not include certain spaxels in the λ_{R_e} calculation when a spaxel has (1) median $S/N_{\rm pPXF} < 10$ or (2) velocity dispersion $<40\,{\rm km\,s^{-1}}$, following the prescription of Lee et al. (2018). We also did not include spaxels with spurious kinematics to the λ_{R_e} calculation, where the absolute value of velocity is greater than $500\,{\rm km\,s^{-1}}$ or the velocity dispersion is less than $50\,{\rm km\,s^{-1}}$. When the number fraction of the excluded spaxels within $1R_{\rm e}$ becomes larger than 30%, we do not use the λ_{R_e} from that galaxy for further analysis. Although we use the same elliptical aperture for the measurement of both $\lambda_{R_e,{\rm MaNGA}}$ and $\lambda_{R_e,{\rm MaNGA,Deconv.}}$, the number of spaxels used for each measurement is not always identical because of $S/N_{\rm pPXF}$ and velocity dispersion criteria. We also exclude the galaxies flagged with "CRITICAL" by the MaNGA Data Reduction Pipeline or Data Analysis Pipeline (Law et al. 2016; Westfall et al. 2019). These criteria would be sufficient to observe the impact of deconvolution on λ_{R_e} for the real data. We note that more strict quality control criteria should be applied for the further analysis using λ_{R_e} (Lee et al. 2018; Graham et al. 2018). The number of galaxies having both quality-assured $\lambda_{R_e,{\rm MaNGA}}$ and $\lambda_{R_e,{\rm MaNGA,Deconv.}}$ is 2268. We present the relation between the $\lambda_{R_e,{\rm MaNGA}}$ and the $\lambda_{R_e,{\rm MaNGA,Deconv.}}$ in the leftmost panels of Figure 13 depending on $n_{\rm Sérsic}$ of the MaNGA galaxies (NSA_SERSIC_N). Compared to the $\lambda_{R_e,{\rm MaNGA}}$, most of the $\lambda_{R_e,{\rm MaNGA,Deconv.}}$ values are moderately increased for both $n_{\rm Sérsic}$ ranges. The median and standard deviation of $\Delta\lambda_{R_e}$ is 0.044 ± 0.046, or a median increase of 8% with 18% point standard deviation for galaxies with $n_{\rm Sérsic} < 2$. The median and standard deviation of $\Delta\lambda_{R_e}$ is 0.055 ± 0.045, or a median increase of 37% with 26% point standard deviation for galaxies with $n_{\rm Sérsic} \geqslant 2$. Note that the fractional difference is larger for the galaxies with $n_{\rm Sérsic} \geqslant 2$ because the majority of $n_{\rm Sérsic} \geqslant 2$ galaxies have relatively small λ_{R_e} values compared to $n_{\rm Sérsic} < 2$ galaxies. We also check the correlation between the two ratios ($\lambda_{R_e,{\rm MaNGA}}/\lambda_{R_e,{\rm MaNGA,Deconv.}}$ and $\rm FWHM_{PSF}/R_e$), and as expected from the result with mock IFU data, $\lambda_{R_e,{\rm MaNGA,Deconv.}}/\lambda_{R_e,{\rm MaNGA}}$ increases as $\rm FWHM_{PSF}/R_e$ increases.

During the validity check of the calculated λ_{R_e}, we find tens of galaxies or more for which their λ_{R_e} do not seem measured correctly. There are several such cases, for example:

1. There are seven galaxies in Figure 13 that have both $\lambda_{R_e,{\rm MaNGA}}$ and $\lambda_{R_e,{\rm MaNGA,Deconv.}} > 0.8$. However, all of those galaxies' systematic velocities are highly underestimated or overestimated; in other words, galaxy systematic velocity derived by the NSA redshift is not matching with the true systematic velocity. After correcting its systematic velocity, it turns out that their λ_{R_e} value is significantly less than 0.8.
2. There are galaxies with foreground/background objects, either stars or other galaxies, at or around the $1R_e$ elliptical aperture. Some of them are already masked by the MaNGA data reduction pipeline, but still there are tens of IFU data with unmasked interloper. Either masked or unmasked, the interloping object disrupts the kinematics measurement in particular at the border between the object of interest and the interloper.
3. Contrary to the sample definition of MaNGA galaxies, there are galaxies where their $R_{\rm e}$ size is comparable to the IFU FOV. This brings spaxels at the edge of the IFU FOV to the λ_{R_e} calculation. Since the kinematics measured at near the edge of the deconvolved IFU data could be different from the correct value, the calculated λ_{R_e} from such a galaxy sample is not reliable.
4. IFU data with small FOV (i.e., 12″) often include only tens of spaxels in λ_{R_e} calculation. This means that even a small offset at its center position or systematic velocity can lead to considerable change in the measured λ_{R_e} value. These suggest that more careful data quality assurance is required to assure the data with a correctly measured λ_{R_e} value.

We also plot the relation between the $\lambda_{R_e,{\rm MaNGA}}$ and the corrected λ_{R_e} (following G18 and H20) in Figure 13. Compared to $\Delta\lambda_{R_e}$ caused by the deconvolution method, the $\Delta\lambda_{R_e}$ caused by G18 correction is higher. Sometimes the corrected value becomes higher than $\lambda_{R_e} = 1$, which is nonphysical. As noticed in Section 5.1, the overcorrection could be due to the different shape of the velocity dispersion profile of the real galaxy compared to the profile used to derived the correction function, or some other unanticipated model-dependent bias. For example, the data points in Figure 4 of G18 show that the difference in λ_{R_e} caused by the PSF convolution is larger with model galaxies compared to the real (ATLAS$^{\rm 3D}$) galaxies. This shows that the G18 correction function could overcorrect the λ_{R_e} values when applied to the real galaxies. Compared to the $\Delta\lambda_{R_e}$ caused by the deconvolution method, the $\Delta\lambda_{R_e}$ caused

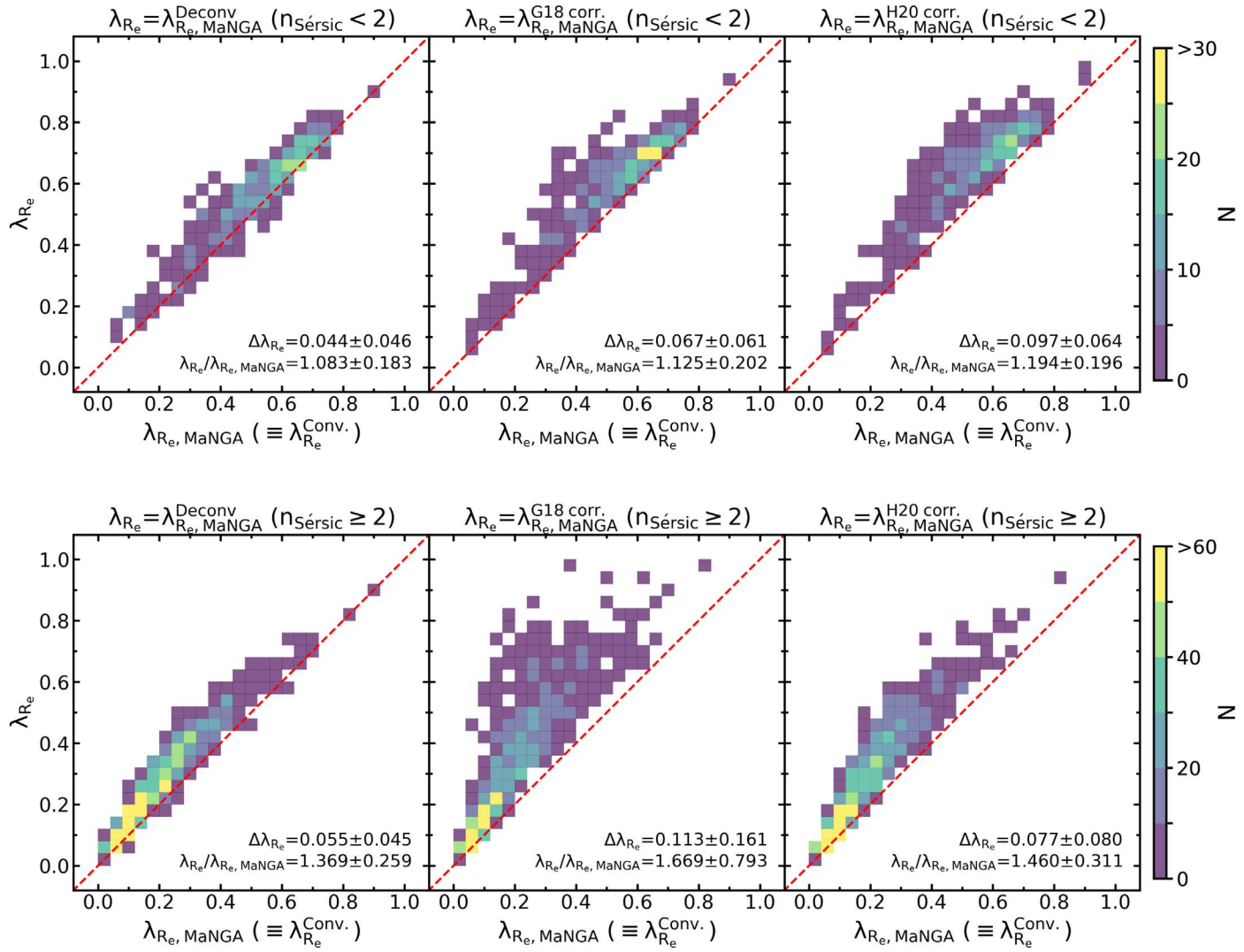

Figure 13. Top panels: each panel shows the comparison between the λ_{R_e} measured from the original MaNGA IFU data and the λ_{R_e} measured from the deconvolved MaNGA IFU data (left), the λ_{R_e} corrected by following G18 (middle), and the λ_{R_e} corrected by following H20 (right), using the MaNGA galaxies with $n_{\rm Sérsic} < 2$. Distributions of points are shown as 2D histograms. Bottom panels: same as the top panels, but using the MaNGA galaxies with $n_{\rm Sérsic} \geqslant 2$.

by H20 correction is also higher. The $\Delta\lambda_{R_e}$ caused by H20 correction is larger than the $\Delta\lambda_{R_e}$ caused by G18 when $n_{\rm Sérsic} < 2$, but smaller than the $\Delta\lambda_{R_e}$ caused by G18 when $n_{\rm Sérsic} \geqslant 2$.

To better understand this $n_{\rm Sérsic}$ dependence, we plot $\lambda_{R_e,\rm MaNGA}/\lambda^{\rm Deconv.}_{R_e,\rm MaNGA}$ versus $\sigma_{\rm PSF}/R_e^{\rm maj.}$ in Figure 14, which is another representation of Figure 13. In Figure 14, the difference between the data points and the red dashed line ($\lambda_{R_e,\rm MaNGA}/\lambda^{\rm Deconv.}_{R_e,\rm MaNGA} = 1$) indicates the amount of λ_{R_e} difference caused by the deconvolution. When $n_{\rm Sérsic} = 1$, the $\lambda_{R_e,\rm MaNGA}/\lambda^{\rm Deconv.}_{R_e,\rm MaNGA}$ distribution is similar to the green line, which is G18 correction. In other words, the amount of correction made by G18 correction is similar to the amount of λ_{R_e} change made by the deconvolution method. Black lines in the $n_{\rm Sérsic} = 1$ panel of Figure 14 are located below the green line, meaning that if H20 correction is applied to $\lambda_{R_e,\rm MaNGA}$, then the corrected value will be higher than the value corrected by G18. The inverse of the H20 correction function for the λ_{R_e} value calculated by using circularized radii is also shown as blue lines. The amount of correction by H20 correction using the definition of circularized radii (blue dashed line) is similar to G18 correction (green line) when the ellipticity is unity. When the ellipticity is zero, G18 corrections with definitions of both elliptical and circularized radii (black and blue solid lines) are identical to each other. This is because elliptical radii are the same as circularized radii when the ellipticity is zero.

On the contrary, when $n_{\rm Sérsic} = 4$, the black lines are closer to the $\lambda_{R_e,\rm MaNGA}/\lambda^{\rm Deconv.}_{R_e,\rm MaNGA}$ distribution, whereas the green line is located below the black lines. This result aligns with the result in Figure 11, where the λ_{R_e} corrected by G18 correction is similar to the λ_{R_e} measured from deconvolved mock IFU data when $n_{\rm Sérsic} = 1$ and the λ_{R_e} corrected by H20 correction is closer to the λ_{R_e} measured from deconvolved mock IFU data when $n_{\rm Sérsic} = 4$. In other words, the difference in λ_{R_e} caused by deconvolution in the mock IFU data and the MaNGA data shows similar trends, depending on $n_{\rm Sérsic}$ and $\sigma_{\rm PSF}/R_e^{\rm maj.}$. This result indicates that the G18 or H20 correction function should be used with caution, because G18 correction could overcorrect the λ_{R_e} when $n_{\rm Sérsic} > 3$ and H20 correction could overcorrect the λ_{R_e} when $n_{\rm Sérsic} < 3$. The amount of correction by H20 correction using the definition of circularized radii (blue dashed line) is the closest to the $\lambda_{R_e,\rm MaNGA}/\lambda^{\rm Deconv.}_{R_e,\rm MaNGA}$ when the ellipticity is unity, but the amount of correction is still slightly

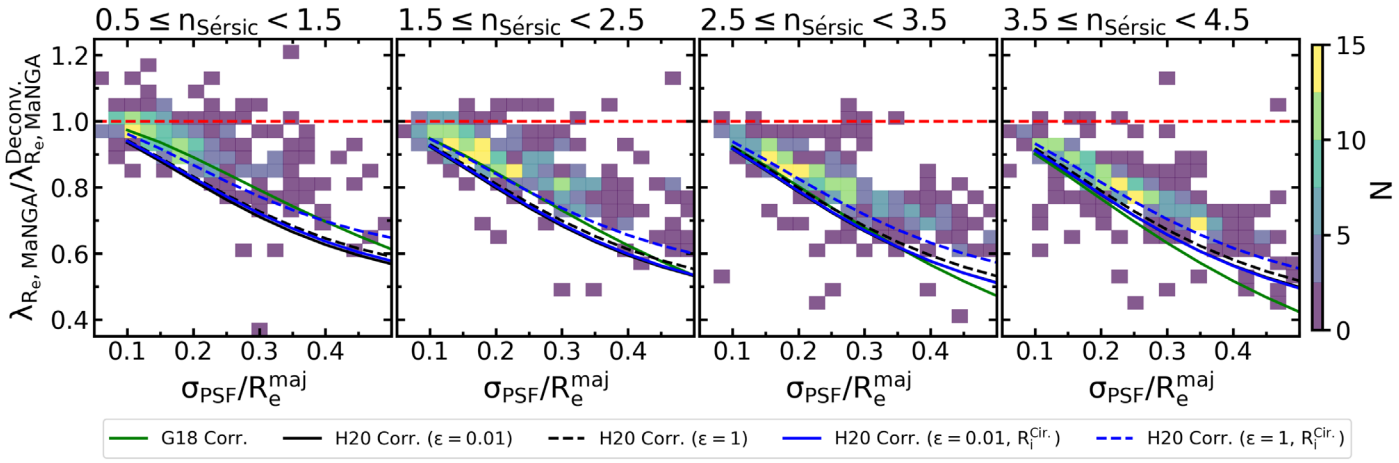

Figure 14. The ratios between the λ_{R_e} measured from the original MaNGA data and the λ_{R_e} measured from PSF-deconvolved MaNGA data, depending on $\sigma_{\rm PSF}/R_e^{\rm maj.}$. Each panel shows the 2D histogram of $\lambda_{R_e,\rm MaNGA}/\lambda^{\rm Deconv.}_{R_e,\rm MaNGA}$ vs. $\sigma_{\rm PSF}/R_e^{\rm maj.}$, when $0.5 \leqslant n_{\rm Sérsic} < 1.5$, $1.5 \leqslant n_{\rm Sérsic} < 2.5$, $2.5 \leqslant n_{\rm Sérsic} < 3.5$, and $3.5 \leqslant n_{\rm Sérsic} < 4.5$, respectively. In each panel, the overlapped lines show the inverse of G18 and H20 correction functions when $n_{\rm Sérsic}$= 1, 2, 3, and 4. The inverses of correction functions are equal to $\lambda_{R_e,\rm MaNGA}/\lambda^{\rm G18\ Corr.}_{R_e,\rm MaNGA}$ (green solid line) or $\lambda_{R_e,\rm MaNGA}/\lambda^{\rm H20\ Corr.}_{R_e,\rm MaNGA}$ (black lines for λ_{R_e} with elliptical radii, blue lines for λ_{R_e} with circularized radii). For each inverse H20 function, two inverse functions are shown, one when $\epsilon = 0.01$ (black solid line) and the other when $\epsilon = 1$ (black dashed line).

larger than the difference between $\lambda_{R_e,\rm MaNGA}$ and $\lambda^{\rm Deconv.}_{R_e,\rm MaNGA}$. The amount of correction by G18 correction (green line) and the H20 correction using the definition of circularized radii (blue lines) are expected to show similar results because both use the same definition of circularized radii. However, they show noticeable difference when $n_{\rm Sérsic} \sim 1$ or $n_{\rm Sérsic} \sim 4$. Again, this could be due to the model dependency behind the empirically derived λ_{R_e} correction functions.

Note that the model galaxies used for G18 were generated using the Jeans anisotropic modeling method (Cappellari 2008), whereas the H20 correction was made based on *N*-body galaxy models. Both G18 and H20 corrections are empirical correction functions based on model/simulation. Therefore, any difference between the model galaxy and the real galaxy could cause a bias to the parameter values corrected by those functions when such functions are applied to real data. Figures 11 and 14 show that neither G18 nor H20 correction could provide the correct λ_{R_e} value over the $n_{\rm Sérsic}$ range from 1 to 4.

5.3. Verification Using MaNGA Data

Verification of the deconvolution method using mock data allows us to test the method in more controlled samples. However, although the kinematics of the mock IFU data that we have generated is inspired by the kinematics of the real galaxies, the kinematics is described by the empirical RC model, not by a model based on physics. Nevertheless, it is also true that even the models based on physics are not sufficient to replace the kinematics of the actual galaxy. The limitation of the empirical kinematics that we used could raise the question of whether the deconvolution method is still applicable to the real galaxy. To mitigate the gap between our empirical kinematics and the real galaxy kinematics, we examined the validity of our method by using the kinematics of real galaxies.

We use the MaNGA DR15 data as a ground truth (PSF-Free) and test our deconvolution method in the same way as we did with the mock data. Although the MaNGA data are already seeing convolved, the flux and kinematic distribution is far more realistic than any empirical model or simulation. First, we generate PSF-convolved data (PSF-Conv) by convolving fixed-size PSF (FWHM = 2.″6) to MaNGA IFU data. Then, we again apply the deconvolution method to the PSF-convolved data and generate PSF-deconvolved data (PSF-Deconv). Kinematic parameters (velocity and velocity distribution) are measured from all Free, Conv, and Deconv in the same way as described in Section 4.2, and λ_{R_e} values are also measured as described in Section 5.2. The velocity and velocity distribution of the seven selected nearby MaNGA galaxies ($z < 0.023$ and IFU FOV $\geqslant 27''$) are shown in Figure E3. λ_{R_e} values measured from Free, Conv, and Deconv data of those seven galaxies are also presented.

In Figure 15, we plot the ratios between the λ_{R_e} measured from Conv and Free ($\lambda^{\rm Conv}_{R_e}/\lambda^{\rm Free}_{R_e}$) and Deconv and Free ($\lambda^{\rm Deconv}_{R_e}/\lambda^{\rm Free}_{R_e}$) as a function of $\lambda^{\rm Free}_{R_e}$ and $\sigma_{\rm PSF}/R_e^{\rm maj.}$. We only use the galaxies that passed the quality control that we applied in Section 5.2. We further exclude the galaxies that show $\Delta\lambda^{\rm Conv}_{R_e} > 0.05$ and $\lambda^{\rm Free}_{R_e} > 0.7$, because visual inspection finds that the λ_{R_e} of those galaxies are not measured correctly, due to the reasons that we noted in Section 5.2. The result is further divided depending on Sérsic index ($n_{\rm Sérsic} < 2$ and $n_{\rm Sérsic} \geqslant 2$). For galaxies with $n_{\rm Sérsic} < 2$, $\lambda^{\rm Conv}_{R_e}/\lambda^{\rm Free}_{R_e} = 0.833 \pm 0.128$ (median and standard deviation) but $\lambda^{\rm Deconv}_{R_e}/\lambda^{\rm Free}_{R_e} = 0.932 \pm 0.121$. For galaxies with $n_{\rm Sérsic} \geqslant 2$, $\lambda^{\rm Conv}_{R_e}/\lambda^{\rm Free}_{R_e} = 0.828 \pm 0.123$ but $\lambda^{\rm Deconv}_{R_e}/\lambda^{\rm Free}_{R_e} = 0.976 \pm 0.119$. Interestingly, $\lambda^{\rm Deconv}_{R_e}$ is measured more accurately for the galaxies with $n_{\rm Sérsic} \geqslant 2$ compared to the galaxies with $n_{\rm Sérsic} < 2$. This might seem in contradiction to the expectation from Figure 11, where the galaxies with $n_{\rm Sérsic} < 2$ could give $\lambda^{\rm Deconv}_{R_e}$ values closer to $\lambda^{\rm Free}_{R_e}$. However, considering the distribution of the overall data points and its standard deviation in Figure 15, it is inconclusive whether the result of Figure 15 does not align with the expectation. The main sequence of the data points shows that the fractional difference between $\lambda^{\rm Deconv}_{R_e}$ and $\lambda^{\rm Free}_{R_e}$ values is less than 0.04 dex for galaxies with $n_{\rm Sérsic} < 2$ when $\sigma_{\rm PSF}/R_e^{\rm maj.} < 0.2$. A similar fractional difference is observed from the main sequence of the data points with $n_{\rm Sérsic} \geqslant 2$ cases when $\sigma_{\rm PSF}/R_e^{\rm maj.} < 0.4$. The recovered $\lambda^{\rm Deconv}_{R_e}$ values do not show clear dependency with respect to the $\sigma_{\rm PSF}/R_e^{\rm maj.}$, but only for a limited $\sigma_{\rm PSF}/R_e^{\rm maj.}$ range owing to the insufficient data points at larger $\sigma_{\rm PSF}/R_e^{\rm maj.}$.

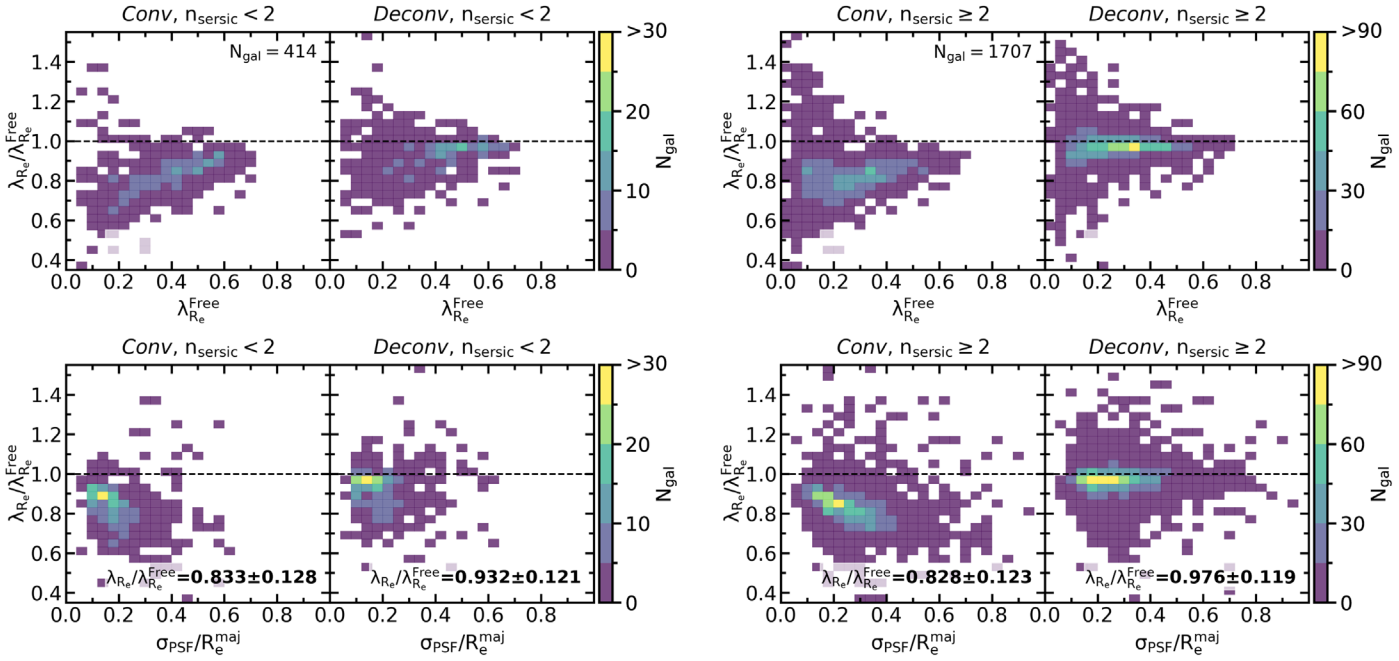

Figure 15. Comparison between the ratios of λ_{R_e} measured from PSF-Convolved or PSF-Deconvolved IFU data with respect to $\lambda_{R_e}^{\rm Free}$ and $\sigma_{\rm PSF}/R_e^{\rm maj.}$ using MaNGA DR15 galaxies as the PSF-Free data. Panels on the left show $\lambda_{R_e}^{\rm Conv}/\lambda_{R_e}^{\rm Free}$ and $\lambda_{R_e}^{\rm Deconv}/\lambda_{R_e}^{\rm Free}$ as a function of $\lambda_{R_e}^{\rm Free}$ or $\sigma_{\rm PSF}/R_e^{\rm maj.}$ for the original MaNGA galaxies with $n_{\rm Sérsic} < 2$. Panels on the right show the same as the left panels, but using the original MaNGA galaxies with $n_{\rm Sérsic} \geqslant 2$. The median and standard deviation of $\lambda_{R_e}/\lambda_{R_e}^{\rm Free}$ are noted in the bottom panels.

The result presented in Figure 15 shows that the λ_{R_e} values measured from the deconvolved data are well restored to the correct value, although the measured value ($\lambda_{R_e}^{\rm Deconv}$) is slightly (<0.04 dex.) smaller than the true λ_{R_e} value on average. Note that it is inconclusive whether $\lambda_{R_e}^{\rm Deconv}$ values are well restored when $\sigma_{\rm PSF}/R_e^{\rm maj.} > 0.4$, with this verification experiment using MaNGA data as the PSF-Free data. Considering the trend of $\lambda_{R_e}^{\rm Deconv}/\lambda_{R_e}^{\rm Free}$ in Figure 11, the $\lambda_{R_e}^{\rm Deconv}$ values could be smaller (<0.1 dex.) than the true λ_{R_e} value when $\sigma_{\rm PSF}/R_e^{\rm maj.} > 0.4$.

In Figure E4, we plotted a figure that is the same as Figure 15, but when the $\rm FWHM_{PSF}$ value for the deconvolution or λ_{R_e} correction is different from the true value by $\pm 0\farcs3$. The results give an idea of the sensitivity of the λ_{R_e} values when incorrect $\rm FWHM_{PSF}$ is used for the deconvolution or correction function. Over the tested $\rm FWHM_{PSF}$ range ($\pm 0\farcs3$), the $\lambda_{R_e}/\lambda_{R_e}^{\rm Free}$ values show the difference maximum 0.05 (5% point), whereas the $\lambda_{R_e}^{\rm Conv}$ shows over 17% difference compared to $\lambda_{R_e}^{\rm Free}$. Therefore, λ_{R_e} from the deconvolved data or corrected λ_{R_e} by the correction function still provides better values compared to the uncorrected λ_{R_e} value.

6. Summary and Conclusion

We investigate the effects of the PSF deconvolution of the optical integral field spectroscopy data on galaxies' internal kinematics. We develop a procedure to apply the LR algorithm to deconvolve IFU data. The procedure deconvolves given IFU data efficiently using only two parameters ($N_{\rm iter}$ and $\rm FWHM_{PSF}$). We generate a large number of mock data with varying Sérsic profile and the RC model and use them to verify the feasibility of the deconvolution method. Using the mock data, we have shown that the deconvolution works well on the IFU data. Contrary to the kinematics measured from PSF-convolved mock IFU data, the kinematics measured from deconvolved mock IFU data is well restored to the true kinematics of mock galaxies.

We deconvolve the mock IFU data with a wide range of a number of iterations (1–50). From the result, we have determined the number of iterations of the deconvolution procedure as 20. We also show that the deconvolution is not highly sensitive to the PSF FWHM size used for the deconvolution, although the use of accurate PSF FWHM close to the one implied in the PSF-convolved IFU data is always desired. The result from various mock IFU data shows that the deconvolution method is working on a variety of galaxy photometric/kinematic distributions. The deconvolution is powerful in the sense that it can provide an unbiased (model-independent) correction to any PSF-convolved IFU data. We apply the deconvolution to the real data, SDSS-IV MaNGA. We show that the deconvolution makes a noticeable difference in the 2D flux, the velocity, and the velocity dispersion distributions.

Finally, we demonstrate that the λ_{R_e} spin parameter can be well estimated from the PSF-deconvolved IFU data. Using the mock IFU data, we show that the λ_{R_e} can be correctly measured from deconvolved IFU data within 3%, when the ratio between the convolved PSF size ($\sigma_{\rm PSF}$) and the galaxy effective radius ($R_{\rm e}$) is less than 0.2. We measure λ_{R_e} from the PSF-deconvolved MaNGA data. The λ_{R_e} measured from the original MaNGA data and the λ_{R_e} measured from the deconvolved MaNGA data show the moderate difference compared to the difference caused by empirically driven λ_{R_e} correction functions. We generate PSF-convolved/deconvolved mock IFU data by considering the original MaNGA IFU data as perfect (PSF-Free) data. The λ_{R_e} comparison result from the experiment using the original MaNGA IFU data as perfect data shows that λ_{R_e} values measured from the PSF-deconvolved mock IFU data are close true λ_{R_e} values. Therefore, the deconvolution

method is indeed working well with the realistic IFU data as well.

We thank the anonymous referee for their detailed and constructive comments, which led to a significant improvement of this manuscript. We thank the Korea Institute for Advanced Study for providing computing resources (KIAS Center for Advanced Computation Linux Cluster System) for this work.

Funding for the Sloan Digital Sky Survey IV has been provided by the Alfred P. Sloan Foundation, the U.S. Department of Energy Office of Science, and the Participating Institutions. SDSS-IV acknowledges support and resources from the Center for High-Performance Computing at the University of Utah. The SDSS website is www.sdss.org.

SDSS-IV is managed by the Astrophysical Research Consortium for the Participating Institutions of the SDSS Collaboration including the Brazilian Participation Group, the Carnegie Institution for Science, Carnegie Mellon University, the Chilean Participation Group, the French Participation Group, Harvard-Smithsonian Center for Astrophysics, Instituto de Astrofísica de Canarias, The Johns Hopkins University, Kavli Institute for the Physics and Mathematics of the Universe (IPMU)/University of Tokyo, the Korean Participation Group, Lawrence Berkeley National Laboratory, Leibniz Institut für Astrophysik Potsdam (AIP), Max-Planck-Institut für Astronomie (MPIA Heidelberg), Max-Planck-Institut für Astrophysik (MPA Garching), Max-Planck-Institut für Extraterrestrische Physik (MPE), National Astronomical Observatories of China, New Mexico State University, New York University, University of Notre Dame, Observatário Nacional/MCTI, The Ohio State University, Pennsylvania State University, Shanghai Astronomical Observatory, United Kingdom Participation Group, Universidad Nacional Autónoma de México, University of Arizona, University of Colorado Boulder, University of Oxford, University of Portsmouth, University of Utah, University of Virginia, University of Washington, University of Wisconsin, Vanderbilt University, and Yale University.

Appendix A
Mock IFU Data Generation

In order to quantitatively examine the change made by the deconvolution, the mock IFU data should be generated correctly as per the model galaxy parameters. Here we describe the generation process of each type of mock IFU data (Free, Conv, Deconv) in detail. Initially, ideal IFU data (Free, without any seeing effect) are produced for each set of galaxy model parameters. Then, the PSF-convolved IFU data (Conv) are made by the convolution of a wavelength-dependent PSF on the 2D image at each wavelength slice with the addition of Gaussian random noise. Deconv IFU data are produced from Conv IFU data by applying the deconvolution method.

An arbitrary synthetic spectrum, composed by single stellar populations with three different ages (1 Gyr (15%), 5 Gyr (60%), 10 Gyr (25%)) from the MILES stellar library (Sánchez-Blázquez et al. 2006; Vazdekis et al. 2010; Falcón-Barroso et al. 2011), is chosen as a rest-frame model spectrum (using unimodal initial mass function (Vazdekis et al. 1996) and Padova+00 isochrones (Girardi et al. 2000); $\Delta\lambda = 2.51$ Å, λ range from 3540 to 7410 Å).

For each set of galaxy model parameters (Section 3.2), we generate the Free and Conv mock IFU data, according to the following steps:

1. The spatial and spectral sampling size of the mock IFU data is determined. Following the sampling size and the data structure of MaNGA IFU data, we choose spatial sampling size as $0\farcs5$, and in the spectral direction we use a logarithmic wavelength sampling from $\log_{10}\lambda = 3.5589$ to 4.0151, with a total of 4563 wavelength bins.
2. 2D maps of flux (Sérsic profile), LOS velocity with respect to the galaxy center (Equation (2)), velocity dispersion (Equation (3)), and S/N distribution (set by S/N at 1 effective radius) are identified as per a set of galaxy model parameters. Angular size of R_e is determined by two parameters, IFU FOV and IFU radial coverage in R_e, by dividing half of the IFU FOV by the IFU radial coverage in R_e. We assume that all three maps follow the identical geometry as defined by the inclination angle, position angle, x_{cent}, and y_{cent}. In the case of the S/N map, a relative S/N map is generated as per the Sérsic profile and then scaled to have an S/N at 1 R_e as per the galaxy model parameter.
3. At each 2D pixel (spaxel), a rest-frame spectrum is shifted and broadened in the spectral direction as per the respective LOS velocity and the velocity dispersion value in the 2D map. First, the spectrum is convolved by a Gaussian function as per the velocity dispersion value. Second, the spectrum is redshifted by z of a model galaxy. Third, a spectrum at each spaxel is blue- or redshifted according to the corresponding LOS velocity value with respect to the galaxy center.
4. (Conv IFU data only) A 2D Gaussian PSF is convolved to the 2D image slice at each wavelength bin. The size of the Gaussian PSF FWHM is determined according to the model FWHM coefficient parameters. For example, in the case of $c_0 = 2\farcs6$ and $c_1 = -1.2 \times 10^{-5\farcs}$ Å^{-1}, $\mathrm{FWHM_{Conv}}$ at g-band effective wavelength (4770 Å) is $2\farcs52$ (which is the median g-band PSF FWHM size of the MaNGA galaxies; Figure 8).
5. A constant spectral resolution (2.9 Å) is applied at each spaxel as a proxy of instrument resolution of the real IFU data. It is done by the convolution of the Gaussian function (FWHM=1.45 Å) to each spectrum. The FWHM size of the applied Gaussian function is determined by the quadratic difference between the instrument spectral resolution and the intrinsic resolution of the model synthetic spectrum (2.51 Å).
6. The noise spectrum at each spaxel is calculated. First, a relative S/N spectrum is calculated from the flux spectrum (assuming Poisson noise), and the relative S/N spectrum is scaled so that the S/N value of the median flux value would be matched to the S/N value in the 2D S/N map (generated in step 2). The noise spectrum is calculated by dividing the flux spectrum by the scaled S/N spectrum. The noise spectrum is not added to the flux spectrum at this stage.
7. Hexagonal shape mask is applied to the IFU data to resemble the MaNGA-like IFU data.
8. (Conv IFU data only) Gaussian random noise is applied to the IFU data using the noise spectrum from step 6. At each spaxel, the noise spectrum is multiplied by the Gaussian random value (−3 to 3) and then added to the flux spectrum.
9. Generated mock spectra are saved in 3D cube FITS format. Each noise spectrum is converted to an inverse

variance spectrum ($=1/\text{noise}^2$) before being saved. Flux, inverse variance, mask, wavelength, and spectral resolution data are saved in FITS extension similar to the actual MaNGA IFU data.

Appendix B
Validity of Rotation Curve Model Fitting

In Section 3.3, we notice that there are cases where the RC model fitting could give an unreliable result under certain circumstances. One case is where the 2D velocity data do not have sufficient radial coverage to constrain the RC slope at the outer radius. For example, in Figure 1, the model would not be able to constrain the RC outer radius slope if the data cover only up to $r = 4''$. The other case is where the geometry of the fitted galaxy is close to either edge- or face-on. In this case, both fitted RC velocity amplitude ($V_{\rm ROT}$) and inclination angle (i) become unreliable. We investigate these two cases in detail using the Group 3 mock IFU data (Section 3.2), which represent various combinations of galaxy parameters that mimic the actual IFU data. From the result, we estimate the criterion that the result of RC model fitting can be considered as valid.

First, we calculate the R-ratio, a ratio between the maximum radial distance along the major axis and the R_1 parameter value ($=R_{\rm major,\ S/N>3}/R_1$). We define the maximum radial distance as the farthest radial distance among the radial distances of the spaxels that are located within $\pm5°$ from the major axis and satisfying $\rm S/N_{pPXF} > 3$. $\rm S/N_{pPXF}$ is the median S/N of the spectrum that is used for LOS velocity distribution fitting (pPXF routine). Then, we plot the relation between the R-ratio and the fitting accuracy of the normalized RC outer slope value as in Figure B1. Although there are multiple factors affecting R-ratio, including the size of IFU, S/N cut, and Sérsic index, we divide the result depending on its IFU size only because the size causes the most significant systematic difference to the 1σ variation of the normalized RC outer slope accuracy. In Figure B1, the accuracy of the normalized RC outer radius slope (R_1/R_2) shows strong dependence on the R-ratio. Regardless of the IFU size, the median difference between the true and the fitted R_1/R_2 is large at low R-ratio, and the difference becomes smaller at higher R-ratio, except for the 19 fiber size IFU, which is the smallest in its size. The 1σ variation of the R_1/R_2 difference becomes smaller as the mock IFU size increases, mainly because the larger IFU has more spaxels, so naturally it can better constrain the parameter values. We did not plot the 1σ range of the 19 fiber size IFU because the range is larger than the height of the plot. From the result, we set a criterion of R-ratio > 2.5, to determine whether the measured R_1/R_2 can be considered as valid, because the difference between the true and the fitted R_1/R_2 becomes stable and small at R-ratio >2.5 compared to the difference at R-ratio <2.5. We also find that the R_1/R_2 value measured from 19 fiber size IFU (FOV equal to $12''$) should not be used. This is because the measured R_1/R_2 value remains inaccurate even at R-ratio >2.5.

We also analyze the relation between the R-ratio and the fitting accuracy of the galaxy kinematic inclination angle in Figure B2. This result is plotted with the IFU data, which are satisfying a criterion of R-ratio > 2.5 only. The result shows that the fitted RC velocity amplitude ($V_{\rm ROT}$) is highly uncertain when the fitted inclination angle is low. In addition, 1σ of the median $V_{\rm ROT}$ also decreases when the fitted inclination value gets higher. Again, we notice that the result of 19 fiber size IFU is not reliable owing to its small number of spaxels. There is a slight hint that the fitted result may not be reliable at the higher inclination side, because the 1σ range is getting increased when the inclination angle is high. This can be explained by the low number of total spaxel elements when the inclination angle is high. From the shape of the curves and the 1σ range, we set a conservative criterion of $25° < \rm i^{deconv} < 75°$ and consider the fitted $V_{\rm ROT}$ value as valid when the result meets those criteria.

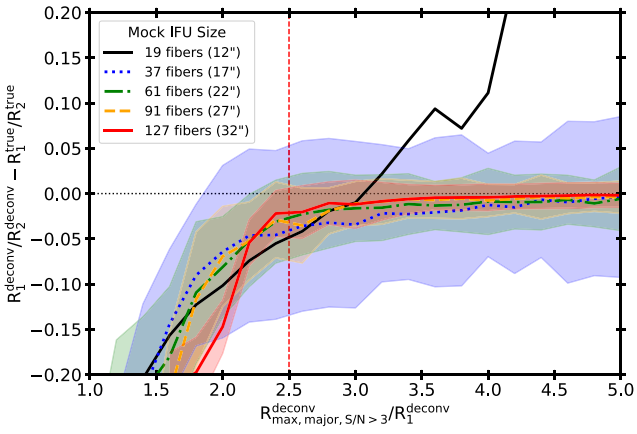

Figure B1. The difference between the true and fitted RC outer radius slope (R_1/R_2) from the deconvolved mock IFU cubes with respect to the R-ratio ($R_{\rm max,\ S/N>3,major}/R_1$). Color represents the size of mock IFU. Each line represents the median of the normalized RC outer radius slope differences at each bin. The shaded region shows the 1σ range of the differences. The 1σ range of the 19 fiber size IFU is not shown because it is significantly higher than others. The vertical red dashed line indicates our choice of R-ratio criterion, which is R-ratio >2.5.

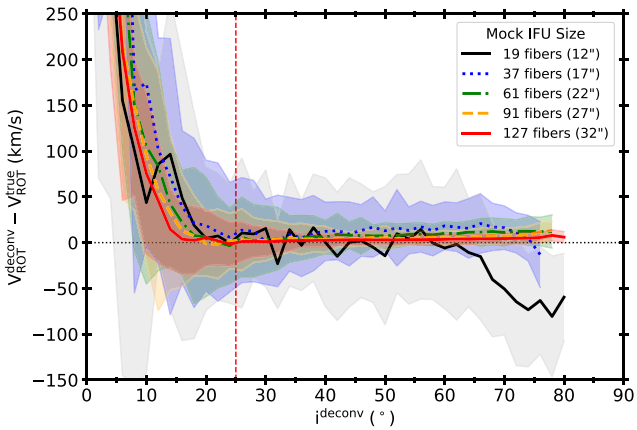

Figure B2. The difference between the true and fitted RC velocity amplitude ($V_{\rm ROT}$) from the deconvolved mock IFU cubes with respect to the fitted inclination angle. Color represents the size of mock IFU. The solid line represents the median of the RC velocity amplitude differences at each bin. The shaded region shows the 1σ range of the differences. The vertical red dashed line indicates the lower end of our inclination angle criterion choice ($25° < i^{\rm deconv} < 75°$).

Appendix C
Deconvolution Effect Examples

In Figure 2, we presented the example of the effects of PSF convolution and deconvolution on the IFU data. Here we show more examples from our mock IFU data to illustrate the effects of the deconvolution in various mock galaxy parameter spaces. Examples are taken from Group 1 mock IFU data. Figures C1 and C2 show the result of the deconvolution at low S/N (S/N@1 $R_e = 10$) when $n_{\rm Sérsic} = 1$ and 4, $R_1 = 3''$, and $i = 55°$. Figures C3–C6 show the result of the deconvolution at different combinations of i (55, 70°) and $n_{\rm Sérsic}$ (1, 4), when S/N at 1 $R_e = 20$ and $R_1 = 3''$. The fourth columns of the all figures represent the significant difference between the maps from Free and Conv. The effect of PSF convolution is crucial in the distribution of flux, velocity, and velocity dispersion. The fifth columns of all the figures show that the changes made by the PSF convolution are significantly restored by the deconvolution method. However, the restoration is not very effective at the outer radius, where S/N becomes low, and also the flux distribution shows nonnegligible artifacts around the center of galaxies, in particular when $n_{\rm Sérsic} = 4$. Nevertheless, the velocity and the velocity dispersion are generally well recovered even when $n_{\rm Sérsic} = 4$.

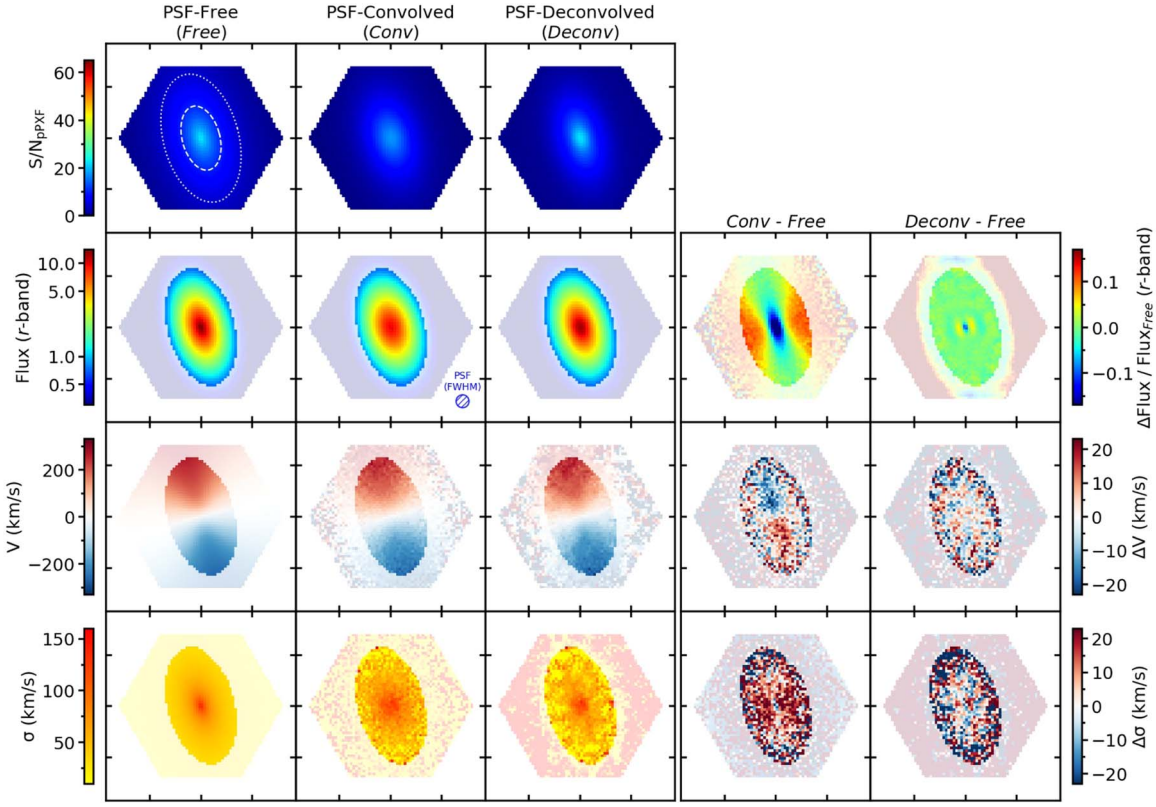

Figure C1. Plots similar to Figure 2, but for $n_{\rm Sérsic} = 1$, $R_1 = 3''$, $1/R_2 = 0.05$/arcsec, $i = 55°$, and S/N@1 $R_e = 10$.

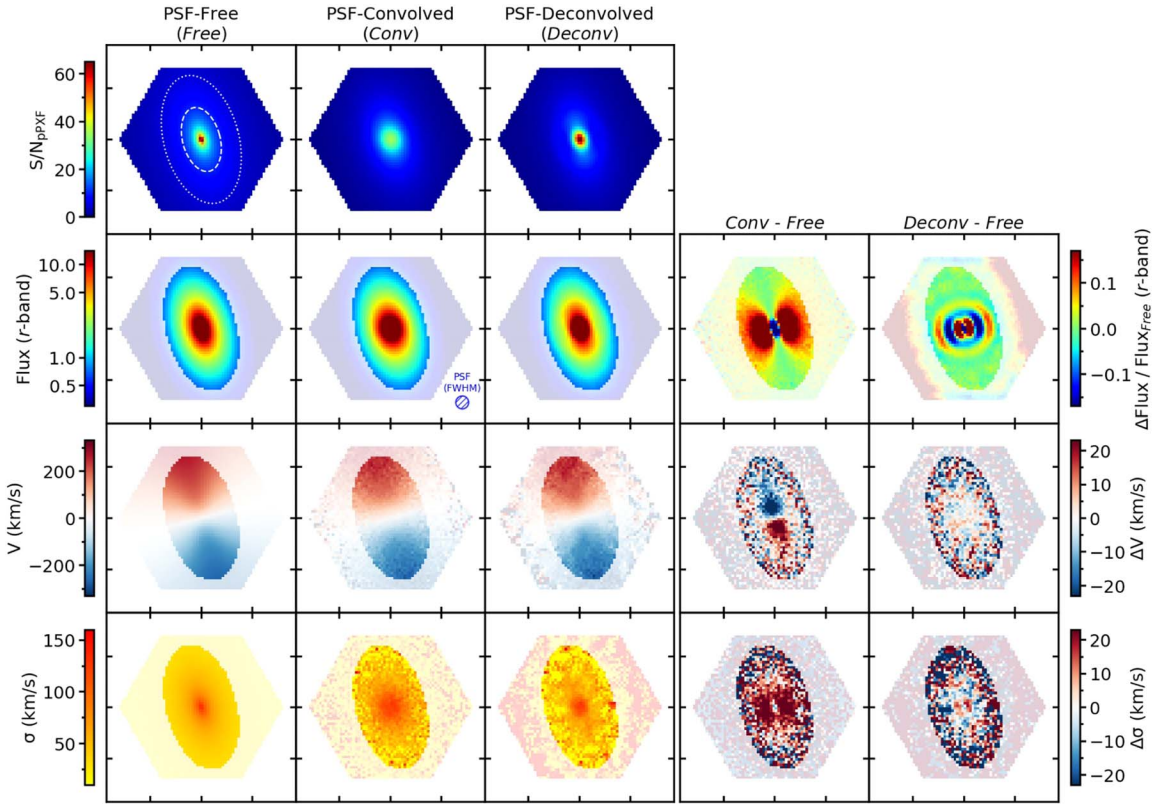

Figure C2. Plots similar to Figure 2, but for $n_{Sérsic} = 4$, $R_1 = 3''$, $1/R_2 = 0.05$/arcsec, $i = 55°$, and S/N@1 $R_e = 10$.

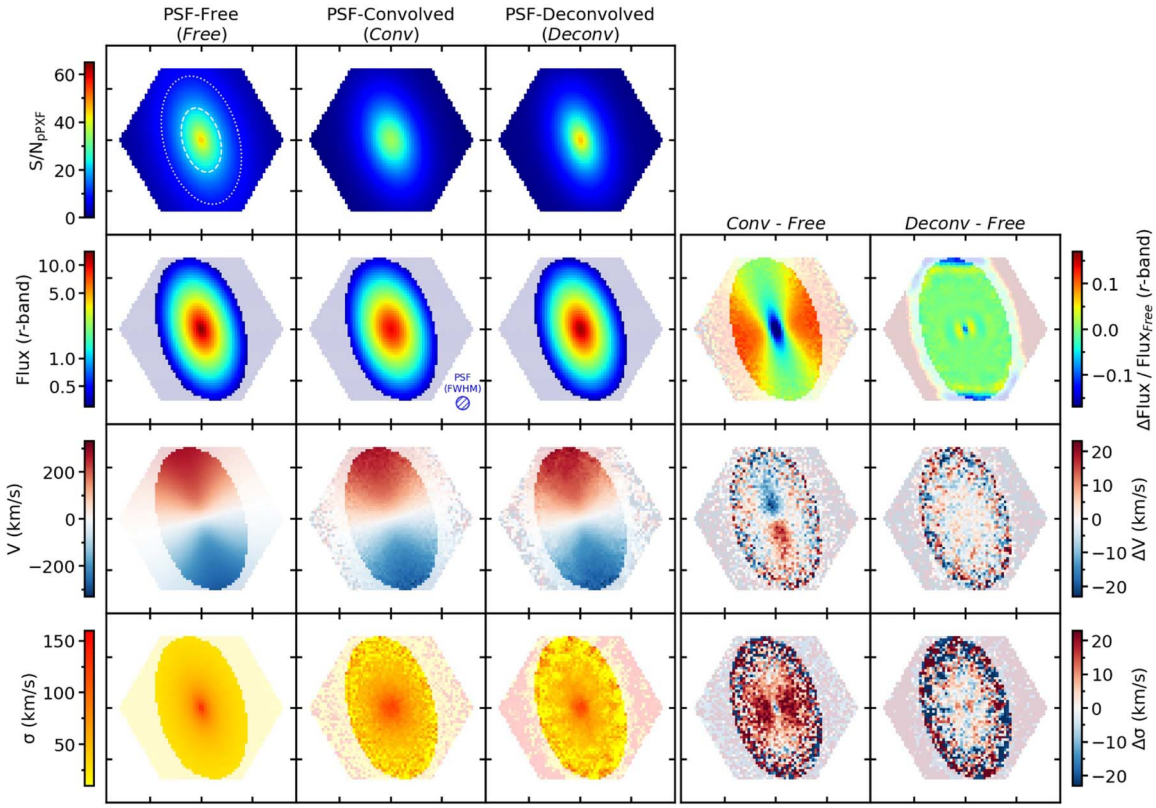

Figure C3. Plots similar to Figure 2, but for $n_{Sérsic} = 1$, $R_1 = 3''$, $1/R_2 = 0.05$/arcsec, $i = 55°$, and S/N@1 $R_e = 20$.

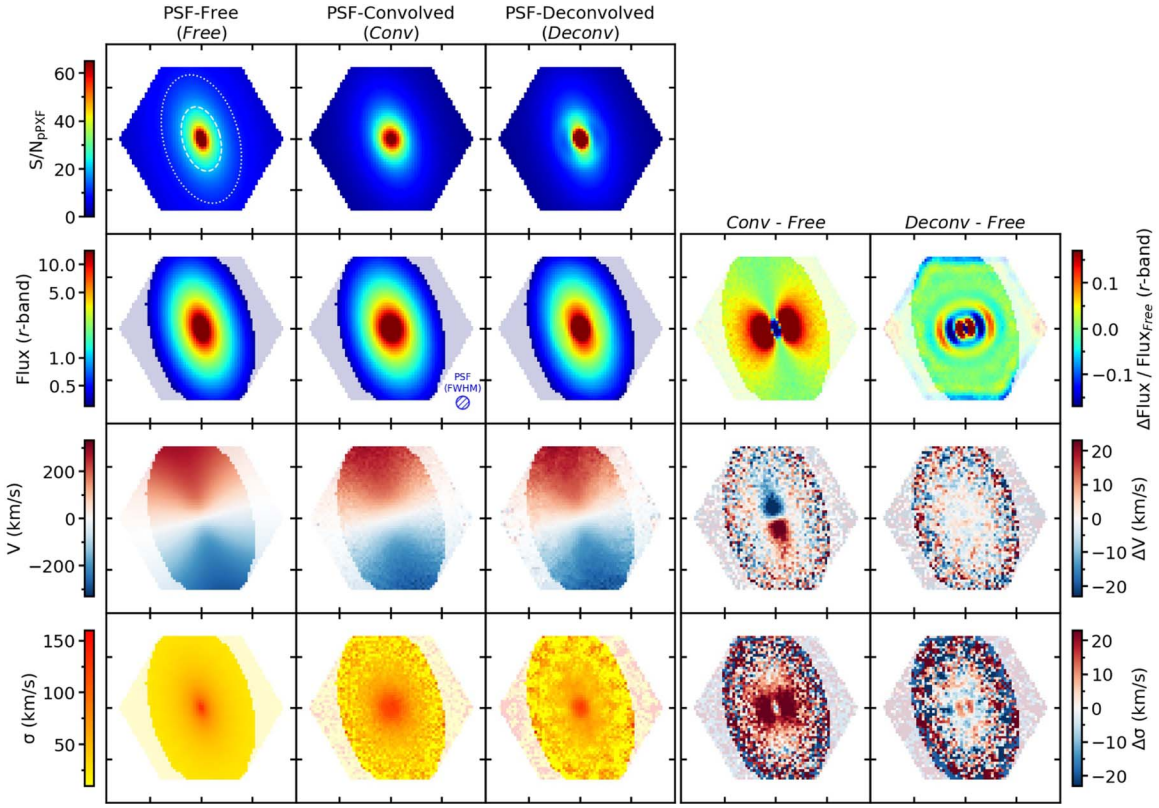

Figure C4. Plots similar to Figure 2, but for $n_{Sérsic} = 4$, $R_1 = 3''$, $1/R_2 = 0.05$/arcsec, $i = 55°$, and S/N@1 $R_e = 20$.

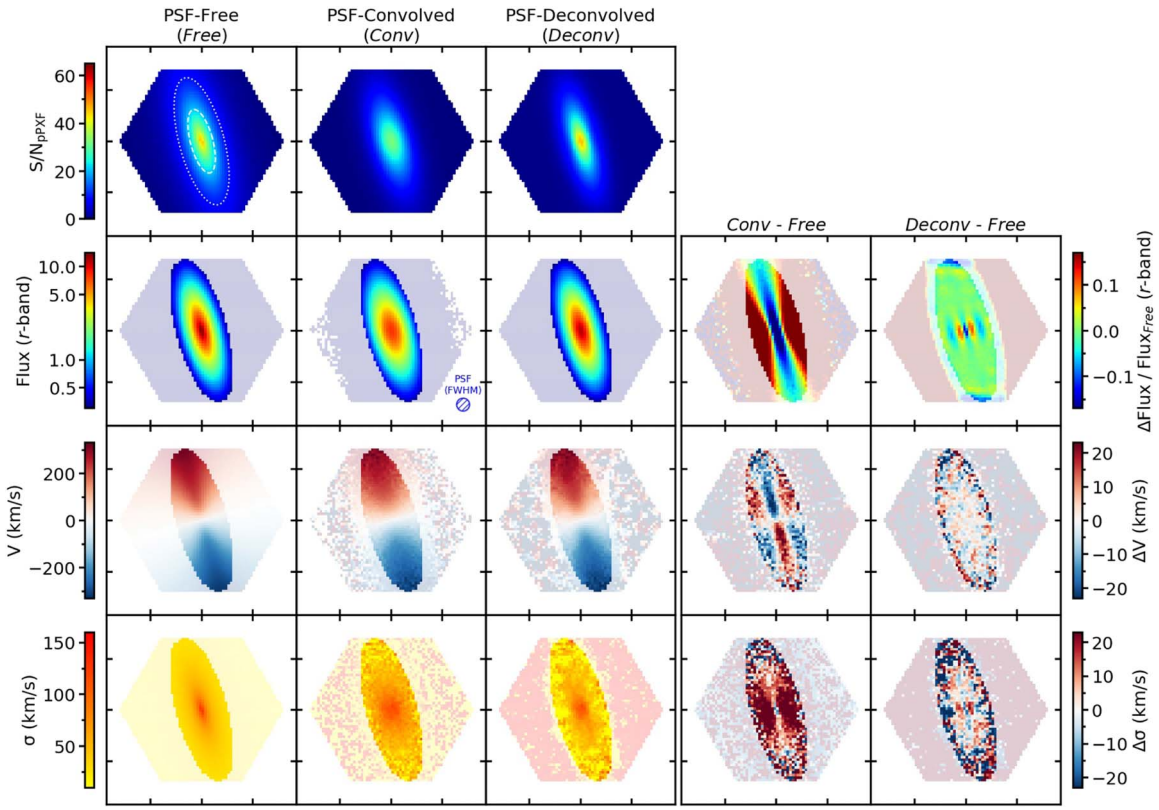

Figure C5. Plots similar to Figure 2, but for $n_{Sérsic} = 1$, $R_1 = 3''$, $1/R_2 = 0.05$/arcsec, $i = 70°$, and S/N@1 $R_e = 20$.

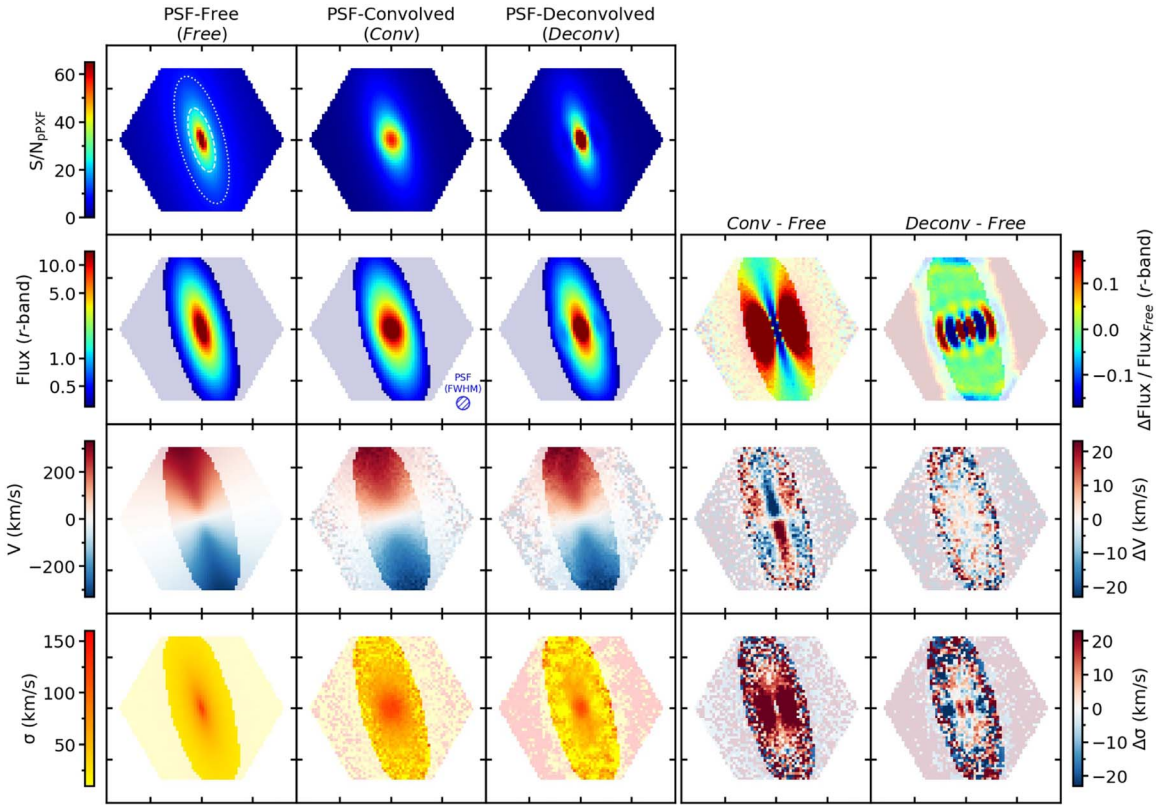

Figure C6. Plots similar to Figure 2, but for $n_{Sérsic} = 4$, $R_1 = 3''$, $1/R_2 = 0.05/\mathrm{arcsec}$, $i = 70°$, and S/N@1 $R_e = 20$.

Appendix D
Dependence on Deconvolution Parameters

D.1. Number of Deconvolution Iterations

In Section 3.4.2, we described the relationship between N_{iter} and the restored model kinematic parameters (Figure 4). Here we give similar plots with model galaxies of different parameters to provide more insight into the determination of N_{iter} to the readers. Figure D1 shows the effect of N_{iter} to the 2D maps of *r*-band flux, LOS velocity, and velocity dispersion. Figures D2–D5 are complementary figures to Figure 4. The figures show the relations between the fitted RC model parameter and the N_{iter} for different R_1 (2, 3, 4 (arcec)) and $1/R_2$ (-0.05, 0, 0.05 ($1/\mathrm{arcsec}$)). The result is consistent with Figure 4; thus, $N_{iter} = 20$ is an adequate choice for the deconvolution.

D.2. Size of PSF FWHM

Here we show the relation between $\mathrm{FWHM_{Deconv}}$ and the restored model kinematic parameters. We present plots similar to Figure 5 but with different model galaxies as well as different $\mathrm{FWHM_{Conv}}$.

Figures D6–D9 are complementary figures to Figure 5. The figures show the relation between the fitted RC model parameter and the $\mathrm{FWHM_{Deconv}}$ with different R_1 (2, 3, 4 (arcsec)) and $1/R_2$ (-0.05, 0, 0.05 ($1/\mathrm{arcsec}$)). The result is consistent with Figure 5; thus, the result of the deconvolution is consistent when $|\mathrm{FWHM_{Deconv}} - \mathrm{FWHM_{Conv}}|$ is smaller than the $\mathrm{FWHM_{PSF}}$ measurement error ($0\farcs2$).

Figures D10 and D11 show the result of the deconvolution with different $\mathrm{FWHM_{Conv}}$ (2.3, 2.9 (arcsec)). Again, the result of the deconvolution is consistent when $|\mathrm{FWHM_{Deconv}} - \mathrm{FWHM_{Conv}}|$ is small.

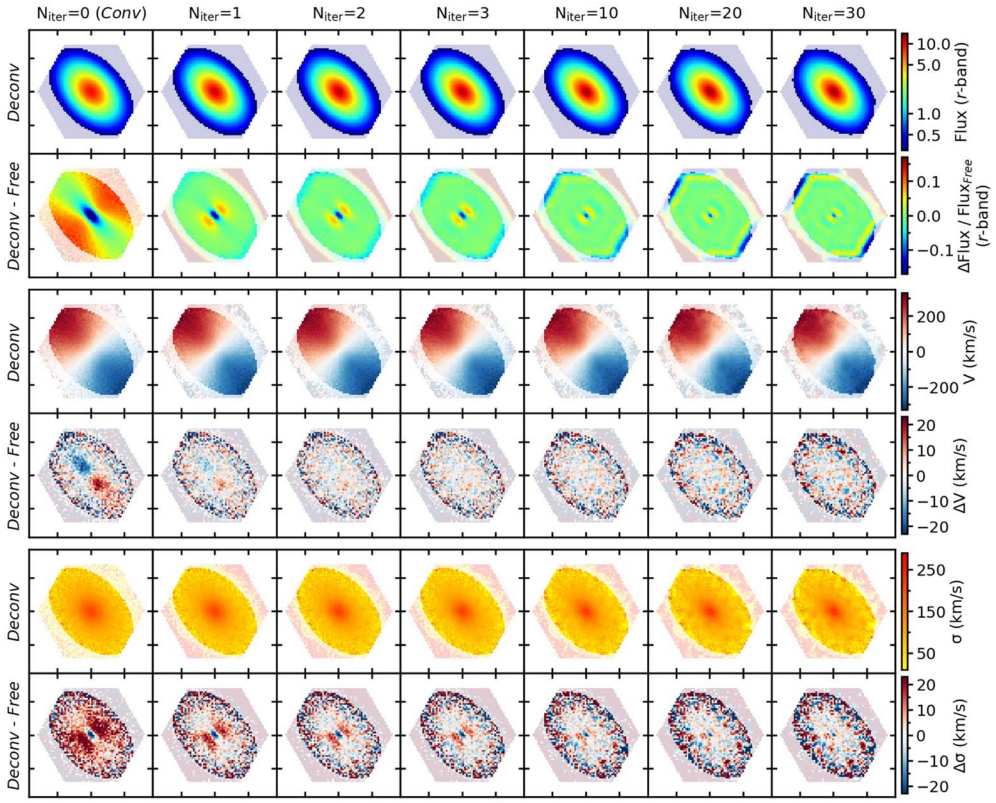

Figure D1. Effect of the number of deconvolution iterations ($N_{\rm iter}$) on the 2D maps of r-band flux, LOS velocity (V), and velocity dispersion (σ). The first and second rows show the 2D flux map from the deconvolved mock IFU data and the difference between the 2D flux map from the deconvolved mock IFU data and the PSF-free mock IFU data at selected $N_{\rm iter} = 0$, 1, 2, 3, 10, 20, 30, respectively. The third and fourth rows show the same for the 2D LOS velocity map, and the fifth and sixth rows show the same for the 2D velocity dispersion map. The 2D maps for $N_{\rm iter} = 0$ and $N_{\rm iter} = 20$ are the same as in Figure 2.

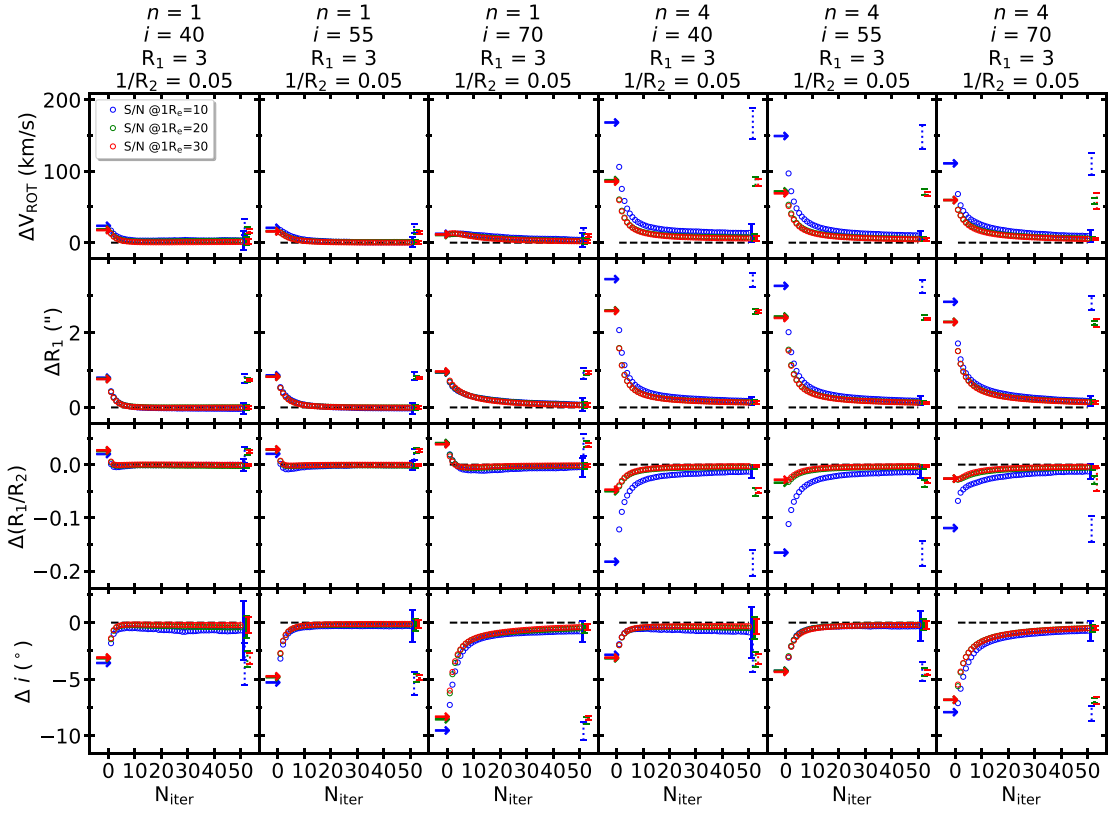

Figure D2. Relations between the RC model parameters and $N_{\rm iter}$ for $R_1 = 3$, $1/R_2 = -0.05$.

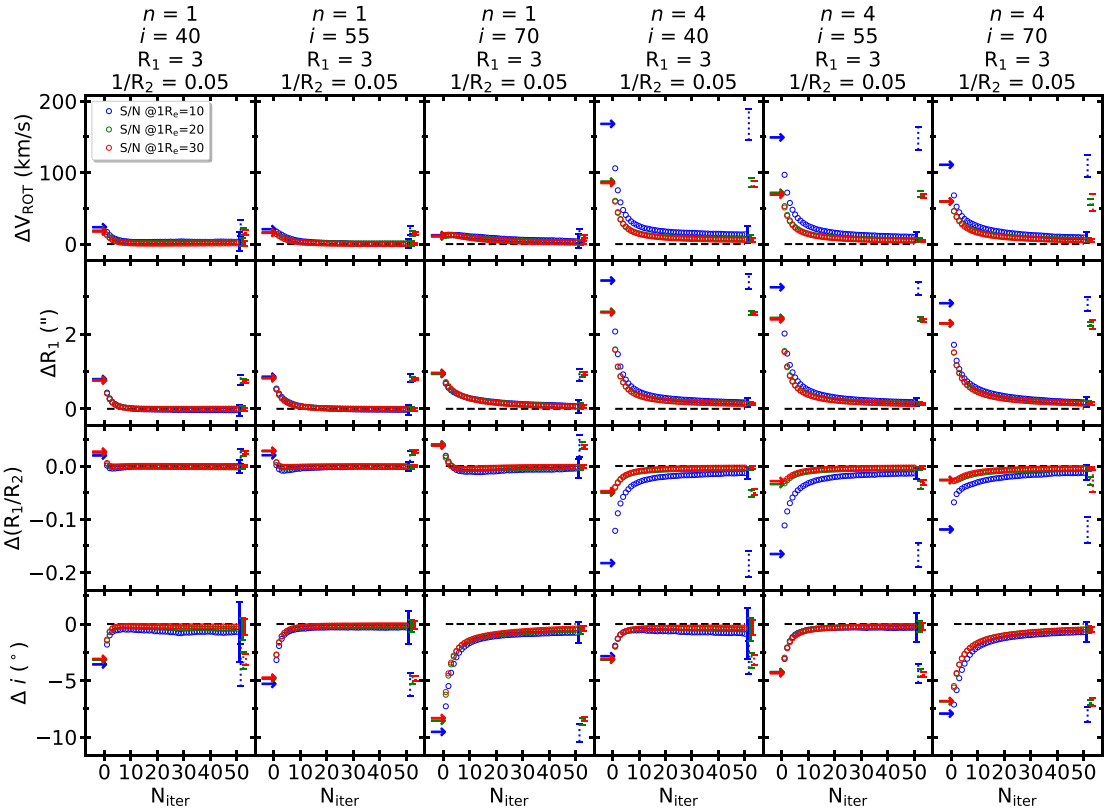

Figure D3. Plots similar to Figure D2, but for $R_1 = 3$, $1/R_2 = 0$.

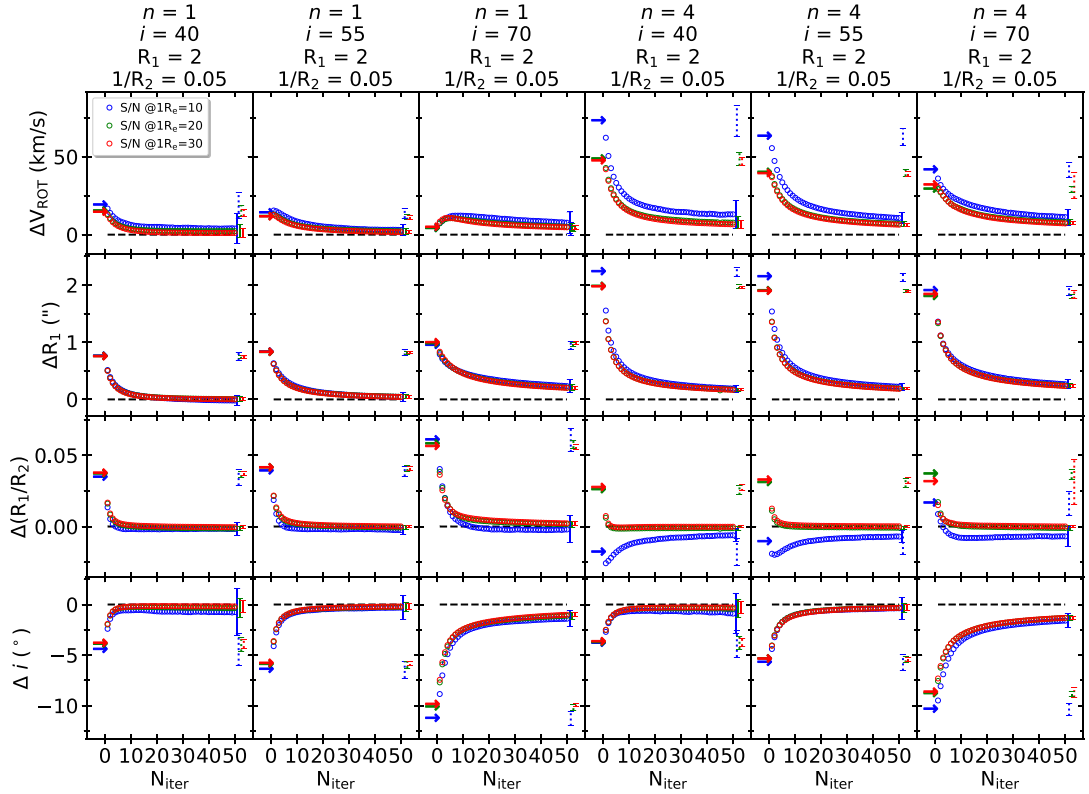

Figure D4. Plots similar to Figure D2, but for $R_1 = 2$, $1/R_2 = 0.05$.

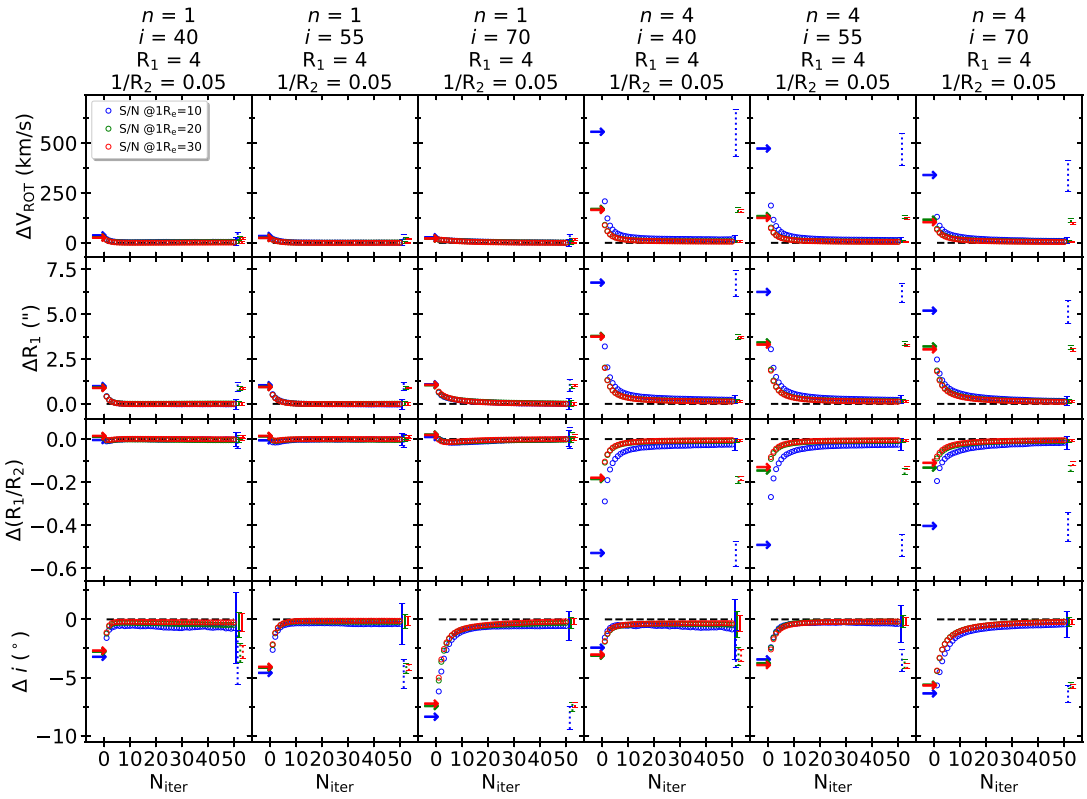

Figure D5. Plots similar to Figure D2, but for $R_1 = 4$, $1/R_2 = 0.05$.

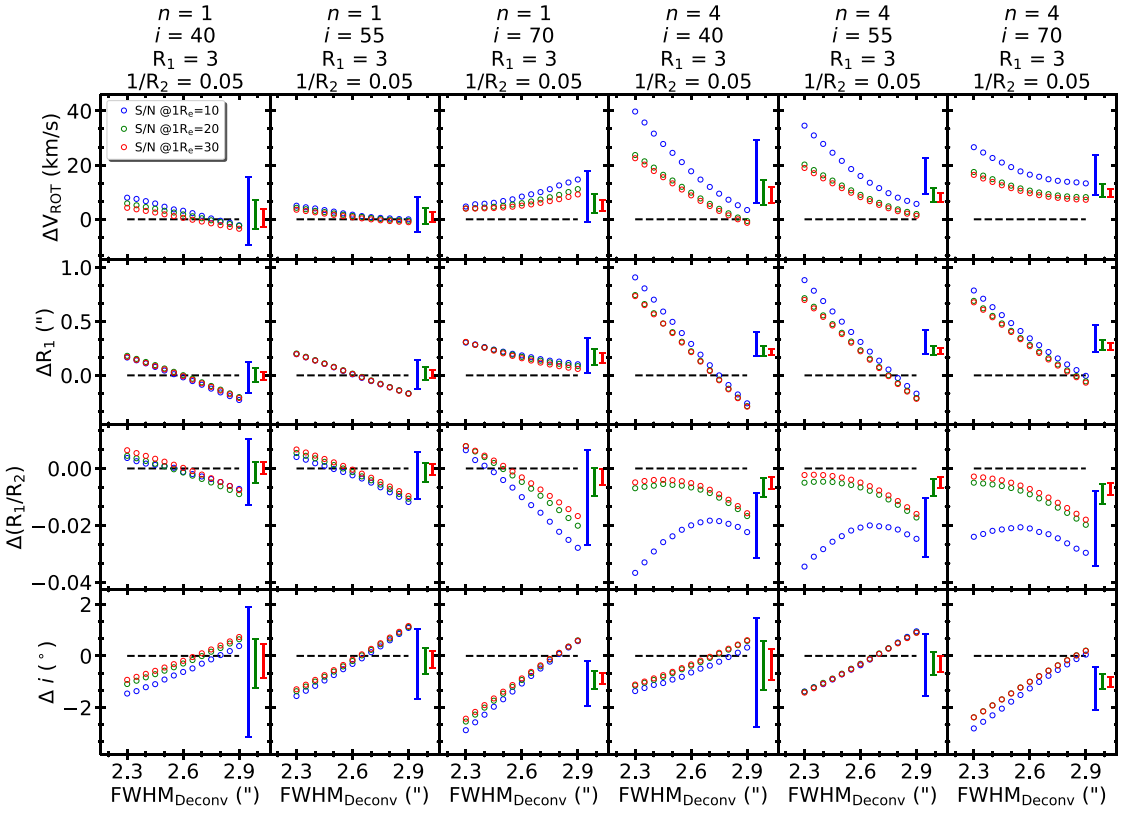

Figure D6. Relations between the RC model parameters and $\mathrm{FWHM}_{\mathrm{Deconv}}$ for $R_1 = 3$, $1/R_2 = -0.05$, $\mathrm{FWHM}c_0 = 2.6$.

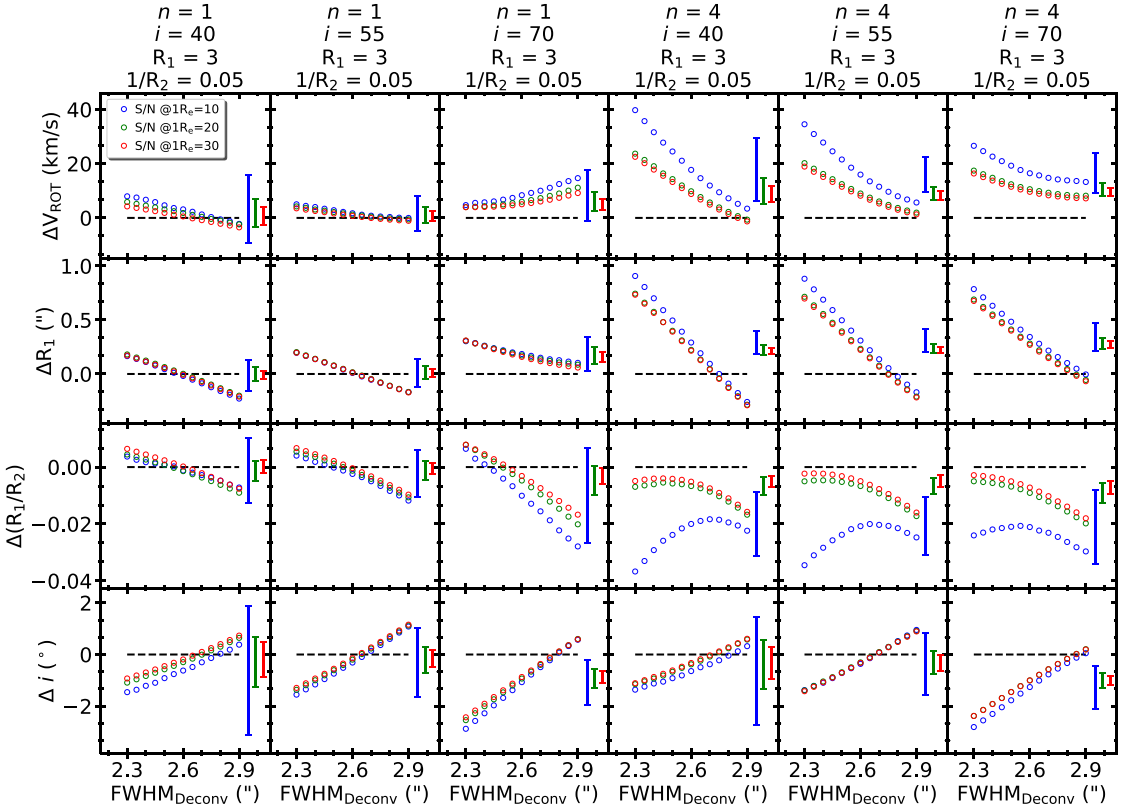

Figure D7. Plots similar to Figure D6, but for $R_1 = 3$, $1/R_2 = 0.05$, FWHM$c_0 = 2.6$.

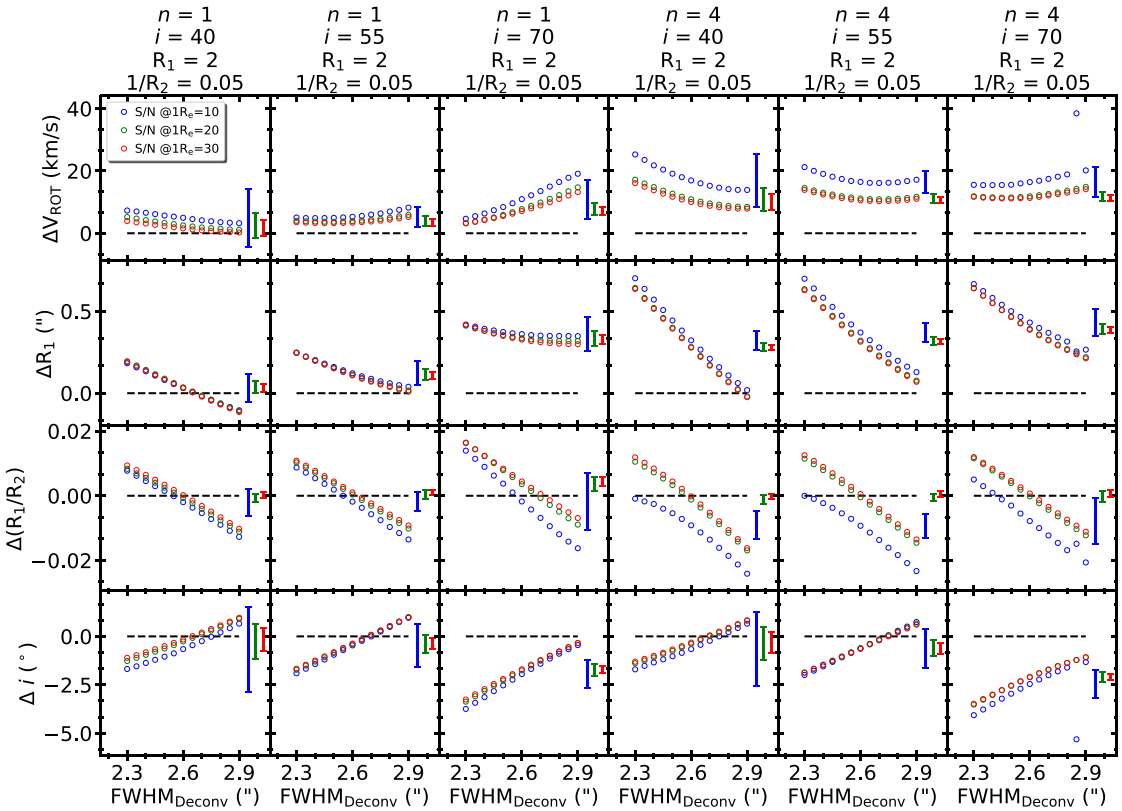

Figure D8. Plots similar to Figure D6, but for $R_1 = 2$, $1/R_2 = 0.05$, FWHM$c_0 = 2.6$.

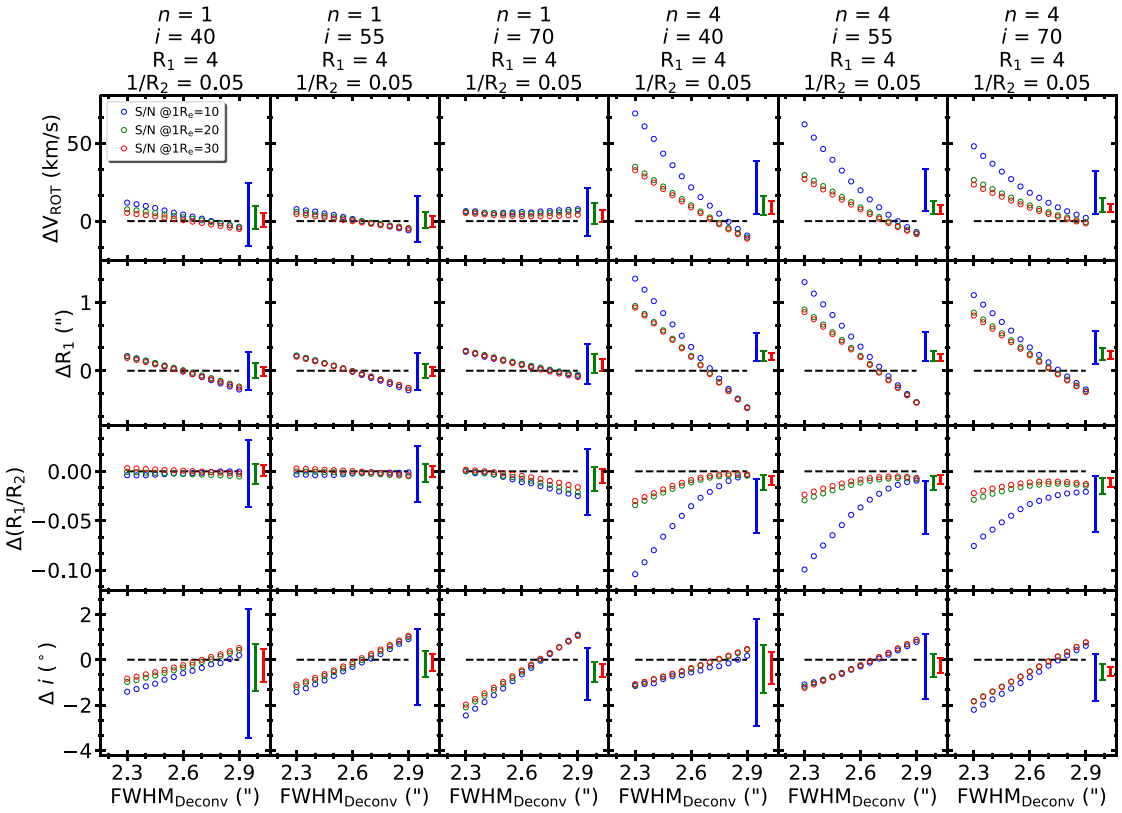

Figure D9. Plots similar to Figure D6, but for $R_1 = 4$, $1/R_2 = 0.05$, FWHM$c_0 = 2.6$.

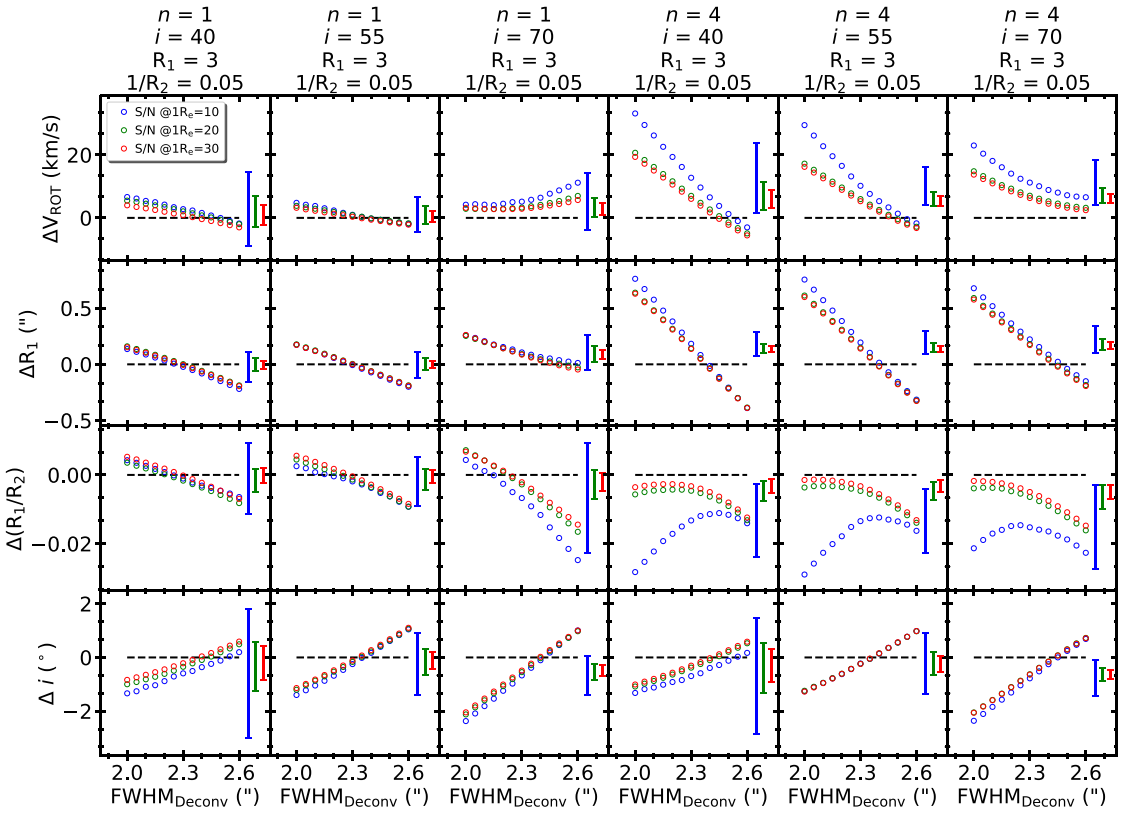

Figure D10. Plots similar to Figure D6, but for $R_1 = 3$, $1/R_2 = 0.05$, FWHM$c_0 = 2.3$.

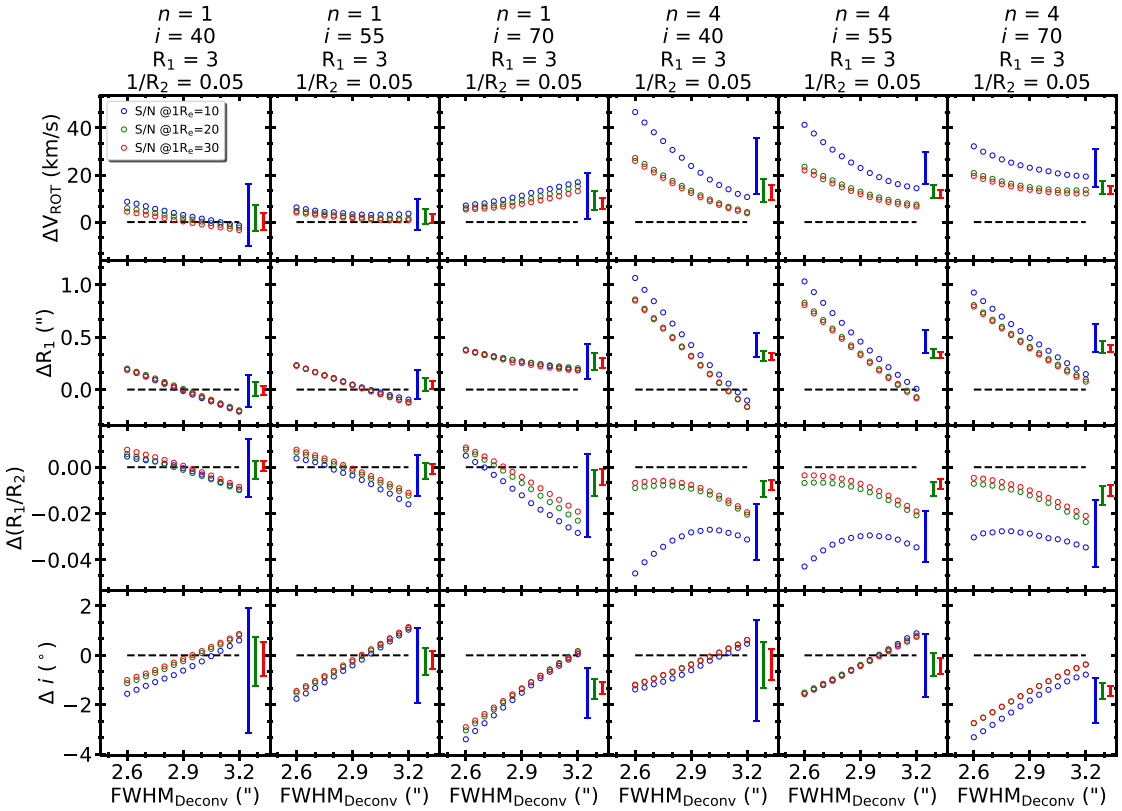

Figure D11. Plots similar to Figure D6, but for $R_1 = 3$, $1/R_2 = 0.05$, FWHM$c_0 = 2.9$.

Appendix E
Effect of PSF Convolution on the Spin Parameter Measurement

In Figure E1, we plot the relations between the λ_{R_e} ratios ($\lambda_{R_e}^{\rm Conv}/\lambda_{R_e}^{\rm Free}$, $\lambda_{R_e}^{\rm Deconv}/\lambda_{R_e}^{\rm Free}$, $\lambda_{R_e}^{\rm G18Corr.}/\lambda_{R_e}^{\rm Free}$) and the true λ_{R_e} value ($\lambda_{R_e}^{\rm Free}$), depending on three mock IFU parameters, IFU FOV, $n_{\rm Sérsic}$, and IFU radial coverage in $R_{\rm e}$, using Group 3 mock IFU data (Section 3.1). Most of the panels of Figure E1 show that λ_{R_e} ratios have little or negligible dependence on $\lambda_{R_e}^{\rm Free}$, except when $\lambda_{R_e}^{\rm Free} < 0.1$. The ratio and its standard deviation at $\lambda_{R_e}^{\rm Free} < 0.1$ look different compared to the ratios at $\lambda_{R_e}^{\rm Free} > 0.1$, but this is simply an effect of a small denominator when $\lambda_{R_e}^{\rm Free} < 0.1$. Since the denominator ($\lambda_{R_e}^{\rm Free}$) is already small, the actual deviation of λ_{R_e} values to the true value ($\lambda_{R_e} - \lambda_{R_e}^{\rm Free}$) is also small. The median and the median of standard deviation of each binned relation ($\Delta\lambda_{R_e}^{\rm Free} = 0.1$) are used to show the overall dependence of the ratios on the mock IFU parameters as in Figure 11. Unlike the average value of entire points, use of the median of the binned relations could avoid the contribution from the large difference and the standard deviation from the points at $\lambda_{R_e}^{\rm Free} < 0.1$. In Figure E2 we plot the relation between the λ_{R_e} ratios and the true λ_{R_e} value, depending on $n_{\rm Sérsic}$ and σ' parameters using the additional set of mock IFU data (Section 5.1). Again the median and the median of standard deviation of each binned relation ($\Delta\lambda_{R_e}^{\rm Free} = 0.1$) are used to show the overall dependence of the ratios on the mock IFU parameters as in Figure 12. Figure E3 shows the effect of the deconvolution to the 2D velocity and velocity distribution of the selected seven MaNGA galaxies, by applying additional PSF convolution to the MaNGA data. Figure E4 is similar to Figure 15, but for the case where the FWHM$_{\rm PSF}$ value is different from the true value by $\pm 0.''3$.

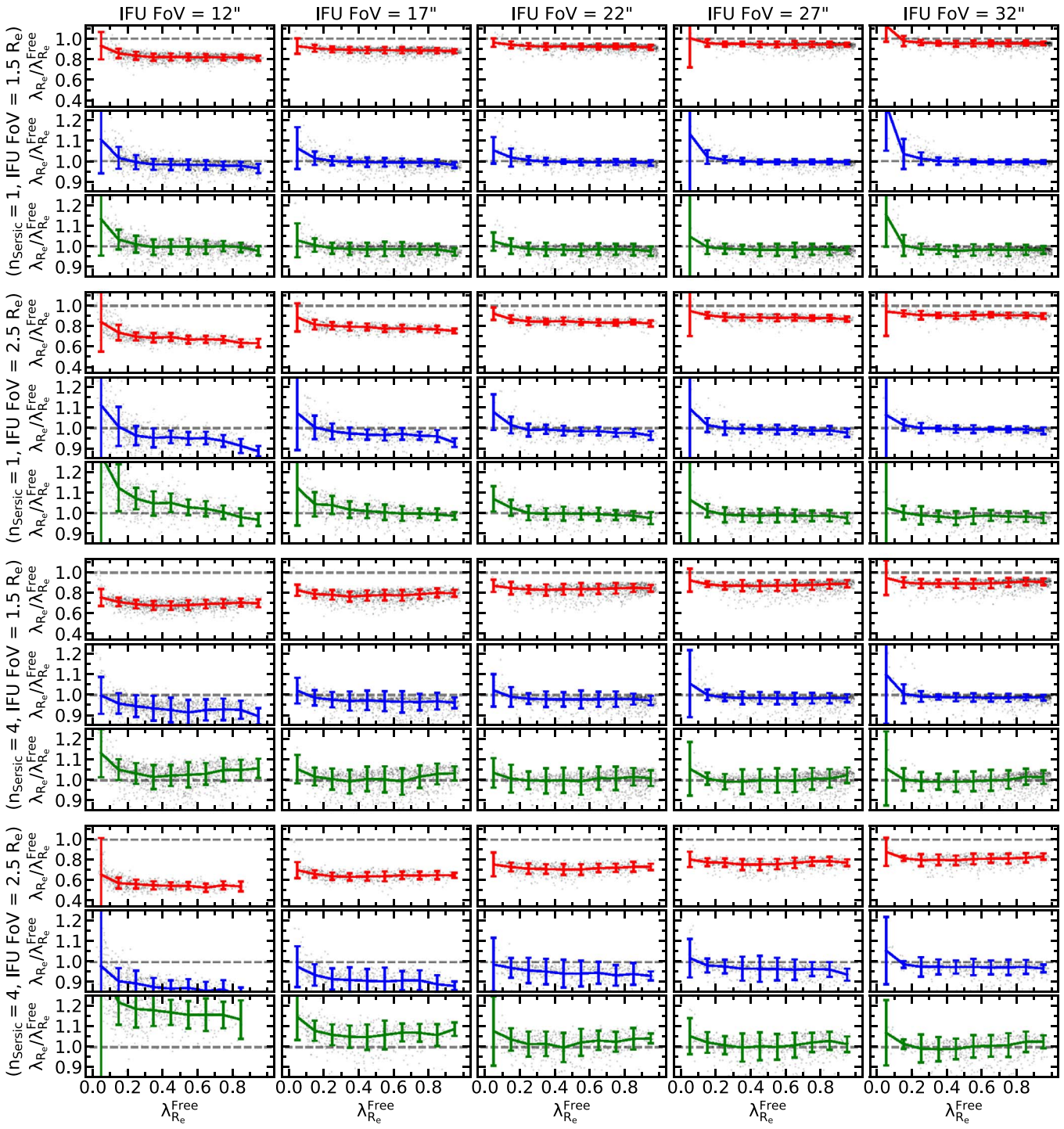

Figure E1. Relations between the ratio of λ_{R_e} values ($\lambda_{R_e}^{\rm Conv}$, $\lambda_{R_e}^{\rm Deconv}$, $\lambda_{R_e}^{\rm G18Corr.}$) and the true λ_{R_e} value ($\lambda_{R_e}^{\rm Free}$) as a function of $\lambda_{R_e}^{\rm Free}$. Each panel with red, blue, and green lines represents data points with $\lambda_{R_e}^{\rm Conv}/\lambda_{R_e}^{\rm Free}$, $\lambda_{R_e}^{\rm Deconv}/\lambda_{R_e}^{\rm Free}$, and $\lambda_{R_e}^{\rm G18Corr.}/\lambda_{R_e}^{\rm Free}$, respectively. Each column represents the FOV of mock IFU data used for each panel (IFU FOV = 12″, 17″, 22″, 27″, 32″). Each of continuous three rows represents the different combination of $n_{\rm Sérsic}$ and the IFU radial coverage in $R_{\rm e}$ ($n_{\rm Sérsic} = 1$ and radial coverage of 1.5 $R_{\rm e}$, $n_{\rm Sérsic} = 1$ and radial coverage of 2.5 $R_{\rm e}$, $n_{\rm Sérsic} = 4$ and radial coverage of 1.5 $R_{\rm e}$, $n_{\rm Sérsic} = 4$ and radial coverage of 2.5 $R_{\rm e}$). Data points are plotted as gray dots in the background. Colored lines and the corresponding error bars are the median and the standard deviation of the data points from each bin with the bin size of $\Delta\lambda_{R_e}^{\rm Free} = 0.1$.

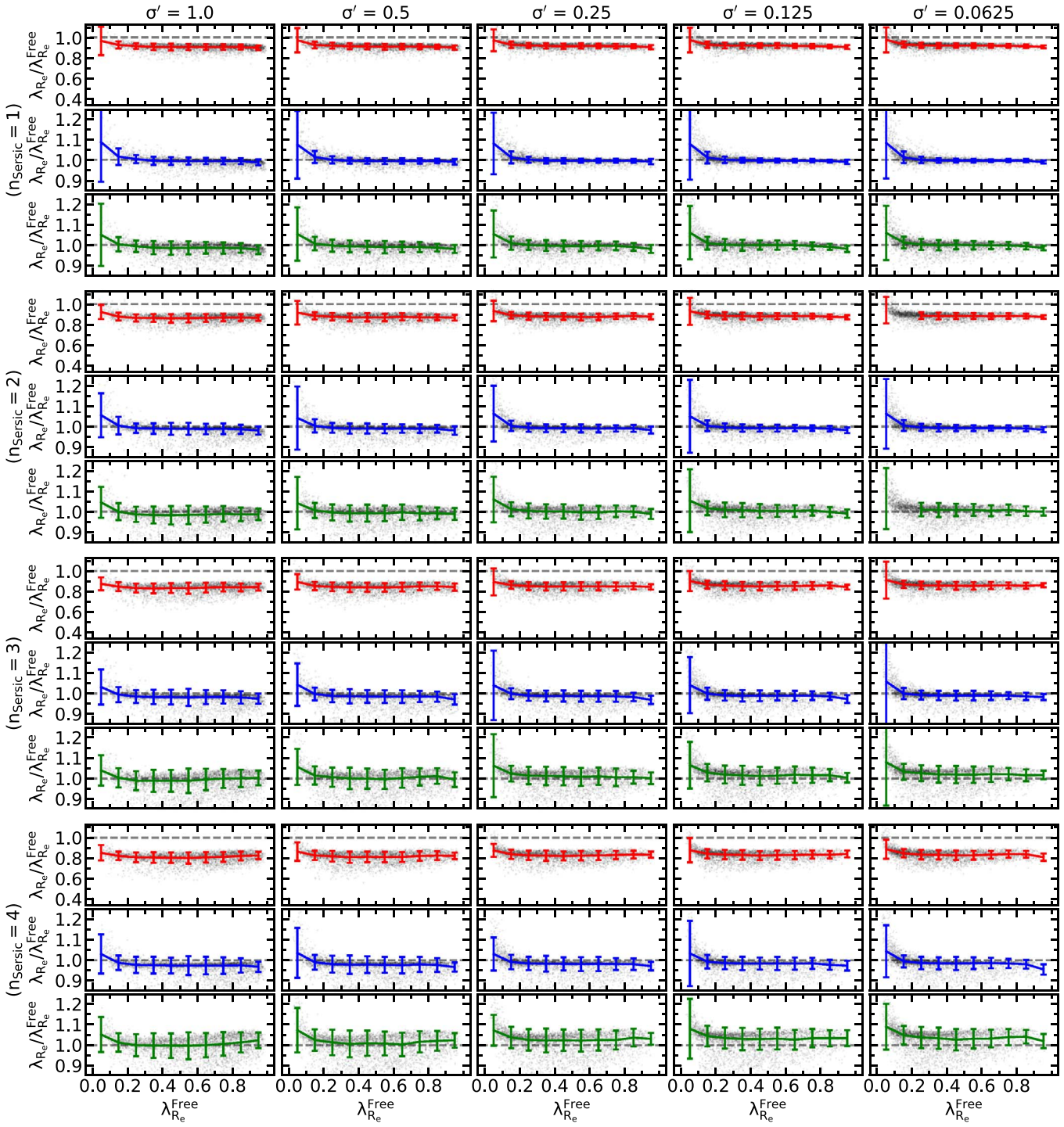

Figure E2. Relations between the ratio of λ_{R_e} values ($\lambda_{R_e}^{\rm Conv}$, $\lambda_{R_e}^{\rm Deconv}$, $\lambda_{R_e}^{\rm G18Corr.}$) and the true λ_{R_e} value ($\lambda_{R_e}^{\rm Free}$) as a function of $\lambda_{R_e}^{\rm Free}$, similar to Figure E1 but using a different set of mock IFU data (Section 5.1). Each column represents different velocity dispersion profile steepness of the mock IFU data used for each panel ($\sigma' = 1$, 0.5, 0.25, 0.125, 0.0625). Each of continuous three rows represents different $n_{\rm Sérsic}$ of the mock IFU data ($n_{\rm Sérsic} = 1$, 2, 3, 4). Data points, colored lines, and the corresponding error bars are plotted in the same way as Figure E1.

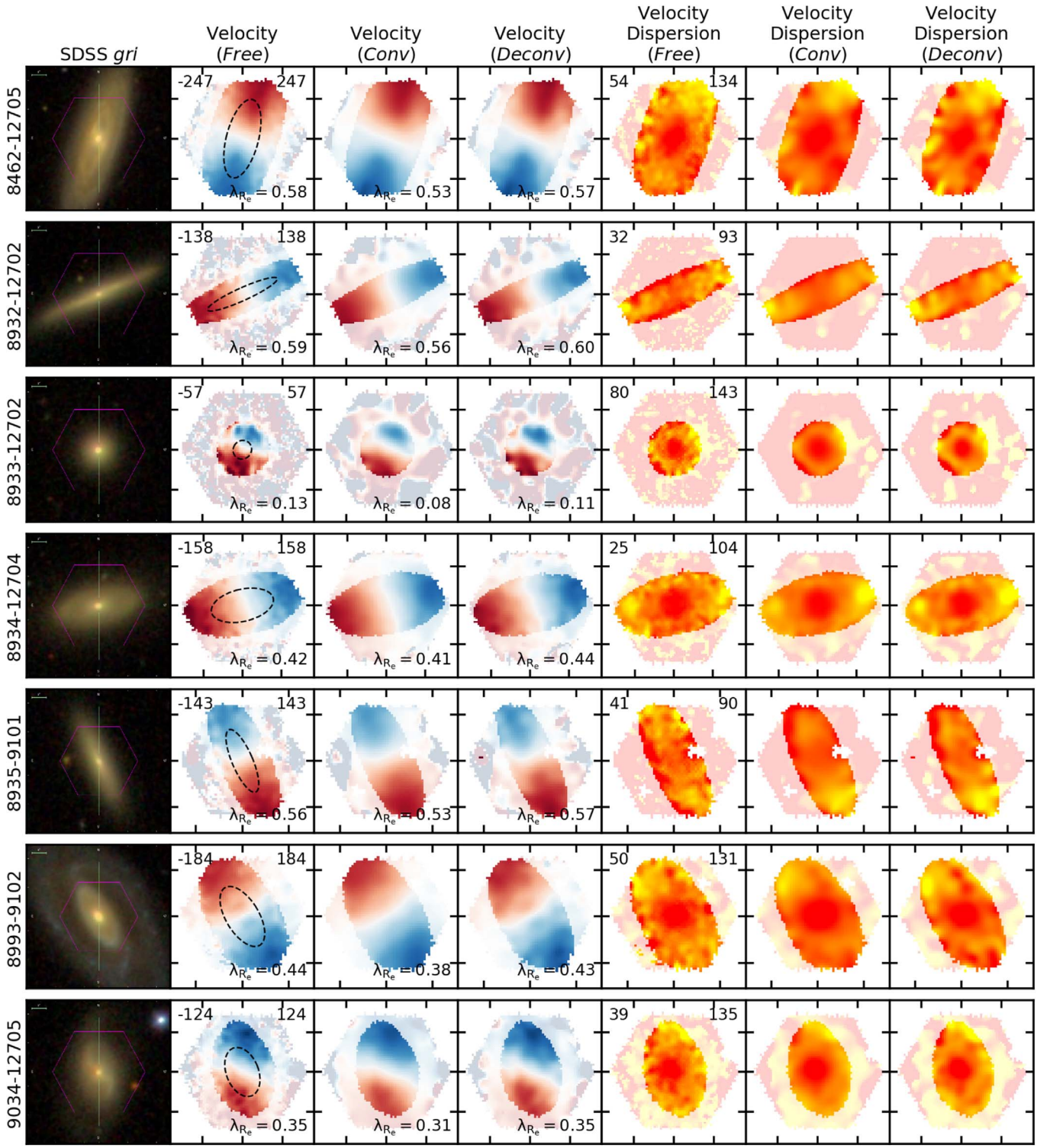

Figure E3. The velocity and velocity distribution of selected nearby MaNGA galaxies ($z < 0.023$ and IFU FOV $\geqslant 27''$). Distributions in the Free column are velocity and velocity dispersion distribution measured from the original MaNGA IFU data. Distributions in the other columns (Conv and Deconv) are measured from PSF-convolved and PSF-deconvolved (PSF FWHM $= 2.''6$) to the original MaNGA IFU data. The ellipses (black dashed) in the leftmost column show 1 R_e aperture, where the λ_{R_e} values are measured. The values in the top left and top right at each panel in the second and fifth columns indicate the minimum and the maximum range of color, where the color bars are the same as in Figure 2 (blue to red for the velocity distribution and yellow to red for the velocity dispersion distribution). Each major tick interval corresponds to $10''$.

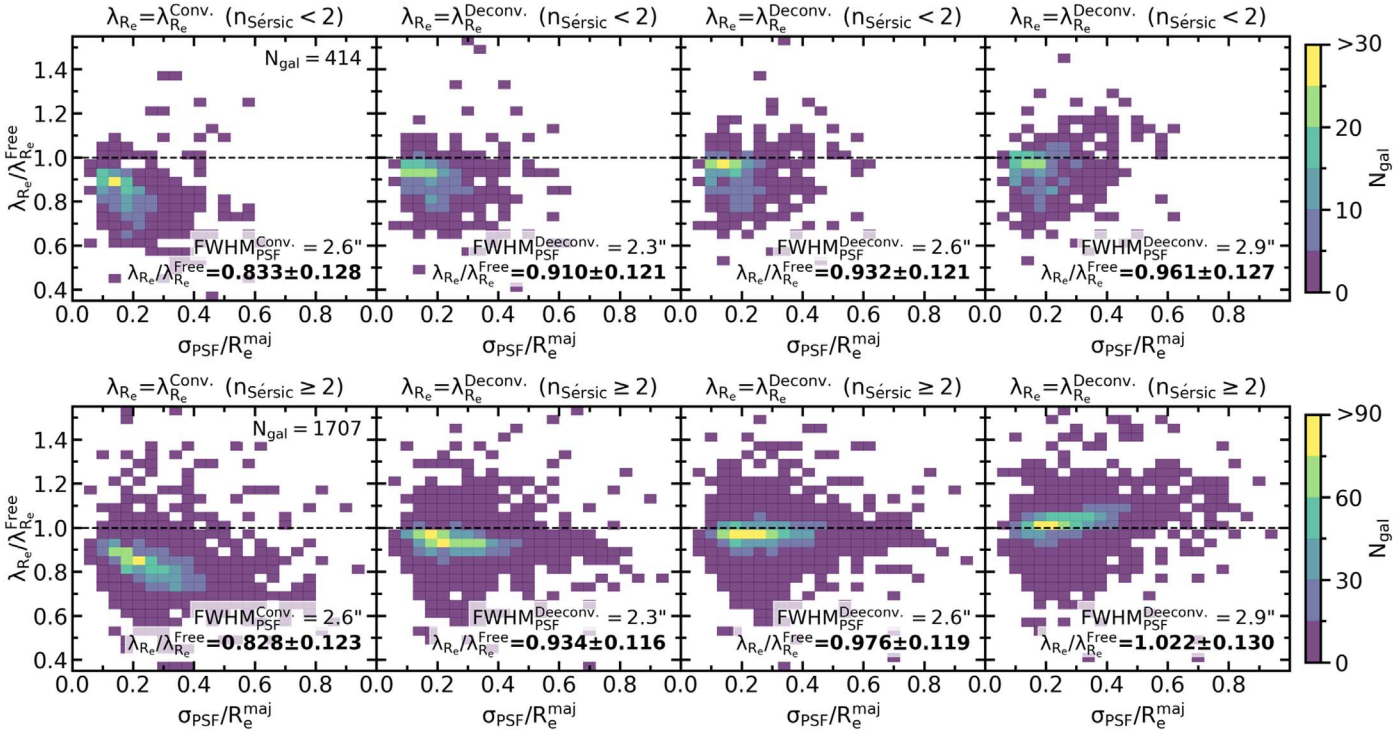

Figure E4. Comparison between the λ_{R_e} measured from PSF-Convolved and PSF-Deconvolved IFU data using MaNGA DR15 galaxies as the PSF-Free data, when the $FWHM_{PSF}$ used for the deconvolution or λ_{R_e} correction is different from the $FWHM_{PSF}$ of the convolved PSF. Upper and lower rows show the results when $n_{Sérsic} < 2$ and $n_{Sérsic} \geqslant 2$, respectively. The first column shows $\lambda_{R_e}^{Conv}/\lambda_{R_e}^{Free}$ as a function of $\sigma_{PSF}/R_e^{maj.}$. The second, third, and fourth columns show $\lambda_{R_e}^{Deconv}/\lambda_{R_e}^{Free}$ as a function of $\sigma_{PSF}/R_e^{maj.}$, but when $FWHM_{PSF}$ used for the deconvolution or λ_{R_e} correction is $2\overset{''}{.}3$, $2\overset{''}{.}6$, and $2\overset{''}{.}9$, respectively. The median and standard deviation of $\Delta\lambda_{R_e}$ are noted in each panel.

ORCID iDs

Haeun Chung https://orcid.org/0000-0002-3043-2555
Changbom Park https://orcid.org/0000-0001-9521-6397

References

Aguado, D. S., Ahumada, R., Almeida, A., et al. 2019, ApJS, 240, 23
Allington-Smith, J., Murray, G., Content, R., et al. 2002, PASP, 114, 892
Andersen, D. R., & Bershady, M. A. 2013, ApJ, 768, 41
Bacon, R., Accardo, M., Adjali, L., et al. 2010, Proc. SPIE, 7735, 773508
Bacon, R., Copin, Y., Monnet, G., et al. 2001, MNRAS, 326, 23
Bershady, M. A., Verheijen, M. A. W., Swaters, R. A., et al. 2010, ApJ, 716, 198
Bongard, S., Soulez, F., Thiébaut, É., & Pecontal, É. 2011, MNRAS, 418, 258
Bouché, N., Carfantan, H., Schroetter, I., Michel-Dansac, L., & Contini, T. 2015, AJ, 150, 92
Bourguignon, S., Carfantan, H., Slezak, E., & Mary, D. 2011, in 2011 3rd Workshop on Hyperspectral Image and Signal Processing: Evolution in Remote Sensing (WHISPERS) (Piscataway, NJ: IEEE)
Bundy, K., Bershady, M. A., Law, D. R., et al. 2015, ApJ, 798, 7
Cappellari, M. 2002, MNRAS, 333, 400
Cappellari, M. 2008, MNRAS, 390, 71
Cappellari, M. 2016, ARA&A, 54, 597
Cappellari, M. 2017, MNRAS, 466, 798
Cappellari, M., & Emsellem, E. 2004, PASP, 116, 138
Cappellari, M., Scott, N., Alatalo, K., et al. 2013, MNRAS, 432, 1709
Choi, H., & Yi, S. K. 2017, ApJ, 837, 68
Choi, H., Yi, S. K., Dubois, Y., et al. 2018, ApJ, 856, 114
Chung, H. 2021, First release of IFU data deconvolution code, v1.0.0, Zenodo, doi:10.5281/zenodo.4783185
Cooley, J. W., & Tukey, J. W. 1965, MaCom, 19, 297
Cortese, L., Fogarty, L. M. R., Bekki, K., et al. 2016, MNRAS, 463, 170
Courbin, F., Magain, P., Kirkove, M., & Sohy, S. 2000, ApJ, 529, 1136
D'Eugenio, F., Houghton, R. C. W., Davies, R. L., & Dalla Bontà, E. 2013, MNRAS, 429, 1258
Dressler, A., Bigelow, B., Hare, T., et al. 2011, PASP, 123, 288
Emsellem, E., Cappellari, M., Krajnović, D., et al. 2007, MNRAS, 379, 401
Emsellem, E., Cappellari, M., Krajnović, D., et al. 2011, MNRAS, 414, 888
Emsellem, E., Monnet, G., & Bacon, R. 1994, A&A, 285, 723
Falcón-Barroso, J., Sánchez-Blázquez, P., Vazdekis, A., et al. 2011, A&A, 532, A95
Feng, J. Q., & Gallo, C. F. 2011, RAA, 11, 1429
Girardi, L., Bressan, A., Bertelli, G., & Chiosi, C. 2000, A&AS, 141, 371
Graham, M. T., Cappellari, M., Li, H., et al. 2018, MNRAS, 477, 4711
Greene, J. E., Leauthaud, A., Emsellem, E., et al. 2018, ApJ, 852, 36
Harborne, K. E., van de Sande, J., Cortese, L., et al. 2020, MNRAS, 497, 2018
Henault, F., Bacon, R., Bonneville, C., et al. 2003, Proc. SPIE, 4841, 1096
Hopkins, P. F., Bundy, K., Hernquist, L., Wuyts, S., & Cox, T. J. 2010, MNRAS, 401, 1099
Jesseit, R., Cappellari, M., Naab, T., Emsellem, E., & Burkert, A. 2009, MNRAS, 397, 1202
Kelz, A., Verheijen, M. A. W., Roth, M. M., et al. 2006, PASP, 118, 129
Lagos, C. d. P., Theuns, T., Stevens, A. R. H., et al. 2017, MNRAS, 464, 3850
Law, D. R., Cherinka, B., Yan, R., et al. 2016, AJ, 152, 83
Law, D. R., Yan, R., Bershady, M. A., et al. 2015, AJ, 150, 19
Le Fèvre, O., Vettolani, G., Garilli, B., et al. 2005, A&A, 439, 845
Lee, J. C., Hwang, H. S., & Chung, H. 2018, MNRAS, 477, 1567
Lucy, L. B. 1974, AJ, 79, 745
Lucy, L. B., & Walsh, J. R. 2003, AJ, 125, 2266
Magain, P., Courbin, F., & Sohy, S. 1998, ApJ, 494, 472
Martin, G., Kaviraj, S., Devriendt, J. E. G., Dubois, Y., & Pichon, C. 2018, MNRAS, 480, 2266
Naab, T., Oser, L., Emsellem, E., et al. 2014, MNRAS, 444, 3357
Penoyre, Z., Moster, B. P., Sijacki, D., & Genel, S. 2017, MNRAS, 468, 3883
Press, W. H., Teukolsky, S. A., Vetterling, W. T., & Flannery, B. P. 2007, Numerical Recipes, The Art of Scientific Computing (3rd ed.; Cambridge: Cambridge Univ. Press)
Puech, M., Flores, H., Hammer, F., et al. 2008, A&A, 484, 173
Richardson, W. H. 1972, JOSA, 62, 55
Rodet, T., Orieux, F., Giovannelli, J.-F., & Abergel, A. 2008, ISTSP, 2, 802
Sánchez, S. F., García-Benito, R., Zibetti, S., et al. 2016, A&A, 594, A36

Sánchez-Blázquez, P., Peletier, R. F., Jiménez-Vicente, J., et al. 2006, MNRAS, 371, 703
Scott, N., van de Sande, J., Croom, S. M., et al. 2018, MNRAS, 481, 2299
Sharples, R., Bender, R., Agudo Berbel, A., et al. 2013, Msngr, 151, 21
Shepp, L. A., & Vardi, Y. 1982, IEEE Trans. Med. Imaging, 1, 113
Soulez, F., Bongard, S., Thiebaut, E., & Bacon, R. 2011, in 2011 3rd Workshop on Hyperspectral Image and Signal Processing: Evolution in Remote Sensing (WHISPERS) (Piscataway, NJ: IEEE)
van de Sande, J., Bland-Hawthorn, J., Fogarty, L. M. R., et al. 2017, ApJ, 835, 104
van de Sande, J., Lagos, C. D. P., Welker, C., et al. 2019, MNRAS, 484, 869
Vazdekis, A., Casuso, E., Peletier, R. F., & Beckman, J. E. 1996, ApJS, 106, 307
Vazdekis, A., Sánchez-Blázquez, P., Falcón-Barroso, J., et al. 2010, MNRAS, 404, 1639
Villeneuve, E., & Carfantan, H. 2014, ITIP, 23, 4322
Wake, D. A., Bundy, K., Diamond-Stanic, A. M., et al. 2017, AJ, 154, 86
Westfall, K. B., Cappellari, M., Bershady, M. A., et al. 2019, AJ, 158, 231
Yan, R., Bundy, K., Law, D. R., et al. 2016, AJ, 152, 197